STUDIA UNIVERSITATIS
BABEŞ-BOLYAI

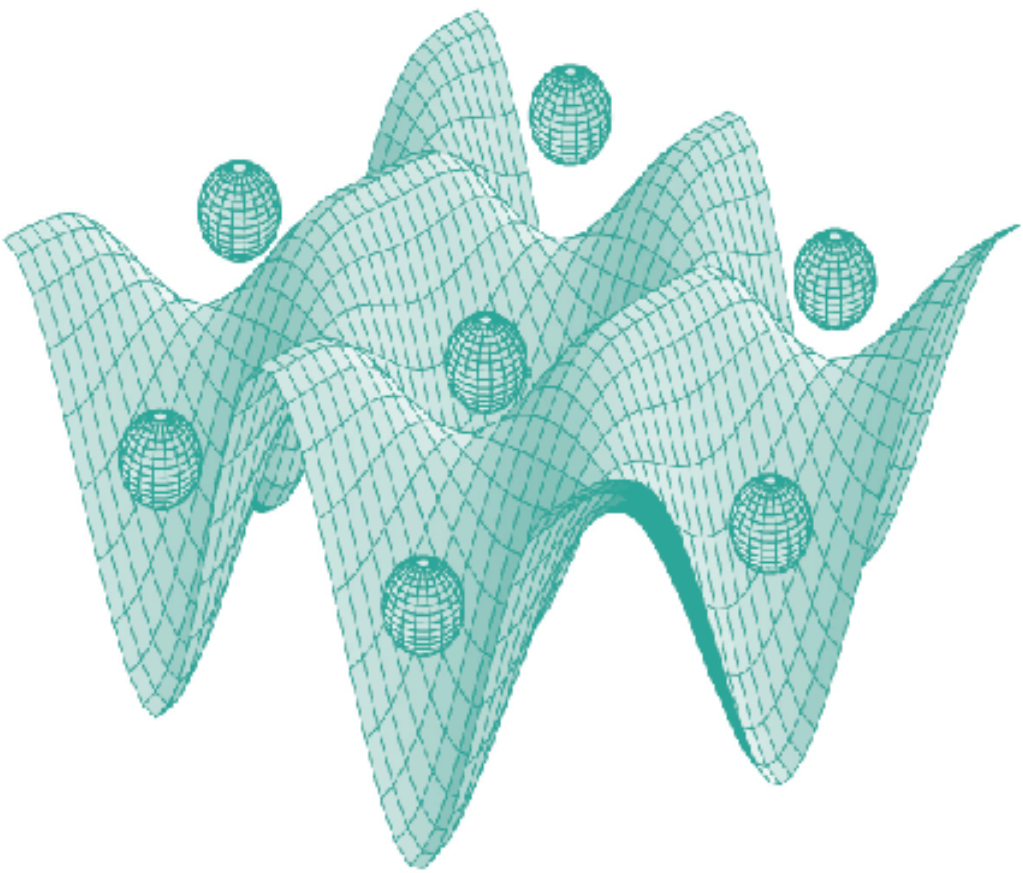

PHYSICA

1-2/2021

STUDIA
UNIVERSITATIS BABEŞ-BOLYAI
PHYSICA

1-2/2021
January-December

EDITORIAL OFFICE OF STUDIA UBB PYSICA:
1, M. Kogălniceanu St., Cluj-Napoca, ROMANIA, Phone: +40 264 405300
http://www.studia.ubbcluj.ro/serii/physica/index_en.html

YEAR **Volume 66 (LXVI) 2021**
MONTH **DECEMBER**
ISSUE **1-2**

PUBLISHED ONLINE: 2021-12-30
PUBLISHED PRINT: 2021-12-30
ISSUE DOI:10.24193/subbphys.2021

S T U D I A
UNIVERSITATIS BABEŞ–BOLYAI
PHYSICA

1-2

STUDIA UBB EDITORIAL OFFICE: B.P. Hasdeu no. 51, 400371 Cluj-Napoca, Romania, Phone + 40 264 405352

CUPRINS – CONTENT – SOMMAIRE – INHALT

STUDIA UBB PHYSICA, Vol. 66 (LXVI), 1-2, 2021, pp. 5-7
(RECOMMENDED CITATION)

Foreword:

Anniversary of Professor Viorel POP

It is a great pleasure to honor Viorel Pop with this dedicated issue on "*Studia Universitatis Babes-Bolyai Physica*". Viorel Pop has contributed to the synthesis and characterization of various materials, like intermetallic compounds, polycrystalline, nanocrystalline or nanocomposite magnetic materials and high T_c superconducting oxides. Viorel Pop research activity have covered a broad range of materials and methods and is well recognized in the worldwide scientific community.

Viorel Pop was born in Pintic/Dej, Cluj County, Romania, on March 25th, 1956 and graduated Faculty of Physics at the Babes-Bolyai University in 1981. In the period 1981-1982 he has followed Master studies in Solid State Physics at the same University. He performed his PhD studies between 1989 and 1993 at Babes-Bolyai University and Laboratoire de Magnétisme Louis Néel, Université Joseph Fourier under the supervision of prof. Emil Burzo and dr. Rafik Ballou. In this time his studies became more complex, and they covered a broader research field. His Ph.D. thesis was entitled "*Physical Properties of Rare Earth - 3d Transition Metals Compounds*".

He starts to work in 1982 as a researcher at Institute for Nuclear Power Reactors till 1983. During this period, his researches was focused on studies of nuclear fuel for the Cernavodă plant. From 1983 till 1990 he has occupied a research position Institute for Atomic Physics, Materials Physics and Technology Bucharest, Măgurele, Romania. In this period his activity was focused on preparation and characterization of rare earth-3d intermetallic compounds, different classes of hard magnetic materials and high T_c superconducting materials.

He has moved to Faculty of Physics, Babes-Bolyai University in 1990. He was researcher in physics (1990-1994) assistant professor (1994-1997), associate professor (1997-2002) and full professor starting with 2002. In this period, he was teaching different courses, seminars and laboratory classes, at bachelor level, like: - Magnetism, Magnetic Materials, Electricity and Magnetism, Materials Technology, master level courses as follows: "Physics of Metals and Alloys", "Magnetic and Superconducting Materials", "Magnetic Phenomena Physics", "Solid State Electronics" and Ph.D. level: "Advanced methods in the study of the condensed state". He was

focused on understanding the new directions in physics and applied physics, and to share this new information's, with him students, during the lectures. The teaching activities performed in all these years were very appreciated by him students.

Viorel Pop research interest was focused in the field the synthesis and study of the structural and magnetic properties of materials like rare earths-3d transition metals intermetallic compounds, superconducting oxides, spring magnets from both, basic and applied research. Recent research activity was focuses on two main areas:

- Synthesis and characterization of new hard magnetic phases without rare earths. Recently, the hard magnetic phases based on intermetallic compounds based on Fe and Mn have acquired a special interest in obtaining magnets without rare earths. His researches were focused in order to stabilize new magnetic phases with high anisotropy and a positive coupling of 3d magnetic moments.
- Preparation and characterization of hard/soft magnetic nanocomposites coupled by interphase exchange (spring magnets). It was shown that the interphase exchange coupling results from the intrinsic parameters of the hard and soft magnetic phases coupled by exchange interactions. The main objective in this direction was to influence the phases and their structure and microstructure on the interphase exchange torque.

The research results were expressed in more than 160 papers with 134 papers published in high impact ISI journals like journal of *Alloys and Compounds*, *Journal of Physics D: Applied Physics*, *Journal of Magnetism and Magnetic Materials*, *Journal of Materials Science, Solid State Communications, IEEE Transactions on Magnetics, Intermetallics, Journal of Applied Physics, Physica Status Solidi, Physical Review B* etc. He also has published 2 books. The high quality and impact on the scientific community of his publications is confirmed by the large number of citations (more than 1800). For his performance he was honoured with Romanian Academy award for the scientific activity, (1990) and Babes-Bolyai University award for excellence in didactic activity (2016).

Viorel Pop was invited in prestigious institutions for research stages at Laboratoire de magnétisme Louis Néel, CNRS, Grenoble, France (1991- 1992), ENEA, Dipartimento Energia, Frascati (Rome), Italy, (2002), Invited associate professor, Université Joseph Fourier, Laboratoire de Cristallographie, CNRS, Grenoble, France (2002), Invited researcher, Laboratoire de Cristallographie, CNRS, Grenoble, France (2004), (2008), Invited professor: Université Joseph Fourier, Laboratoire de magnétisme

Louis Néel, CNRS, Grenoble, France (2005), Université de Nantes, Institut de Matériaux Jean Rouxel (2012) and (2013), Chemnitz University of Technology, Germany (2012), (2013) and University of Augsburg, Institute of Physics, Germany (2014). In the same period Viorel was member in different committees for PdD defence at the doctoral schools from École Normale Supérieure Paris, Limoges University, Rhone-Alpes Univerity Grenoble, and Osnabrueck University.

Besides the rigorous scientific activity carried out at the Faculty of Physics of the Babes-Bolyai University, he was permanently involved in the academic development at local and national levels. In this respect, he served as Director at the College of Environmental Physics, Dej, extension of the Faculty of Physics of Babes-Bolyai University Cluj-Napoca (2001–2003), Director at Institute of Technology of Babes-Bolyai University (2008–2010) were he structured and organized the Institute of Technology of University Babes-Bolyai, as Secretary of the Cluj Branch of the Romanian Physics Society (2008–2016), as member of the National Council for Research in Romanian University (2000–present), as member of the National Council for the Recognition of University Degrees (2010–2020).

Having in view his research results Viorel won more than 8 research grants as project coordinator and more than 10 research grants as team leader.

Viorel Pop was serving as Secretary for: Magnetic Materials and Superconductors Conference, Cluj-Napoca, (1994) and (1996); 3rd General Conference of the Balkan Physical Union, Cluj-Napoca, Romania 2-5 September (1997) and Co-director of European School on Magnetism: ESM 2007, "*New Magnetic Materials and their Functions",* Cluj-Napoca, Romania and ESM 2015, "*From Basic Magnetic Concepts to Spin Currents*", Cluj-Napoca, Romania.

He is also a member of the following international scientific societies: European Physical Society, Romanian Physical Society, IEEE Magnetics Society, Balkan Physical Society, Romanian Magnetic Materials Society

Under his supervision, many students have obtained their B.Sc. or M.Sc. Diploma, 5 students obtained a PhD in physics, and some of him coworkers decided to follow an academic career. In the name of all those who have benefited from Professor Viorel Pop's scientific achievements, as well as from his being a knowledgeable advisor and colleague, we would like to express our deepest appreciation and best wishes for the future.

Dr. ROMULUS TETEAN

Professor at Babes-Bolyai University

STUDIA UBB PHYSICA, Vol. 66 (LXVI), 1-2, 2021, pp. 9-17
(RECOMMENDED CITATION)
doi:10.24193/subbphys.2021.01

MAGNETIC PROPERTIES OF $PrFe_{11}Ti$ ALLOYS BY Co AND Zr DOPING

D. BENEA[1]

ABSTRACT. Theoretical investigations on the electronic and magnetic properties (magnetic moments, magneto-crystalline anisotropy, exchange-coupling parameters) of the $PrFe_{11-x}Co_xTi$ (x = 0 – 3) and $Pr_{0.8}Zr_{0.2}Fe_{11}Ti$ alloys are presented. Our calculations show that Co for Fe doping in $PrFe_{11-x}Co_xTi$ maximize the calculated total magnetic moment and magnetocrystalline anisotropy energy (MAE) for x = 1. The calculated exchange-coupling parameters for the first neighbours of each Fe site (*8i*, *8j* and *8f*) show an increase by increasing the Co content suggesting higher Curie temperatures for Co doped $PrFe_{11}Ti$-based alloys. On the other hand, the Zr for Y substitution in $Pr_{1-y}Zr_yFe_{11}Ti$ (y = 0 - 0.2) decreases MAE without a noticeable decrease of the calculated total magnetic moment. Zr doping has opposite effects on the exchange coupling parameters J_{ij} for different spin pairs. As consequence, any significant changes of the Curie temperatures are predicted for Zr doped $PrFe_{11}Ti$ based alloys in the investigated doping range.

Keywords: *A. ab-initio calculations; B. magneto-crystalline anisotropy; C. magnetization; D. rare earth magnets.*

INTRODUCTION

Between the R-T (R- rare earth, T- 3d transition metals) intermetallic compounds, the 1:12 compounds with $ThMn_{12}$ structure type (space group I4/mmm) have been intensely studied due to their low ratio of rare earth and high content of low-cost iron. The partial substitution of Fe with M (Ti, V, Cr, Mo, W or Al) it is necessary to stabilize the phase, as binary R - Fe intermetallic phase is not formed for each rare earth element R. All the $RFe_{12-x}M_x$ compounds are characterized by high values of saturation magnetization and Curie temperatures, respectively. The relatively high values of magnetocrystalline anisotropy allow them to be considered as candidates for permanent magnets applications [1].

[1] *Faculty of Physics, Babeș-Bolyai University Cluj-Napoca, Kogălniceanu str. 1, 400084 Cluj-Napoca, Romania*

The recent research directions are oriented to reduction of critical rare earth content in order to obtain low-cost permanent magnets [2]. In this sense, several substitutions were employed to decrease the critical rare-earth content, either by non-critical rare earth elements (Ce) or by other elements (Y, Zr) with similar atomic radius with the rare earth elements [3]. Moreover, partial Co for Fe substitution increase the magnetization and the Curie temperature of the $RFe_{11-x}Co_xTi$ alloys [3-5]. Other method used to enhance coercivity and magnetization of the $R(Fe,M)_{12}$ compounds is the light elements (H, B, C) interstitial addition [4]. Some substitutions have adverse effects, as for $CeFe_9Co_2Ti$, where the low value of coercivity has been reported [6].

In the present paper we present our investigations on the magnetic properties of Co and Zr doped $PrFe_{11}Ti$-based alloys. The calculated total magnetic moments, MAE and the exchange coupling parameters are analysed and compared with the corresponding values obtained for Zr and Co doped $YFe_{11}Ti$ -alloys [4]. Our investigations results may give insight on the possible routes of enhancement for main magnetic properties (magnetization, MAE and Curie temperature) which are important for permanent magnet applications.

CALCULATIONS DETAILS

Electronic band structure calculations have been done using the SPRKKR band structure method. The method is based on the KKR-Green's function formalism that makes use of multiple scattering theory [7]. The fully relativistic approach has been employed, i.e., all relativistic effects have been taken into account, including the spin-orbit coupling, for ferromagnetic and antiferromagnetic spin configurations. The angular momentum expansion of the basis functions was taken up to *l* = 3 for rare earth elements and *l* = 2 for Fe, Co, Zr and Ti. The exchange and correlation effects have been accounted for by means of the generalized gradient approximation with the parametrization of Perdew et al. (GGA-PBE) [8]. The k-space integration was performed using the special points method [9]. The substitutional disorder in the system has been treated within the Coherent Potential Approximation (CPA) theory [10]. Full potential approach has been used for self-consistent band structure calculations.

Additionally, the study of the magnetic anisotropy has been performed by calculating the magnetic torque acting on the magnetic moment $\overrightarrow{m_i}$ of the atomic site *i,* oriented along the magnetization direction $\vec{M}$ [11,12]. As the component of the magnetic torque with respect to axis $\hat{u}$ is defined by $T_{\hat{u}}(\theta,\varphi) = -\partial E(\overrightarrow{M}(\theta,\varphi))/\partial\theta$, where θ and φ are the polar angles, a special geometry can be used to relate the

magnetic torque and the energy difference between the in-plane and out-of-plane magnetization directions. For a uniaxial anisotropy, by setting the angles to $\theta = \pi/4$ and $\varphi = 0$, the calculated magnetic torque is $T_{\hat{u}}(\pi/4,0) = E_{[100]} - E_{[001]}$ [12].

A complementary approach to investigate the magnetic behaviour of solids is to consider particular microscopic models making use of magnetic interaction. One of the approaches widely used is based on the classical Heisenberg Hamiltonian described by the expression:

$$H_{ex} = -\sum_{ij} J_{ij} \hat{e}_i \cdot \hat{e}_j ,$$

where the summation is performed on all lattice sites *i* and *j* and $\hat{e}_i$ / $\hat{e}_j$ are the unit vectors of magnetic moments on sites *i* and *j,* respectively. The J_{ij} exchange coupling parameters for the Fe and Co magnetic moments have been calculated as a function of distance using the expression derived by Liechtenstein [13] based on the magnetic force theorem.

RESULTS AND DISCUSSIONS

- ***Crystal structure***

The $R(Fe,M)_{12}$ compounds crystallize in the $ThMn_{12}$ structure (space group *I4/mmm*) having Fe atoms on 3 inequivalent crystal sites (*8i*, *8j* and *8f*) and the R atoms on *2a* sites (Figure 1). By Ti for Fe substitution, as determined by neutron diffraction experiments [6], the Ti atoms occupy preferentially the *8i* sites. On the other hand, by experimental investigations if was found that Co atoms occupy preferentially sites in the sequence *8j > 8f > 8i* in $PrFe_{11-x}Co_xTi$ alloys [4]. For interstitial dopants (H, C and B), the *2b* sites within the structure are occupied [4, 6].

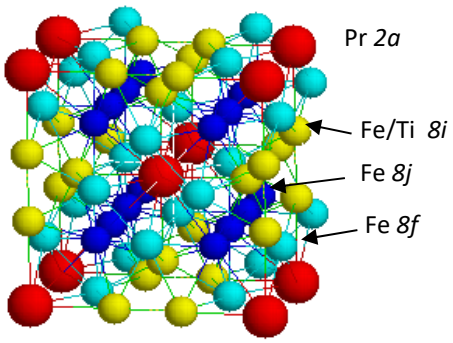

Figure 1. The $ThMn_{12}$ structure (space group *I4/mmm*) of $PrFe_{11}Ti$. The Pr atoms on *2a* sites are red spheres, whilst Fe atoms are represented as green (*8i)*, blue (*8j)* and grey (*8f*) spheres, respectively.

- ***Magnetic moments***

Band structure calculations have been performed using the SPR-KKR method for the $PrFe_{11-x}Co_xTi$ using the experimental lattice constants [14, 15]. Calculated magnetic moments (in Bohr magnetons μ_B) for the $PrFe_{11-x}Co_xTi$ and $Pr_{0.8}Zr_{0.2}Fe_{11}Ti$ are shown in Table 1. Our theoretical calculations show monotonic increase of Fe magnetic moment on each crystal site by increasing Co content. The Fe spin magnetic moments are in following the sequence m_S^{Fe}(*8j*) > m_S^{Fe} (*8i*) > m_S^{Fe} (*8f*), which is consistent with the sequence determined experimentally for other 1:12 phases [16].

Table 1. Calculated magnetic moments (in Bohr magnetons μ_B) for the $PrFe_{11-x}Co_xTi$ and $Pr_{0.8}Zr_{0.2}Fe_{11}Ti$. Preferential occupation of Co for *8j* and *8f* sites has been considered. Lattice constants for $PrFe_{11-x}Co_xTi$ from [15] are considered.

	$PrFe_{11}Ti$		**$PrFe_{10}CoTi$**		**$PrFe_9Co_2Ti$**		**$PrFe_8Co_3Ti$**		**$Pr_{0.8}Zr_{0.2}Fe_{11}Ti$**	
	$m_s(\mu_B)$	$m_l(\mu_B)$	$m_s(\mu_B)$	$m_l(\mu_B)$	$m_s(\mu_B)$	$m_l(\mu_B)$	$m_s(\mu_B)$	$m_l(\mu_B)$	$m_s(\mu_B)$	$m_l(\mu_B)$
Pr	1.04	-0.01	0.97	-0.01	0.90	-0.01	0.86	-0.01	1.05	-0.02
Zr									1.05	-0.02
Fe *8i*	2.34	0.06	2.37	0.07	2.41	0.08	2.42	0.08	2.35	0.06
Ti *8i*	-0.93	0.01	-0.91	0.02	-0.88	0.02	-0.86	0.02	-0.95	0.01
Fe *8j*	2.40	0.06	2.45	0.07	2.49	0.07	2.50	0.08	2.40	0.06
Co *8j*			1.60	0.11	1.60	0.12	1.60	0.12		
Fe *8f*	2.06	0.05	2.17	0.06	2.24	0.06	2.27	0.06	2.07	0.05
Co *8f*			1.56	0.09	1.56	0.10	1.56	0.10		
Total	24.97	0.64	24.96	0.75	24.60	0.86	23.90	0.93	25.03	0.62

The calculated spin magnetic moments of Fe for undoped $PrFe_{11}Ti$ alloy values range between 2.06 μ_B for Fe *8f* and 2.40 μ_B for Fe *8j*. The lowest value of the m_S^{Fe} (*8f*) could be related with the interatomic Fe-Fe distances, as those of *8f* site are the smallest and those of *8i* sites are the longest.

By Co doping, each Fe spin moment is increased, the highest rate of increase (10%) being obtained for Fe *8f* atoms (from 2.06 to 2.27 μ_B). The orbital moments (m_l) of Fe atoms on *8i* and *8j* sites are also showing small increase (from 0.06 to 0.08 μ_B) whilst the m_l values for Fe *8f* sites do not change by changing the Fe/Co ratio in the alloys. The spin magnetic moment of substitutional Co is 1.60 μ_B on *8j* sites and 1.56 on *8f* sites, independent on Co content within the considered doping range. In the same time, Co substituting atoms have increased orbital moments, which contribute also at the total orbital magnetic moment enhancement, which is increasing from

0.64 μ_B/f.u. (x = 0) to 0.93 μ_B/f.u. (x = 3). The calculated maximum value of the total magnetic moment is obtained for x = 1, with values of m_s = 24.96 μ_B and m_l = 0.75 μ_B for $PrFe_{10}CoTi$. The total magnetic moment is in agreement with other reported experimental and theoretical investigations (22.72 μ_B and 23.02 μ_B, respectively) [14]. We note that Co distribution on crystallographic sites has important influence on calculated magnetic moments. Also, as the electronic correlations are not accounted in the present study, the Pr magnetic moment is expected to be underestimated. However, Pr calculated moment shows agreement with the corresponding calculated value for $PrFe_{11}Ti$ (1.31 μ_B) of Bouhbou et al. [14].

- ***Magnetocrystalline anisotropy***

The magnetocrystalline anisotropy for Co doped alloys is shown in Figure 2, together with similar calculations for $YFe_{11-x}Co_xTi$ alloys [17]. As can be seen in Figure 2, MAE reaches a maximum value for x = 1. The site-dependence of the MAE shown in Figure 2 reveals the origin of this change. As can be seen, the transition metals on *8j* sites, followed by those from *8i* sites have the largest main MAE contributions. A small MAE contribution comes from *8f* site, which is negative for undoped $PrFe_{11}Ti$, changing to positive sign for x = 1, 2 and again negative for x = 3. The *2a* site contribution, occupied by Pr is underestimated, as the electronic correlations are not accounted. Pr is expected to add a negative contribution at MAE [18, 19], higher in modulus than current calculated values (~ -0.07 meV for x = 1). Due to this known deficiency, only the MAE behavior in Fe sublattices is discussed. The overall MAE contribution of transition metal atoms increases with Co content, reaching the maximum value for x = 1. This dependence is explained also by the interplay between the Fe axial local anisotropy and that of Co which is planar [16]. The evolution of transition metals MAE with Co content x is very similar with the experimental determined anisotropy constant K_1 for by Tereshina et al. [16] for $YFe_{12-x}Co_xTi$ alloys where a maximum at x = 1 is also reached, with a K_1 value of 0.98 MJ/m^3 deduced from measurements at 300 K. Our calculations show a value for magnetic anisotropy energy of $YFe_{10}CoTi$ alloy of 1.57 MJ/m^3 [17], whilst for $PrFe_{10}CoTi$ alloy a higher value is obtained (2.24 MJ/m^3). The calculated value is in the relative agreement with other calculations for $PrFe_{11}Ti$ [14].

By Zr for Y substitution in $Pr_{0.8}Zr_{0.2}Fe_{11}Ti$, the main MAE contribution of transition metals comes from *8j* site (0.35 meV), the *8i* site contribution being reduced compared with undoped alloy (0.06 meV), whilst 8f site has negative contribution (-0.11 meV). As consequence, total MAE is reduced by Zr doping compared to $PrFe_{11}Ti$ alloy.

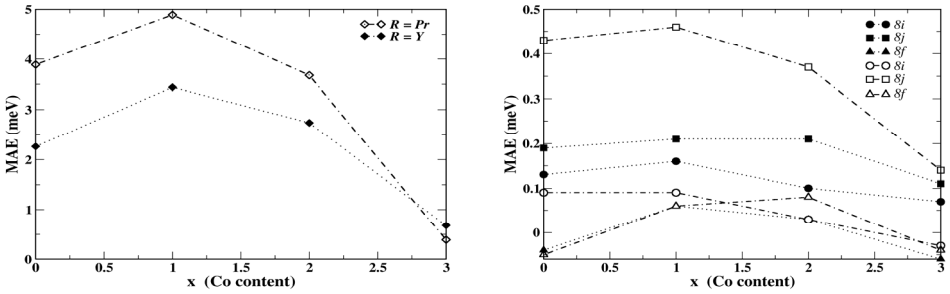

Figure 2. Site-dependent average magnetocrystalline anisotropy (in meV) calculated using the torque method [8] for $RFe_{11-x}Co_xTi$ (R = Y, Pr). Filled symbols (● – *8i*; ■ - *8j* and ▲ - *8f*) have been used for R = Y and open symbols (○ - *8i*, □ - *8j* and Δ - *8f*) for R = Pr.

- ***Exchange-coupling parameters***

The exchange coupling parameters J_{ij} between Fe spins from *8i*, *8j* and *8f* sites calculated using the magnetic force theorem [13] for the $PrFe_{11-x}Co_xTi$ alloy and $Pr_{0.8}Zr_{0.2}Fe_{11}Ti$ alloys are shown on Figure 3. The highest strength of the exchange interaction is obtained between Fe *8i* spins, followed by Fe *8f* – Fe *8f* exchange interaction; other exchange interactions between pair of Fe spins are lower than half in magnitude compared with Fe *8i* - Fe *8i* exchange interaction. The highest J_{ij} values obtained for nearest neighbours are increasing by Co substitution for almost all pairs of spins.

The exchange coupling parameters J_{ij} between Co spins from *8i* sites and the spins of Fe and Co neighbours have been also checked. Analysing their behaviour with Co content x we concluded that that these exchange interactions are almost independent on the Co content and for simplicity are not shown here. We note that the highest values of J_{ij} appear for Co – Fe *8f* next neighbour interaction. Based on discussed dependencies of the exchange coupling parameters of Co and Fe spins by Co doping, it is expected that the Curie temperatures for $PrFe_{11-x}Co_xTi$ alloys to increase by increasing the Co content x, in agreement with experimental measurements [15].

By Zr for Pr doping, the calculated exchange-coupling parameters between pairs of Fe spins, considering by turn Fe *8i, 8j* and *8f* spins at the origin, are also shown in Fig. 1. For the Fe 8*i* -Fe *8i,* the Fe 8*i* -Fe *8i* and Fe *8j* -Fe *8f* pairs, the exchange coupling parameters J_{ij} with first neighbours decrease by Zr doping, in contrast to J_{ij}*s* of the other Fe spin pairs which show opposite trend. Accounting the number of such pairs showing enhancement/decrease of next neighbours J_{ij}, the Curie temperature of $Pr_{0.8}Zr_{0.2}Fe_{11}Ti$ is not expected to be strongly influenced by Zr substitution.

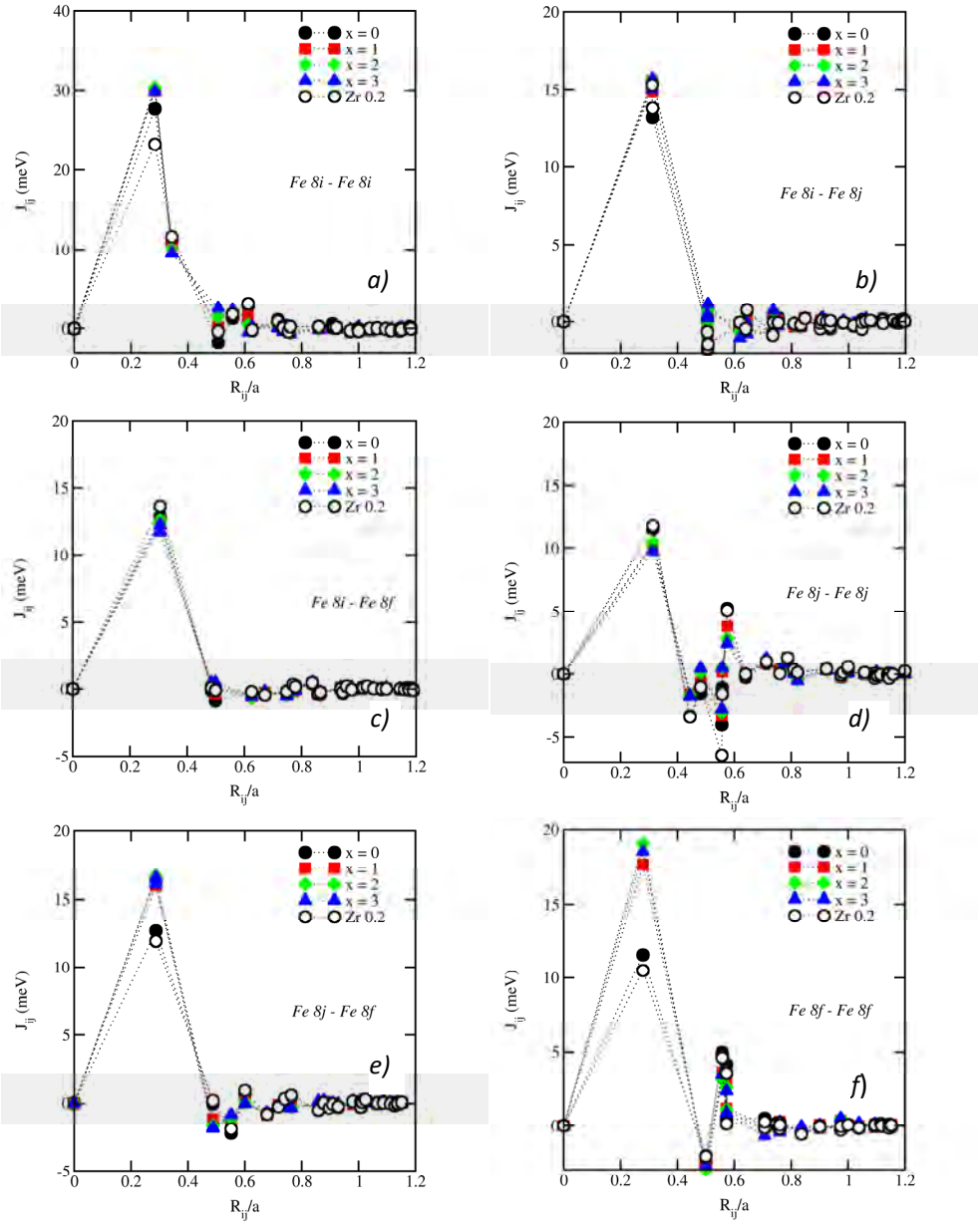

Figure 3. The exchange coupling parameters J_{ij} between Fe spins from *8i*, *8j* and *8f* sites for $PrFe_{11-x}Co_xTi$ and $Pr_{0.8}Zr_{0.2}Fe_{11}Ti$ (y = 0.2) alloys, with Fe *8i* (*a, b* and *c*), Fe *8j* (*d* and *e*) and Fe *8f* (*f*) at the origin.

CONCLUSIONS

Theoretical studies presented here show that Co for Fe substitutions in $PrFe_{11}Ti$ alloys increase Fe magnetic moments, transition metals contribution at MAE for $x \leq 1$ and the exchange-coupling parameters (J_{ij}) between nearest neighbours. Also, Zr for Pr substitution preserve the magnetic moments magnitude, but reduces slightly the transition metals contribution at MAE. In addition, Zr doping in $PrFe_{11}Ti$ alloys do not cause overall diminishment of the exchange coupling between Fe pairs from different crystal sites. As consequence, Zr doping could be used in $PrFe_{11}Ti$- alloys in order to stabilize the phase and to reduce the Pr content, without significant weakening of the magnetic properties important for applications as permanent magnets.

ACKNOWLEDGEMENTS

The author acknowledges the long and fruitful collaboration with Prof. Dr. Viorel Pop, counting over 20 common ISI papers, other 3 BDI indexed papers and the partnership in 12 scientific projects. Also, Diana Benea thanks for all encouragement, guidance and support during over 15 years of scientific collaboration.

The financial support from the Romanian Ministry of Education and Romanian Ministry of Research and Innovation, CCCDI-UEFISCDI grant PN-III-P2-2.1-PED-2019-3484 is acknowledged.

References

[1] K. H. J. Buschow, *J. Magn. Magn. Mater.,* 100 79 (1991).
[2] A.M. Gabay and C. C. Hadjipanayis, *Scripta Materialia,* 154 284 (2018).
[3] P. Tozman, H. Sepehri-Amin, Y. K. Takahashi, S. Hirosawa and K. Hono, *Acta Materialia,* 153 354 (2018).
[4] L. Ke and D. D. Johnson, *Phys. Rev. B,* 94 024423 (2016).
[5] A. M. Gabay, A. Martin-Cid, J. M. Barandiaran, D. Salazar and G. C. Hadjipanayis, *AIP Advances,* 6, 056015 (2016).
[6] J. M. D. Coey, *Engineering,* 6 119 (2020).
[6] Von Barth U. and Hedin L., *J. Phys*., C5 1629 (1972).
[7] Ebert H., Ködderitzsch D. and Minar J., *Rep. Prog. Phys.,* 74 096501 (2011).
[8] J. P. Perdew, K. Burke, M. Ernzerhof, *Phys. Rev. Lett.,* 77 3865 (1996).
[9] Monkhorst H. and Pack J., *Phys. Rev. B*, 13, 5188 (1976).
[10] Faulkner J.S., *Prog*. *Mater. Sci.,* 27 1 (1982); Faulkner J. S. and Stocks G.M., *Phys. Rev. B*, 21 3222 (1980).

[11] J.B. Staunton, L. Szunyogh, A. Buruzs, B.L. Gyorffy, S. Ostanin, and L. Udvardi, *Phys. Rev. B,* 74 144411 (2006).
[12] S. Mankovsky, S. Polesya, J. Minar, F. Hoffmann, D.H. Back and H. Ebert, *Phys. Rev. B,* 84 201201 (2011).
[13] Liechtenstein A.I., Katsnelson M.I., Antropov V.P. and Gubanov V.A., *J. Magn. Magn. Mater.,* 67 65 (1987).
[14] M. Bouhbou, R. Moubah, E.K. Hlil, H. Lassri and L. Bessais, *J. Magn. Magn. Mater.,* 518 167362 (2021).
[15] L. Bessais, S. Sab and C. Djega-Mariadassou, *Phys. Rev. B*, 66 054430 (2002).
[16] I.S. Tereshina, P. Gaczynski, V.S. Rusakov, H. Drulis, S.A. Nikitin, W. Suski, N.V. Tristan and T. Palewski, *Phys. Condens. Matter.,* 13 8161 (2001); I.S. Tereshina, S.A. Nikitin, T.I. Ivanova, K.P. Skokov, *J. Alloys Compd.*, 275-277 625 (1990).
[17] D. Benea et al., Co, Zr and C doping on $RFe_{11}Ti$-based alloys (R = Y, Gd), in press (2022).
[18]. R. Skomski and D.J. Sellmyer, *J. of Rare Earth*, 27 675 (2009).
[19] X. C. Kou, T.S. Zhao, R. Grossinger, H.R. Kirchmayr, X. Li and F.R. de Boer, *Phys. Rev. B,* 47 3231 (1993).

STUDIA UBB PHYSICA, Vol. 66 (LXVI), 1-2, 2021, pp. 19-30
(RECOMMENDED CITATION)
doi:10.24193/subbphys.2021.02

SOFT MAGNETIC NANOCRYSTALLINE Ni-Fe-X-Y AND $MeFe_2O_4$ POWDERS OBTAINED BY MECHANOSYNTHESIS

I. CHICINAȘ[1*], F. POPA[1], B.V. NEAMȚU[1], T.F. MARINCA[1], O. ISNARD[2], V. POP[3]

ABSTRACT. The soft magnetic nanocrystalline powders, alloys (Ni_3Fe, 79Ni16Fe5Mo, 77Ni14Fe5Cu4Mo, wt. %) and zinc ferrite, were obtained by dry and wet mechanical alloying and reactive milling, followed by different heat treatments. The powders were characterised by X-ray diffraction, scanning electron microscopy, X-ray microanalysis, differential scanning calorimetry, thermomagnetic and magnetic measurements. The X-ray diffraction shown the progressive new phases formation. The crystallite size is between 18-7 nm depending on materials and milling conditions. The particle size is smaller for wet-mechanical alloying comparing with dry-milling. The thermomagnetic measurement shown the Curie temperature of the alloys. The spontaneous magnetisation of the wet-milled and annealed samples is higher than of the molten alloys.

Keywords*: mechanical alloying; Ni-Fe-X-Y alloys; soft ferrite; magnetisation; XRD; DSC.*

INTRODUCTION

Materials having crystallite/particle size smaller than 100 nm are known as nanocrystalline/nanostructured/nanosized materials. Nanocrystalline materials have unique properties if their crystallites are smaller than the characteristic length of the physical phenomena occurring in bulk materials. These different properties derive from the large number of atoms placed at the grain boundaries, interfaces/

[1] *Materials Science and Engineering Department, Technical University of Cluj-Napoca, 103-105 Muncii Ave., 400641 Cluj-Napoca, Romania*
[2] *Institut Néel, CNRS / Université Grenoble Alpes, 25 rue des Martyrs, BP166, 38042 Grenoble, Cédex 9, France*
[3] *Babeş-Bolyai University, Faculty of Physics, 1 Kogălniceanu Str., 400084 Cluj-Napoca, Romania*
* *Corresponding author: ionel.chicinas@stm.utcluj.ro*

interphases as compared to the same materials in the polycrystalline state [1-3]. Thus, the atoms located at interfaces determine decisively the physical/mechanical properties of the nanocrystalline materials. The benefits of the nanocrystalline state are due to chemical and structural variations on a nanoscale, very important to having optimal magnetic properties [1,2,4]. The very low coercivity in the nanocrystalline materials is different from superparamagnetic behaviour, where low coercivity come together with a low permeability. Due to the coupling of small ferromagnetic crystallites by exchange interactions, the nanocrystalline materials have simultaneously low coercivity and high permeability [5]. Such behaviour was explained by the random anisotropy model [6].

Fe–Ni alloys around the Ni_3Fe (Permalloy) composition and Fe–Ni–(X–Y) alloys, known as Supermalloy, are widely used for their high properties as soft magnetic materials. The production of these materials as nanocrystalline powders can add interesting properties. The interesting properties (superparamagnetic state, spin canting effect, partial redistribution of the cations) can be obtained in the nanocrystalline/ nanosized ferrites prepared by mechanical activation and mechanosynthesis, which were reviewed in Ref. [7].

In last decades, the different mechanosynthesis routes used in developing soft magnetic nanocrystalline powders (ferrites and alloys) or nanocomposite powders were reported. Here we summarize our contributions on obtaining new materials by mechanosynthesis with an emphasis on the Ni-Fe-(X-Y) and ferrites soft magnetic nanocrystalline powders obtained by mechanical alloying and reactive milling. Some results have been previously reported [8-25].

MATERIALS AND METHODS

For Ni-Fe and Ni-Fe-X-Y alloys producing the following elemental powders were used as starting materials: 123-carbonyl nickel, NC 100.24 (Höganäs) iron, Mo powder produced by chemical reduction and copper powder. The powder mixtures with the following composition were used: Ni_3Fe, 79Ni16Fe5Mo (wt. %) and 77Ni14Fe5Cu4Mo (wt. %). The soft magnetic ferrites were obtained from equimolar mixture of high purity commercial oxide powders (Alpha Aesar), MeO (Me = Ni, Cu, Zn) and iron oxide (α-Fe_2O_3—haematite).

All the mixtures of elemental powders or oxides, before milling, were homogenised for 15 minutes using a Turbula type apparatus. For mechanical alloying the starting mixtures (“ss” sample) were dry or wet milled in argon atmosphere using a planetary ball mill (Fritsch, Pulverisette 4 and Pulverisette 6). For wet milling

2 ml of benzene was added after each vial opening (for sampling) in order to avoid powders agglomeration via cold welding. The milling process were caried out in stainless steel vials (with 500 cm^3 volume), using stainless steel balls with 15 mm diameter. The ball to powder mass ratio (BPR) was between 8:1 and 10:1. Several milling times were used ranging from 1 to 12-28 hours, depending on mill and alloy. The milled powders were annealed in vacuum at 350 °C and 400 °C during 0.5 to 4 h to remove the internal stresses and also to finish the solid-state reaction leading to synthesis of a new phase. The nanocrystalline soft ferrites were obtained by reactive milling in air, using the same mill equipment. The ball to powder mass ratio (BPR) was 15:1.

The evolution of formation of new phases (alloy or ferrite) by milling was investigated by X-ray diffraction (XRD) in the angular range 2θ = 25–100° using a Siemens D5000 diffractometer, operating with CoKα radiation (λ = 1.7903 A) and Bruker D8 diffractometer operating with CuKα radiation (λ = 1.5418 Å). The mean crystallite size was determined on the milled and annealed samples from full-width-at-half maximum (FWHM) of the diffraction peaks using Scherrer's formula [26] and by Williamson-Hall method, on the as-milled samples [27].

Thermal stability of the samples was studied by a Setaram Labsys differential scanning calorimetry (DSC) apparatus, using high purity alumina as reference in the 25 – 800 °C temperature range using argon atmosphere. The heating/cooling rate was 10 °C/min.

The powders morphology and the local chemical homogeneity of the particles were investigated by scanning electron microscope (SEM, Jeol-JSM 5600 LV) equipped with an energy dispersive X-ray spectrometer (EDX, Oxford Instruments, Inca 200 soft).

The magnetisation measurements (M(H)) were made by the extraction sample method at 300 K and a maximum magnetic field of 8 T. The Curie temperatures of different phases were determined by thermomagnetic measurements.

RESULTS AND DISCUSSIONS

The XRD patterns for the powders obtained by mechanical alloying (MA) for times ranging from 2 to 28 h show a progressive formation of Ni_3Fe intermetallic compound by MA (Fig. 1). The iron Bragg peaks are vanished and after 6 hours of milling, they are indistinguishable from the background noise. This fact suggests the idea that iron atoms either formed a compound with nickel (Ni_3Fe), or formed a Ni-Fe solid solution. At the same time, a shift of the peaks towards the small angles is

observed. The shift to small angles is due (i) to the formation of the Ni_3Fe intermetallic compound and (ii) to the first order stresses induced by milling. The news peak positions after 10 hours of milling are at smaller angles than the Ni_3Fe positions, as a consequence of the first order internal stresses.

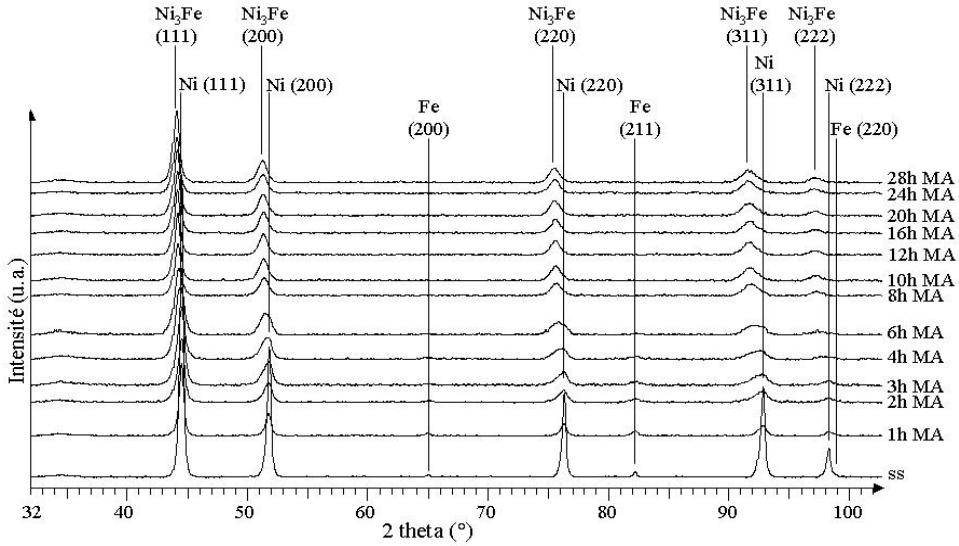

Fig. 1. X-ray diffraction patterns (Cu Kα1, λ = 1.5406 Å) for samples milled up to 28 hours. ss refers to the starting sample. For clarity, the spectra have been shifted vertically. There are indicated the positions of the Bragg peaks of nickel, iron and Ni_3Fe.

The influence of the annealing conditions (temperature and time) on the Ni_3Fe formation is shown for 8 h milled sample, figure 2. For 8 h as-milled sample a broad diffraction peak is observed at the Ni_3Fe position, accompanied by another peak of lower intensity which corresponds to the unreacted nickel during milling. After only 30 minutes of annealing at 400 °C, the intensity of the Ni_3Fe maxima increases and the Ni maxima has disappeared. By increasing the annealing time, the intensity of the Ni_3Fe maximum increases and also the maximum shifts towards large angles as a consequence of the internal stresses' removal. After 4 hours of annealing the peak position is at the same position as for Ni_3Fe obtained by fusion, as an effect of the stresses removal and finishing the solid-state reaction [28].

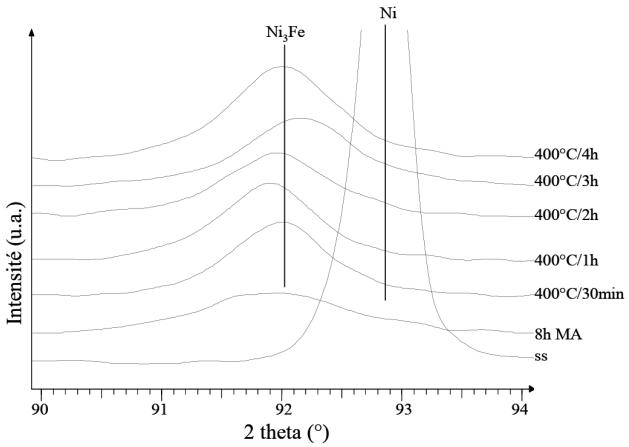

Fig. 2. The influence of annealing conditions on the (311) Ni_3Fe maxima of the samples milled 8 hours. ss denote the starting mixture.

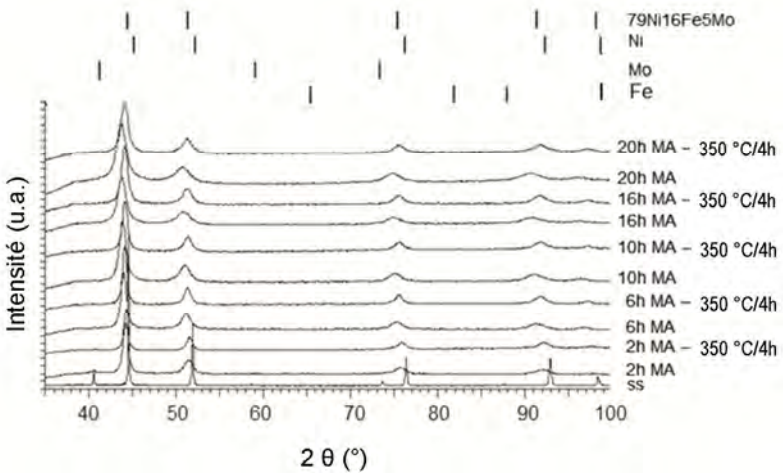

Fig. 3. X-ray diffraction patterns of 79Ni16Fe5Mo (wt %) mechanically wet-milled powders up to 20 hours and mechanically wet-milled and followed by annealing at 350°C for 4 hours (λ1 = 1.5406 Å). To clarity the diffractograms were vertically shifted. The starting mixture was indicated by the acronym ss. [29].

The evolution of the Supermalloy 79Ni16Fe5Mo (wt. %) formation by wet-milling up to 20 hours and annealing (350 °C for 4 h) is shown in figure 3. It can be shown a movement towards smaller angles and a broadening of the Bragg peaks by increasing the milling time. This displacement of the Bragg peaks is caused, similar

to Ni_3Fe alloy, by the formation of the alloy and by the first-order internal stresses that are induced by milling. X-ray patterns of the annealed samples show a better definition of diffraction peaks. The X-ray diffraction patterns of 79Ni16Fe5Mo powder after 6 hours of wet-milling followed by annealing shows that Bragg maxima correspond those of the alloy of the same composition obtained by fusion [29].

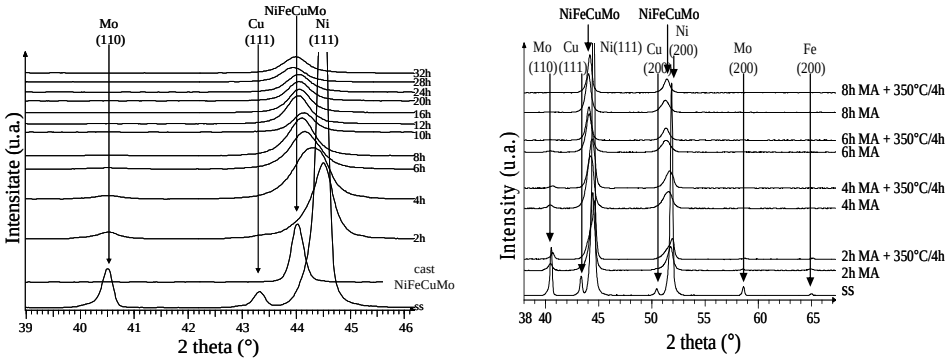

Fig. 4. X-ray diffraction patterns of 77Ni14Fe5Cu4Mo (wt. %). a - mechanically dry-milled powders up to 32 hours; b - mechanically dry-milled and followed by annealing at 350°C for 4 hours (λ1 = 1.5406 Å). To clarity the diffractograms were vertically shifted. The starting mixture was indicated by the acronym ss.

The evolution of the Mümetal (77Ni14Fe5Cu4Mo, wt. %) formation by milling up to 32 hours and annealing (350°C/4 h) is shown in figure 4 a, b. A displacement towards smaller angles and a broadening of the Bragg peaks by increasing the milling time was observed. In figure 4a, in the case of as-milled powders, the Cu, Fe and Mo Bragg peaks disappear after 4, 6 and 10 hours of milling respectively. By annealing the Mümetal alloy is formed after 8 hours of milling followed by an annealing at 350 °C/4 hours, figure 4b [28].

The evolution of Zn ferrite obtaining by reactive milling (RM) is shown in figure 5. After 4 hours of milling, they are noticed new, intense maxima, that correspond to the newly formed phase, zinc ferrite. Simultaneously with the appearance of these maxima also shows the disappearance of the maxima characteristic of zinc oxide, which indicates a rapid and complete amorphization of it or a diffusion of Zn and O atoms in the structure of iron oxide [30, 31]. Iron oxide maxima are much flattened (those that are visible in the diffractogram), but most can no longer be identified in diffractogram. The corresponding maxima of $ZnFe_2O_4$ are much more intense compared to the maximum of the unreacted iron oxide, which suggests that at this time of milling (4 hours) the major phase is Zn ferrite. The presence of elemental iron in the sample is

due to contamination of the powder on during milling. [31, 32]. Prolonged milling time (20-30 h) lead to a reaction between zinc ferrite and iron provided by contamination resulting in a wüstite type phase. The as-milled samples were subjected to a heat treatment in vacuum and in air at temperatures of 400, 500, 600, 700 and 800 °C for 4 hours. At temperatures higher than 500 °C a decomposition of the Zn ferrite with the presence of Fe_2O_3 was evidenced. The heat treatment at 500 ºC for 4 hours in the air is the only one we have a complete ferrite formation for all milling times. More information of $ZnFe_2O_4$, $NiFe_2O_4$, $CuFe_2O_4$ can be found in Ref [30]. All milled samples (alloys and ferrites) obtained by MA and RM are in the nanocrystalline state. The crystallite size of the Ni-Fe alloys decreases by increasing milling time, up to 18 – 7 nm, depending on alloys, milling equipment or type o milling (wet or dry) [28, 29]. The crystallite size of $ZnFe_2O_4$ powders obtained by RM is of 8 ± 2 nm after 30 hours of milling [30].

In Figure 6 are presented the SEM images of 77Ni14Fe5Cu4Mo powders

Wet milled for 4, 8 and 20 hours. The decrease of particle size with increasing milling time can be observed. In addition, for longer milling times (8 hours), particles with rounded corners can be observed. The two causes that lead to the decrease the size of the particles are, on the one hand, the stresses induced in the material by the milling, which reduce the plasticity of the material and, on the other hand, the presence of benzene on the surface particles that prevents cold welding processes. The same powders morphology evolution can be found for all samples obtained by MA.

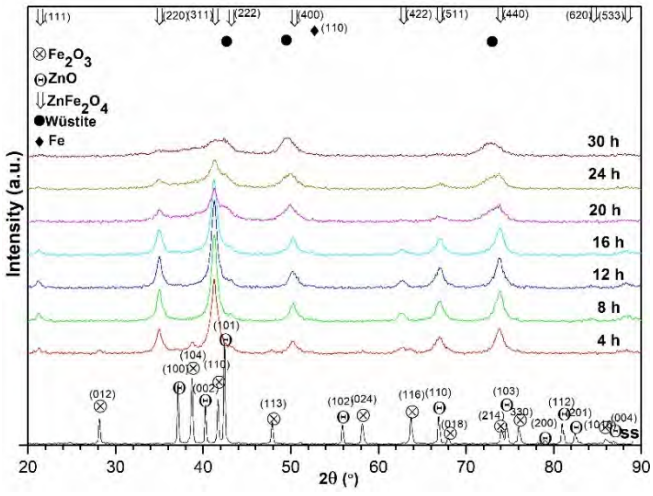

Fig. 5. XRD patterns of the as-milled samples (4, 8, 12,16, 20, 24 and 30 h). The starting sample is noted by ss. For clarity, the spectra have been shifted vertically. The XRD maxima for different phases are marked.

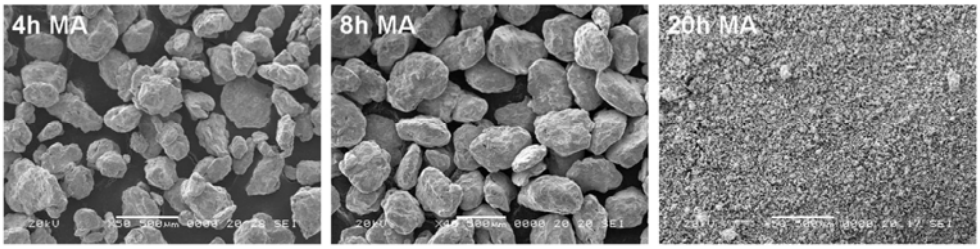

Fig. 6. SEM images of 77Ni14Fe5Cu4Mo powder milled for 4, 8 and 20 hours at magnification of 50x.

The DSC curves of the milled samples were evidenced the phase transformations in the powders during heating and cooling, such as: internal stresses removal, recrystallisation, Curie temperature and their changes with milling conditions. An interesting behaviour was observed on the DSC curves of the wet-milled samples, where the presence of an exothermic peak for all wet-milled samples can be observed, figure 7. This peak was attributed to the elimination of benzene adsorbed on the surface of powders. The elimination of benzene results from the thermal activation and the catalytic behaviour of Ni, Fe and Mo on the decomposition of benzene [33, 34]. concerning the exothermic peaks presented in figure 6 one can observe that (i) their surface increases (by a factor of 4), and (ii) a shift towards lower temperatures when the milling time increases (from 495 °C to 431 °C for a milling time of 4 and 20 hours respectively). The increase in the surface of the DSC peaks is related to the increase of the amount of benzene adsorbed on the surface and inside particles. A complete analysis of the presence of this exothermic peak in Ni_3Fe powders wet-milled was presented in Ref. [35].

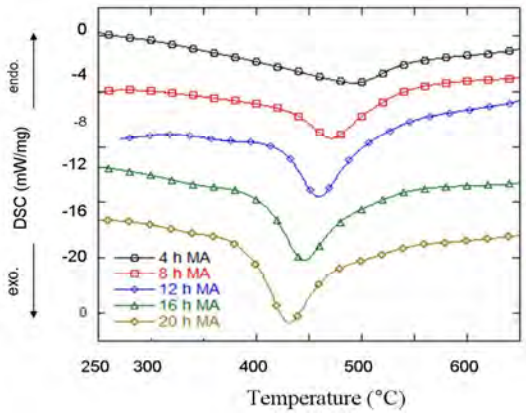

Fig. 7. DSC heating curves for 77Ni14Fe5Cu4Mo samples, wet-milled in benzene for 4, 8, 12, 16 and 20 hours. For more than clarity, the DSC curves have been shifted vertically. The atmosphere used in DSC was Ar + 5% H2

Thermomagnetic analysis offers the advantage of in-situ alloying study during heat treatment. Thermomagnetic measurements in a low field (less than 0.1 T) are shown in figure 8. These measures show the progressive formation of the alloy by MA, and by milling followed by annealing. For the starting sample (ss), the M^2 curve versus temperature shows two transitions on heating: one at the Curie temperature of nickel (T_C = 631 K) and the other at the Curie temperature of iron (T_C = 1043 K). On cooling, the $M^2(T)$ curve shows a mixture of ferromagnetic phases with the Curie temperatures over a wide range. These phases were formed at high temperature by the local diffusion of nickel, molybdenum and copper small particles in the larger iron particles. This can be explained by the fact that in the starting mixture there are large iron particles (average particle size is < 40 μm), surrounded by much smaller particles of nickel and molybdenum (about 5 – 7 μm). For the sample milled 4 h, on the heating curve is observed the Curie temperature of unreacted Ni and also the Curie temperature of the NiFeCuMo alloy formed by MA (a small change in the slope curve). Also, a progressive alloying process by heating with formation of a mixture of phases can be observed. No transition at the Curie temperature of iron is detected, because iron reacted with the other elements under the influence of temperature before 1043 K. By heating up to 1100 K, the 77Ni14Fe5Cu4Mo alloy is formed in the whole sample volume and, consequently, on the cooling curve only one Curie temperature is observed. The process is the same for the 10 h milled sample, but the amount of the unreacted elements during milling is very little. For 16 h milled sample, on the heating curve a single transition is visible at a temperature of 630 K (the Curie temperature of the alloy), but at cooling the transition is shifted towards higher temperatures. The difference between the Curie temperatures at heating and at cooling could be due to the appearance of an iron-rich phase. This can be due to the powder contamination with iron during milling at high milling time and under the influence of very high temperature iron-rich phases can form (the Ni_3Fe maybe). A complete analysis of the thermomagnetic measurements on the synthesis of nanocrystalline Supermalloy powders by mechanical alloying is presented in Ref. [17].

The spontaneous magnetization of the samples milled for 8 and 12 hours before and after annealing at 350 °C/4 hours is shown in figure 9. It is notable that the annealing leads to an increase of the value of the powder's spontaneous magnetization. This fact can be explained by the elimination of internal stresses and the decrease in the density of crystalline defects induced during milling. By comparing the value of the spontaneous magnetization of the annealed samples with the spontaneous magnetization of the molten alloy, also shown in the figure 9, it is obvious that the magnetizations for samples obtained by wet-milling are slightly higher. This

can be due to the contamination with iron from the balls and vials used, contamination that was observed during EDX analyses. It is well known that in the dry milling a protective layer from the materials milled is formed on the surface of the balls and vials which prevents or decreases the powder contamination. In the case of wet-milling, this protection layer is absent or too thin and its thickness may not be sufficient to prevent powder contamination.

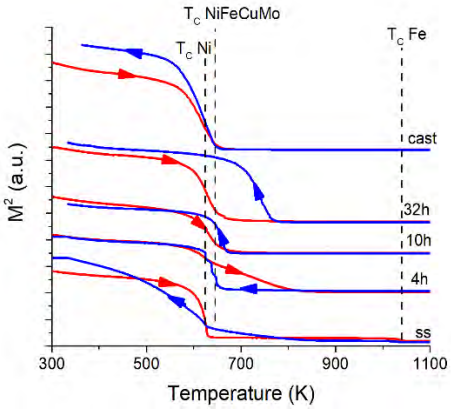

Fig. 8. The magnetization versus temperature for 77Ni14Fe5Cu4Mo powders milled 4, 10 and 32 hours. The starting sample (ss) and the cast sample are also presented.

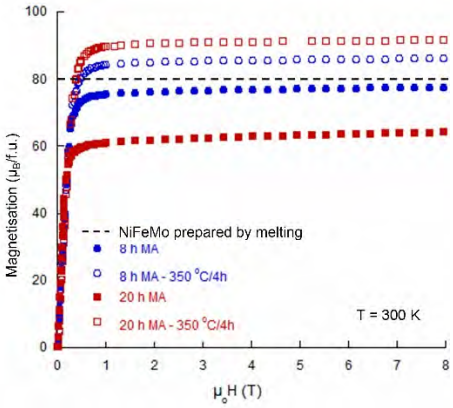

Fig. 9. Influence of annealing at 350 °C/4 hours on the magnetization value of Supermalloy (79Ni16Fe5Mo, wt. %) powders wet-milled for 8 and 20 hours.

CONCLUSIONS

The mechanosynthesis route is a powerful tool for producing soft magnetic nanocrystalline materials, both alloys and ceramic compounds. A large variety of Ni-Fe alloy have been successfully produced by mechanical alloying in nanocrystalline state. Also, by reactive milling Cu, Zn and Ni ferrites with cubic spinel structure have been produced effectively. In both cases the structure is formed progressively upon increasing the milling time. The alloying time needed for fully obtaining the desired phase is depending on the processed materials. For both, alloys and ferrites a contamination of the powders with iron provided by vials and ball for prolonged milling times was noticed. The crystallites size is in nanometric range when the alloy/compound starting to form. The annealing, in general, improve the magnetic characteristic of the as-milled samples. The structural and magnetic characteristics are strongly dependent on the synthesis conditions. The magnetic measurements

show a decrease of the magnetisation upon milling process, with a strong restauration after annealing. The thermomagnetic measurement is a strong instrument in observation of the alloys formation and theirs iron contamination for large milling times.

REFERENCES

[1] C. Suryanarayana, *Int. Mater. Reviews,* 40, 41 (1995).
[2] K. Lu, *Mater. Sci. Eng.,* R16, 161 (1996).
[3] S.C. Tjong, H. Chen, *Mater. Sci. Eng.,* R41, 1 (2004).
[5] G. Herzer, Nanocrystalline Soft Magnetic Alloys, in Handbook of Magnetic Materials, Ed. by K.H.J. Buschow, Elsevier Science BV (1997).
[6] G. Herzer, *Physica Scripta,* T49, 307 (1993).
[7] V. Šepelák, I. Bergmann, S. Kips, K.D. Becker, *Z. Anorg. Allg. Chem.,* 631, 993 (2005).
[8] I. Chicinaş, V. Pop, O. Isnard, *J. Magn. Magn. Mater.,* 242-245, 885 (2002).
[9] I. Chicinaş, V. Pop, O. Isnard, J.M. Le Breton, J. Juraszek, *J. Alloys Compd.,* 352, 34 (2003).
[10] V. Pop, O. Isnard, I. Chicinaş, *J. Alloys Compd.,* 361, 144 (2003).
[11] I. Chicinaş, V. Pop, O. Isnard, *J. Mater. Sci.,* 39, 5305 (2004).
[12] O. Isnard, V. Pop, I. Chicinaş, *J. Magn. Magn. Mater.,* 290-291, 1535 (2005)
[13] Z. Sparchez, I. Chicinaş, O. Isnard, V. Pop, F. Popa, *J. Alloys Compd.,* 434–435, 485 (2007).
[14] F. Popa, O. Isnard, I. Chicinaş, V. Pop, *J. Magn. Magn. Mater.,* 316, e900 (2007).
[15] V. Pop, I. Chicinaş, *J. Optoelectron. Adv. Mater.*, 9, 1478 (2007).
[16] B.V. Neamtu, O. Isnard, I. Chicinaş, V. Pop, *IEEE Trans. Magn.,* 46, 424 (2010).
[17] F. Popa, O. Isnard, I. Chicinaş, V. Pop, J*. Magn. Magn. Mater.*, 322, 1548 (2010).
[18] B.V. Neamtu, I. Chicinaş, O. Isnard, F. Popa,V. Pop, *Intermetallics*, 19, 19 (2011).
[19] T.F. Marinca, I. Chicinaş, O. Isnard, V. Pop, *Optoelectron. Adv. Mater. - Rapid Commun.,* 5, 39 (2011).
[20] B.V. Neamţu, O. Isnard, I. Chicinaş, V. Pop, *J. Alloys Compd.,* 509, 3632 (2011).
[21] T.F. Marinca, I. Chicinaş, O. Isnard, V. Pop, F. Popa, *J. Alloys Compd.,* 509, 931 (2011).
[22] F. Popa, I. Chicinaş, O. Isnard, V. Pop, *J. Therm. Anal Calorim.,* 110, 295 (2012).
[23] F. Popa, O. Isnard, I. Chicinaş, V. Pop, *J. Alloys Compd.,* 554, 39 (2013).
[24] I. Chicinaş, T.F. Marinca, B.V. Neamţu, F. Popa, O. Isnard, V. Pop, *IEEE Trans. Magn.*, 50, Article Number: 2800704 (2014).
[25] I. Chicinaş, T.F. Marinca, B.V. Neamţu, P. Pascuta, V. Pop, *J. Therm. Anal. Calorim.,* 118, 1269 (2014).
[26] P. Scherrer, *Nachr Gött Matematisch Phys Klasse I*, 98 (1918).
[27] G.K. Williamson, W.H. Hall, *Acta Metall.*, 1, 22 (1953).
[28] F. Popa, Ph. D. Thesis, Technical University of Cluj-Napoca and Joseph Fourier University, Grenoble, 2008.

[29] B.V. Neamtu, Ph. D. Thesis, Technical University of Cluj-Napoca and Joseph Fourier University, Grenoble, 2010.
[30] T.F. Marinca, Ph. D. Thesis, Technical University of Cluj-Napoca, 2011.
[31] T. F. Marinca, I. Chicinaş, V. C. Pricǎ, F. Popa and B. V. Neamţu, *Mater. Sci. Forum,* 672, 149 (2011).
[32] T. Verdier, V. Nachbaur, J. Malick, *J. Solid State Chem.,* 178, 3243 (2005).
[33] J. E. Zanetti and G. Egloff, *J. Ind. Eng. Chem.,* 9, 350 (1917).
[34] S. Ahmed, A. Aitani, F. Rahman, A. Al-Dawood, F. Al-Muhaish, *Appl. Catalysis A,* 359, 1 (2009).
[35] B.V. Neamțu, O. Isnard, I. Chicinaș, C. Vagner, N. Jumate, P. Plaindoux, *Mater. Chem. Phys.,* 125, 364 (2011).

STUDIA UBB PHYSICA, Vol. 66 (LXVI), 1-2, 2021, pp. 31-37
(RECOMMENDED CITATION)
doi:10.24193/subbphys.2021.03

SERS INVESTIGATIONS OF 2-METHOXY-2-METHYLPROPYLISONITRILE (MIBI) AND ITS TECHNETIUM COMPLEX

GEORGE CRIȘAN[1,2], ANA MARIA MACEA[1], GABRIEL ANDRIEȘ[2], VASILE CHIȘ[1*]

ABSTRACT. Technetium radiopharmaceuticals remain the most widely available and cost-effective compounds used in nuclear medicine imaging. However, exact information regarding the chemical structure of these compounds is scarce. In this study we present a spectroscopic investigation of Hexakis (2-methoxy-2-methylpropylisonitrile) (MIBI) Technetium (^{99m}Tc) (^{99m}Tc-sestamibi). Surface Enhanced Raman Scattering spectra of the ligand and the Technetium sestamibi complex were recorded. For the later, the measurements were recorded in solution as administered to patients and at different moments from the time of preparation in order to monitor its stability. The information provided by the vibrational characterization of the MIBI ligand allowed us to understand spectroscopic features pertaining to the SERS spectra of the Technetium complex.

Keywords: *Technetium; radiopharmaceuticals; SPECT; MIBI; SERS.*

1. INTRODUCTION

^{99m}Tc-Sestamibi is a Technetium based radiopharmaceutical commonly used for Single Photon Emission Computed Tomography (SPECT) imaging. Since its introduction, as a cardiac imaging agent [1], it rapidly became a standard in nuclear medicine clinical practice for myocardial perfusion scans and parathyroid adenoma identification [2, 3]. The radiopharmaceutical, consisting of a ^{99m}Tc core bound to six 2-methoxy-2-methylpropylisonitrile (MIBI) ligands, presents an uptake mechanism

[1] *Babeş-Bolyai University, Faculty of Physics, 1 Kogălniceanu, RO-400084 Cluj-Napoca, Romania*
[2] *Department of Nuclear Medicine, County Clinical Hospital, 3-5 Clinicilor, RO-400006 Cluj-Napoca, Romania*
[*] *Corresponding author: vasile.chis@phys.ubbcluj.ro*

dependent on mitochondrial and plasma membrane potentials, extending its use in oncology applications e.g. breast cancer imaging and Multidrug Resistance Mutation (MDR1) expression studies [4, 5].

Since molecular and electronic structure information is missing for both the Technetium complex and the MIBI ligand, we previously presented a joint experimental and computational study of the ligand. Using conformational and vibrational analysis based on DFT calculations in both harmonic and anharmonic approximations we obtained an accurate characterization of the Raman spectrum of MIBI [6].

The aim of the present study is to extend the previously reported investigation on the ^{99m}Tc-sestamibi complex. Due to the fact that in nuclear medicine studies radiopharmaceuticals are injected in very small quantities, we considered the Surface Enhanced Raman Scattering (SERS) technique as the best suited approach for this purpose. Thus, we present here an analysis of the SERS spectrum for the MIBI ligand, as well as the SERS spectrum of ^{99m}Tc-Sestamibi in the solution administered to patients. We will focus also on the observed differences that appear in the SERS spectrum at different time intervals after the radiolabelling of the Technetium complex.

2. EXPERIMENTAL DETAILS

2.1. Chemicals

As received aqueous solution of MIBI (Manchester Organics Ltd., 98.3% purity) was used without further purification.

Sodium pertechnetate solution was obtained following the daily elution of an Ultratechnekow^{TM} FM 12.9 GBq ^{99m}Tc generator purchased from Curium.

^{99m}Tc-Sestamibi solution was obtained using the Technescan^{TM} Sestamibi kit for radiopharmaceutical preparation purchased from Mallinckrodt Medical. The radiolabeling process was performed during regular clinical practice, following the manufacturer's instructions. Briefly, a 3ml saline solution of sodium pertechnetate was aseptically added to a vial from the preparation kit containing 1 mg [Tetrakis (2-methoxy-2-methylpropylisonitrile)copper(I)] tetrafluroborate. The vial was then placed in a water bath at 100^{o}C for 10 minutes and left to cool at room temperature for 15 minutes.

SERS measurements for both MIBI and ^{99m}Tc-Sestamibi were performed using an Ag-colloid as substrate, prepared by the Leopold-Lendl method [7]. We found that a 1:9 sample to substrate ratio yielded the best results for both MIBI and ^{99m}Tc-sestamibi measurements.

All radioactive solutions were handled according to radioprotection guides and local regulations.

2.2. Instrumentation

The SERS spectra were recorded on an Invia Reflex confocal Raman spectrometer (Renishaw, UK), equipped with a RenCam CCD detector and using the 532 nm excitation line from a Cobolt Diode Pumped Solid State (DPSS) laser and a diffraction grating with 1800 lines mm^{-1}.

3. RESULTS AND DISCUSSIONS

The interpretation of the SERS spectra is made in accordance with our previous work in which we presented a full assignment of the Raman spectra of the MIBI ligand based on DFT calculations, taking into account conformer analysis and both, the harmonic and anharmonic approximations [6].

Figure 1 shows the SERS spectrum of the MIBI ligand of 10^{-4}M concentration. It is worth mentioning that we previously found the limit of detection of 10^{-3}M by using the Raman technique [6]. Comparing the Raman and SERS spectra of MIBI it is evident that the main band observed in the Raman spectrum are also observed in the SERS spectrum, some of them being enhanced and/or shifted.

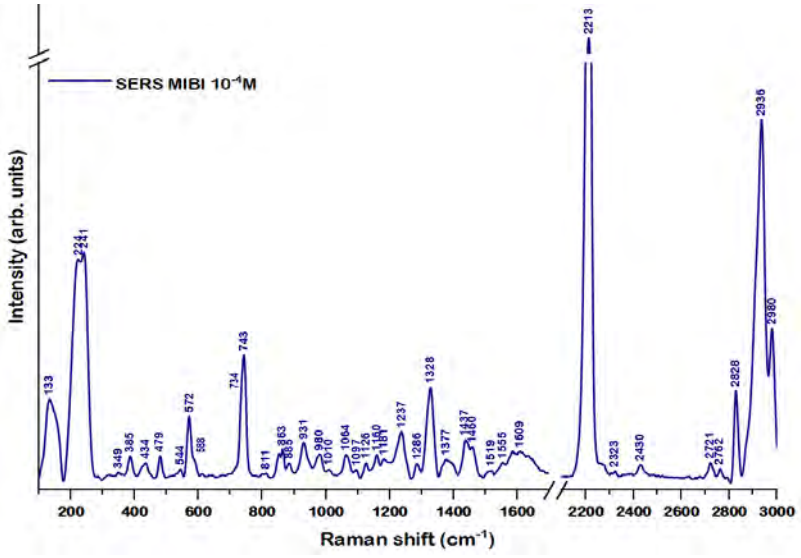

Figure 1. SERS spectrum of MIBI at 10^{-4}M

The most striking difference both in position and intensity is observed for the band at 2213 cm^{-1} in the SERS spectrum (2148 cm^{-1} Raman) assigned to a C≡N stretch mode [6]. The band suffers a significant blue-shift of 65 cm^{-1} and presents the largest enhancement. Other bands with significantly increased wavenumbers can be observed in the fingerprint region at 572, 479, 434 and 385 cm^{-1}. On the other hand the bands at 2936, 1377, 1328, 1286, and 1064 cm^{-1} exhibit red-shifts between 7 and 16 cm^{-1}.

Slight increases in relative intensity can be observed for most of the bands in the fingerprint region, while significant enhancements are seen for the combined C-CH_2 stretch and CH_2 wagging mode at 1328 cm^{-1}, the 1237 cm^{-1} band assigned to C-CH_3 stretch and COC bend, and the doublet at 588/572 assigned to a COC and CNC bend.

The doublets observed in the SERS spectrum at 743/734 and 588/572 were proved to be due to contributions from different conformers [6]. The shoulder at 734 observed is less pronounced than in the Raman spectrum. For the second doubled we see that the band at 572 cm^{-1} suffers a blue-shift, and an increase in relative intensity. These changes can be attributed to the signal enhancement of certain conformers.

Important to note is the band located at 1377 which suffers a significant increase in intensity when compared to the Raman measurements. This band is accurately reproduced by the harmonic and especially the anharmonic calculations but was very weak on the experimental Raman spectra at either at 1M or 10^{-1}M concentration.

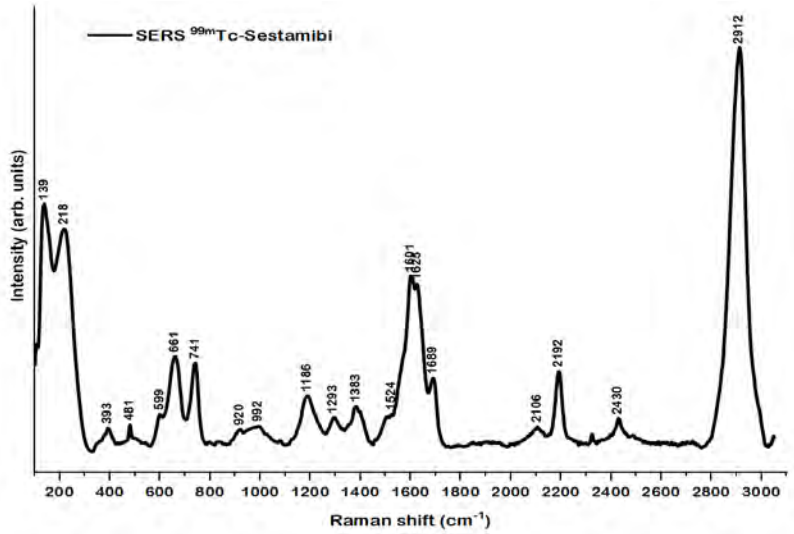

Figure 2. SERS spectrum of ^{99m}Tc-Sestamibi solution

In Figure 2 we present the SERS spectra of ^{99m}Tc-Sestamibi. The complex is considered to be stable for patient use within 8 hours after preparation. We can observe several bands characteristic to the MIBI ligand: 2912 cm^{-1} (CH_2 stretch), 2192 cm^{-1} (C≡N stretch), and 741 cm^{-1} (C-CH_3 and CO stretch). We note the presence of the band at 661 cm^{-1} that was not observed neither in the Raman or the SERS spectrum of the ligand. It is very probable that the band arises due to the excipients present in the kit that facilitate the formation of the Technetium complex.

In addition we performed measurements at different times from the moment of radiolabelling. Figure 3 shows the comparison between the SERS spectra of Tc-sestamibi at 4, 24, 54 and 106 hours from preparation. Comparing the first two we observe no significant change in band position and intensity in the first 24 hours. However we can observe three new, although weak, bands at 2952, 2835 and 1355 cm^{-1}. In contrast, the spectrum recorded at 56 hours from preparation shows significant changes. We observe new bands characteristic to the ligand, such as the doublets at 1455/1435 and 590/573 as well as the bands at 2829, 1288, 852, 808 and 349 cm^{-1}. Also, one can easily note the splitting of the band assigned to the C≡N stretch mode at 2193 cm^{-1}.

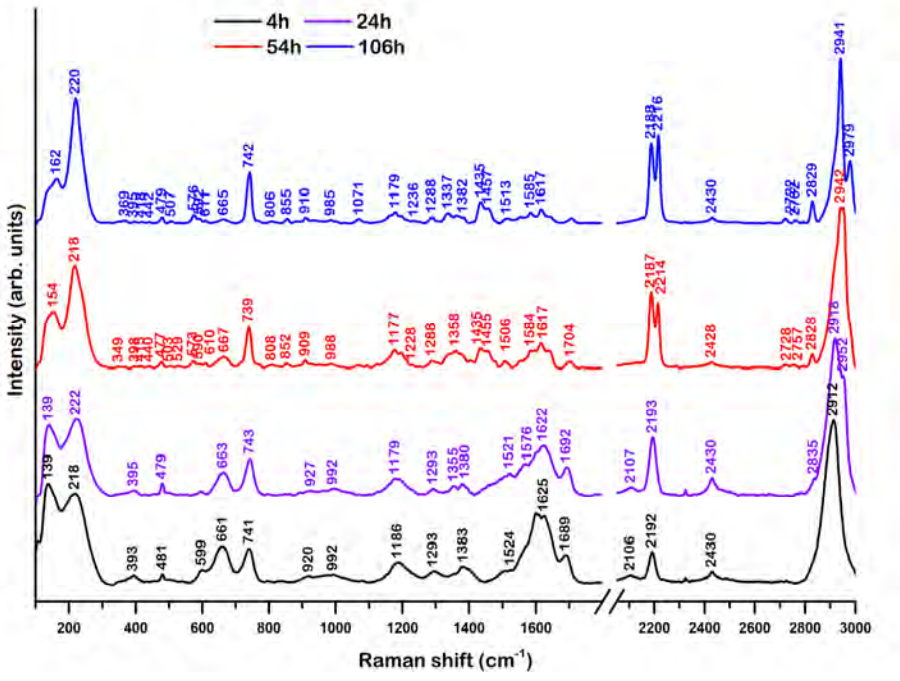

Figure 3. SERS spectra of ^{99m}Tc-Sestamibi at 2, 24, 54 and 106 hour from radiolabelling

The next spectrum, which was recorded at 106 hours, shows no significant differences in band positions with respect to that recorded at 54 hours after preparation. We can assume that the Technetium complex destabilizes between the second and third measurement.

The higher wavenumber component of the doublet recorded at 54 and 106 hours after the preparation (2216 cm^{-1}) is very close to that corresponding to the SERS spectrum of the unbound MIBI ligand (2213 cm^{-1}). Thus, most probably, the splitting of the C≡N band can be explained either by the appearance of free MIBI molecules adsorbed on the colloidal surface, besides the Tc-sestamibi complex which became slightly red-shifted with time.

4. CONCLUSIONS

SERS measurements on the MIBI ligand show good amplification of Raman bands even at concentration lower than the Raman detection limit, in particular the C≡N stretch at 2213 cm^{-1}. In addition we find good agreement between the experimental data and previously obtained results. This allows for a more confident characterization of the ^{99m}Tc-sestamibi. The SERS spectrum of the complex reveals several MIBI characteristic bands. We also observe that ^{99m}Tc-Sestamibi has a structural stability of at least 24 hours from the time of the radiolabelling process. However by this time most ^{99m}Tc atoms will have decayed to ^{99}Tc atoms which would make the complex inefficient for imaging.

ACKNOWLEDGMENTS

V. Chiş acknowledges the support of the CNCS-UEFISCDI Romania, grant PN-III-P4-ID-PCCF-2016-0112.

REFERENCES

[1] D. Berman, H. Kiat, J. Maddahi, The new ^{99m}Tc myocardial perfusion imaging agents: ^{99m}Tc-sestamibi and ^{99m}Tc-teboroxime, *Circulation*, 84(3 Suppl) (1991) I7-I21.

[2] D. Agostini, V. Roule, C. Nganoa, N. Roth, R. Baavour, J.J. Parienti, F. Beygui, A. Manrique, First validation of myocardial flow reserve assessed by dynamic 99mTc-sestamibi CZT-SPECT camera: head to head comparison with 15O-water PET and fractional flow reserve in patients with suspected coronary artery disease. *Eur. J. Nucl. Med. Mol. Imaging,* 45 (2018) 1079–1090.

[3] J. Whitman, I. Allen, E. Bergsland, I. Suh, T. Hope, Assessment and comparison of fluorocholine PET and sestamibi scans in identifying parathyroid adenomas: a meta-analysis, *J. Nucl. Med.*, 62(9) (2021) 1285-1291.
[4] S. Del Vecchio, M. Salvatore, Bonanno, O. Schillaci, ^{99m}Tc-MIBI in the evaluation of breast cancer biology. *Eur. J. Nucl. Med. Mol. Imaging*, 31 (2004) S88-S96.
[5] N.H. Hendrikse, E.J.F Franssen, W.T.A van der Graaf, C. Meijer, D.A. Piers, E.G.E. Vries, ^{99m}Tc-sestamibi is a substrate for P-glycoprotein and the multidrug resistance-associated protein, *Brit. J. Cancer,* 77 (1998) 353–358.
[6] G. Crisan, A. Macea, G. Andrieș, V. Chiș, Experimental and computational Raman spectroscopies applied to 2-methoxy-2-methylpropylisonitrile (MIBI) ligand of 99mTc-sestamibi radiopharmaceutical, *J. Mol. Struct.*, 1246 (2021) 131159.
[7] N. Leopold, B. Lendl, A New Method for Fast Preparation of Highly Surface-Enhanced Raman Scattering (SERS) Active Silver Colloids at Room Temperature by Reduction of Silver Nitrate with Hydroxylamine Hydrochloride, *J. Phys. Chem. B,* 107 (2003) 5723-5727.

STUDIA UBB PHYSICA, Vol. 66 (LXVI), 1-2, 2021, pp. 39-46
(RECOMMENDED CITATION)
doi:10.24193/subbphys.2021.04

XPS ON $Mn_{0.95}Dy_{0.05}NiSb$ HEUSLER ALLOY

R. DUDRIC[1*], R. GRASIN[2], M. NEUMANN[3], R. TETEAN[1]

ABSTRACT. XPS results on $Mn_{0.95}Dy_{0.05}NiSb$ Heusler alloy are presented. The compound is single phase with a *C*1*b* type cubic structure. All the experimental results suggest that the rare earth atoms entered in the lattice and they are not forming second phases. An exchange splitting of Mn 3s core-level spectrum of about 4.6 eV was shown, giving a direct evidence of the local magnetic moments on Mn sites. The Ni 3d states are giving the major contribution to the XPS valence band spectra. The Ni 3d satellite peak situated around 6 eV was attributed to the fact that the Ni 3d states in the valence band are not fully occupied. However, the Ni 3d band is almost full in this alloy and the Stoner criterion for the existence of a magnetic moment on Ni sites is no longer fulfilled.

Keywords: *Heusler alloys, X-ray photoelectron spectroscopy, valence band spectra.*

INTRODUCTION

Half metallicity was predicted by de Groot and his collaborators in a pioneering paper published in 1983 for the Heusler alloy MnNiSb [1]. These materials present a metallic behavior for one spin band and a semiconducting one for the opposite spin band. Being metals for one spin projection and semiconductors for the opposite one they have, in magnitude, different spin contributions to electronic transport properties, which can result in a huge magnetoresistance for heterostructures containing Half-metallic ferromagnets. These compounds are either ferromagnetically or ferrimagnetically ordered and were predicted to have perfect spin polarization at the Fermi level. NiMnSb crystallizes in the cubic structure of *C*1*b* type with space group $F\bar{4}3m$. This structure can be described as

[1] *Babes-Bolyai University, Faculty of Physics, Kogalniceanu 1, RO-400084, Cluj Napoca, Romania*
[2] *SC Robert Bosch S.R.L., Str. Robert Bosch no. 1, 407350 Jucu, Cluj, Romania*
[3] *University of Osnabrueck, Fachbereich Physik, 49069 Osnabrueck, Germany*
[*] *Corresponding author: roxana.dudric@ubbcluj.ro*

three interpenetrating fcc lattices of Ni, Mn, and Sb. It was shown that in order to obtain the minority spin gap it is necessary to take into account the Mn-*d*-Sb-*p* and Mn-*d*-Ni-*d* interactions. The large exchange splitting of the Mn atoms, producing the local Mn magnetic moment is crucial to induce a half-metallic structure. The spin polarized calculations reveal that the position of t_{2g} and e_g Ni states are slightly changed comparing the minority and majority spin channels, so that the exchange splitting on Ni is small. The magnetic moment calculation gives values around 3.7 μ_B for Mn and 0.3 μ_B for Ni respectively [1-8]. Spin–orbit interaction causes the mixing of the two spin directions, the result being a reduction of the spin polarization of the conduction electrons even at zero temperature. In order to avoid the reduction of spin-polarization, special care has to be taken. Attema et al. have shown that a properly chosen element from the lanthanide series as a substitute would increase the magnetic anisotropy and at the same time would contribute in keeping a significant spin-polarization [9]. The 4f electrons are not directly involved in chemical bonding and show a strong spin–orbit interaction and are energetically well separated from the Fermi energy. Holmium was proposed as substituent considering both the spin moment and the orbital moment. It was shown that the half-metallic properties are completely conserved if Mn is substituted with a rare earth metal [9]. According to the authors, the size of the effect is not determined by the strength of the spin–orbit coupling, but limited by the interaction between the magnetic moments of manganese and holmium.

In this paper we have investigated the effect of Dy substitution for Mn on the physical properties of NiMnSb compounds. X-ray diffraction and X-ray photoelectron spectroscopy (XPS) were used to characterize the samples. From the experimental data we concluded that the heavy rare-earth atoms have entered in the C1*b* structure.

EXPERIMENTAL

The $Mn_{0.95}Dy_{0.05}NiSb$ compound was prepared by arc melting of the constituent elements in a purified argon atmosphere using high purity Ni (99.8%), Mn (99.9%), Sb (99.999%) and Dy (99.95%) ingots (Alfa Aesar, Jonson & Matthey, Karlsruhe, Germany). The ingots were turned around and remelted up to 10 times. The samples were sealed in tantalum foil and heat treated in vacuum at 1000 ºC for 5 days. The crystal structure of the studied samples was checked by X-ray Diffraction using a Bruker 8 XD diffractometer at the Ioan Ursu Institute Cluj Napoca. XPS spectra were recorded at room temperature using a SPECS Multifunctional surface analysis system with monochromatized Al Kα radiation, located at Osnabrueck University.

The pressure in the ultra-high vacuum chamber was in the 10^{-10} mbar range. In order to avoid the surface contamination, the sample was crushed in situ and the surface cleanness was checked by monitoring the oxygen and carbon 1s core levels. It was found that the contamination was almost absent, so we can conclude that the XPS spectra are representative of the bulk.

In Fig.1 the survey spectra of the $Mn_{0.95}Dy_{0.05}NiSb$ is presented.

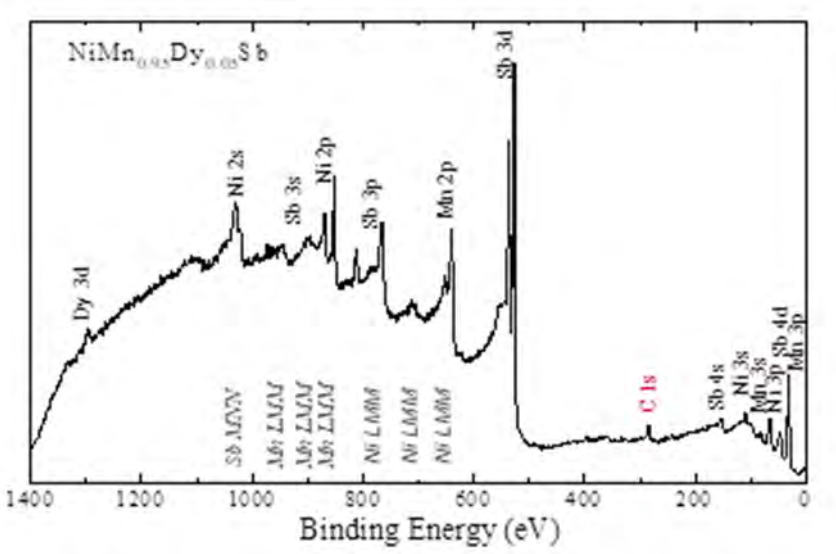

Fig. 1. XPS survey spectra of $Mn_{0.95}Dy_{0.05}NiSb$.

One can see that the sample is not oxidated, since the oxygen O 1s core level (around 531 eV) was almost absent. The small C 1s core line indicates the low level of sample contamination.

RESULTS AND DISCUSSIONS

The X-ray diffraction analysis show, in the limit of experimental errors, that the compound is single phase with a *C*1*b* type cubic structure (space group $F\bar{4}3m$). The lattice parameter was found to be 0.594(3) nm, somewhat higher than that of the pure compound (0.593(1) nm [10]). This small increase could be explained by the higher radius of Dy ion compared to Mn ion.

XPS core level and valence band spectra provide important information on the electronic structure of 3d transition metal alloys and compounds. Multiplet splitting and satellite emission in the core-level photoelectron spectra represent the interaction between the core hole and the valence electrons and are related to the electronic structure of the bound atoms. The localization or delocalization of the 3d valence electrons, screening, and charge transfer processes can influence the core-level photoelectron spectra. The multiplet splitting of the XPS core levels show the existence of localized magnetic moments of transition metals ions. The splitting of the Mn 3*s* core level in MnNiSb and $Mn_{0.95}Dy_{0.05}NiSb$ is presented in Fig. 2. The Mn 3s core-level spectra show an exchange splitting of about 4.6 eV, arising from the exchange interaction between the core hole and open 3d shell. A high-spin density of the 3d electrons on Mn sites is revealed by the high value of the energy separation and proof the existence of localized magnetic moments confined on Mn sites.

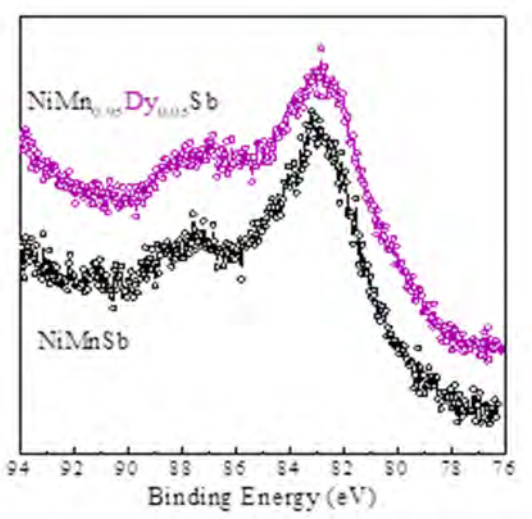

Fig. 2. XPS Mn 3s core level spectra of $Mn_{0.95}Dy_{0.05}NiSb$ and MnNiSb

The Ni 2p XPS spectra for $Mn_{0.95}Dy_{0.05}NiSb$ alloy are shown in Fig. 3.

The Ni 2p spectra in NiMnSb and in metallic Ni are also plotted. A satellite in the Ni 2p core level spectra, at about 6.5 eV higher binding energy than the main lines can be observed, suggesting the *d* character in the unoccupied bands. The intensity of this satellite in both investigated compounds is much smaller than in pure Ni. This show that, in these alloys, the Ni 3d band is almost full and the Stoner criterion for the existence of a magnetic moment on Ni sites is no longer fulfilled.

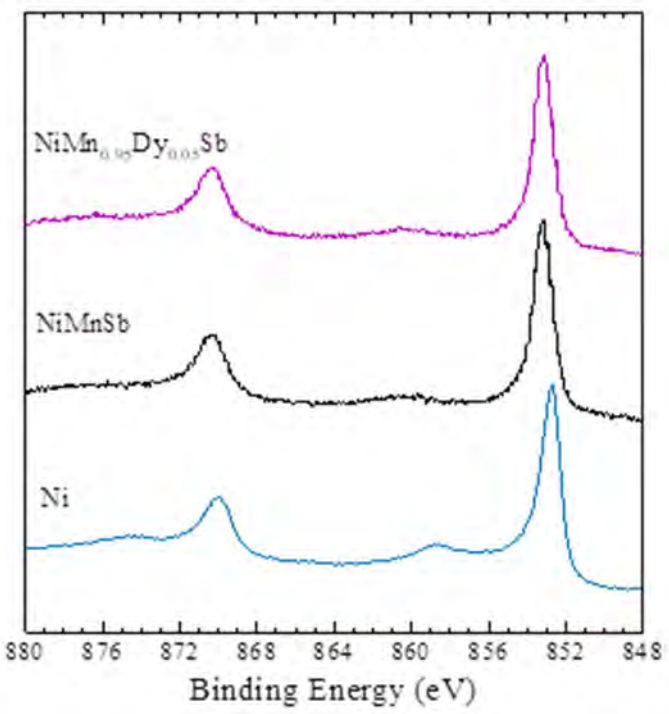

Fig. 3. Ni 2p XPS spectra of Ni, NiMnSb and $Mn_{0.95}Dy_{0.05}NiSb$ alloys

The core-level spectra in the region of Sb 4s and Dy 4d binding energies are presented in Fig. 4. Information about the atomic bonding can be subtracted from here by extracting the binding energies of the Dy atom at the 4d core shell, comparing with the values in pure metals and in oxides from Handbook of X-Ray Photoemission Spectroscopy (HXPS). The 4f binding energy was found to be 9 eV and 4d binding energy 155 eV. The experimentally determined binding energies, in the region of 4f and 4d core shells, are different from that of the pure element (8 eV and 152 eV from HXPS) or it's oxide (168 eV in Dy_2O_3 according to HXPS). These results allow us to conclude that the rare earth element occupies a lattice position in the $Mn_{0.95}Dy_{0.05}NiSb$ alloy.

The Dy concentration alloys in $Mn_{0.95}Dy_{0.05}NiSb$ alloy was calculated considering the intensity ratio of the Sb 4s and the Dy 4f peaks. The calculated values of the concentrations are presented in Table 1. One can see that the experimentally determined intensities are in a quiet good agreement with the theoretical ones, which means, that in the limit of the experimental errors, the rare earth elements entered in the composition of the $Mn_{0.95}Dy_{0.05}NiSb$ alloy.

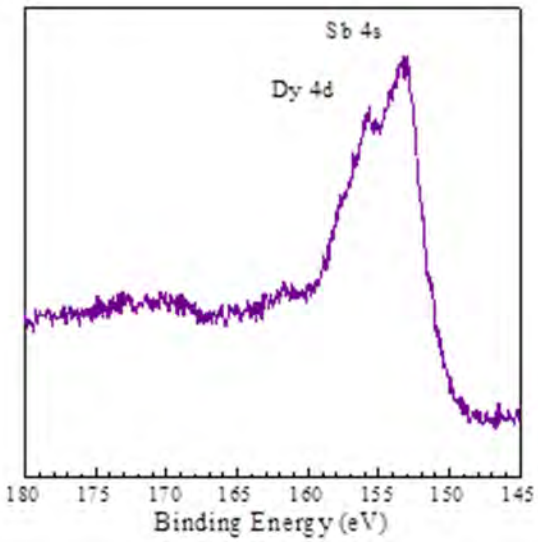

Fig. 4. Core-level spectra in the region of Sb 4s and Dy 4d binding energies

Table. 1. The calculated concentration of Sb and Dy in $Mn_{0.95}Dy_{0.05}NiSb$.

Core level	Cross section	Concentration	Theoretical int.	Exp. Int.
Sb 4s	0.011	1.00	1.00	1.00
Dy 4d	0.140	0.05	0.71	0.60

The XPS spectra of the valence band region of $Mn_{0.95}Dy_{0.05}NiSb$ compared with MnNiSb alloy is shown in Fig. 5.

The Ni 3d states are giving the major contribution to the XPS valence band spectra, the typical feature being around 1 eV. One can see that this feature is not shifted. It was expected that this feature will give the main contribution, considering that the Ni 3d cross section for Al Kα radiation is about four times larger than the Mn 3d cross section situated at about ~2.8 eV. The peak at around ~6 eV is a satellite feature of the Ni 3d. These satellite features can be attributed to the fact that the Ni 3d states in the valence band are not fully occupied. The main difference between the valence band spectra of $Mn_{0.95}Dy_{0.05}NiSb$ and NiMnSb is between 8.5 eV and 10.5 eV, due to the Dy 4f states contribution. By subtracting the normalized XPS valence band spectra of NiMnSb, from the normalized spectra of $Mn_{0.95}Dy_{0.05}NiSb$, it was found that the binding energy of the Dy 4f core level is around 9.5 eV at higher

binding energy than in metallic rare earth (inset of Fig. 5). We can conclude that the Dy atoms occupy atomic positions in the NiMnSb cell. The peak at around ~10-11 eV is also present in all investigated alloys and is assigned to the Sb 5s states.

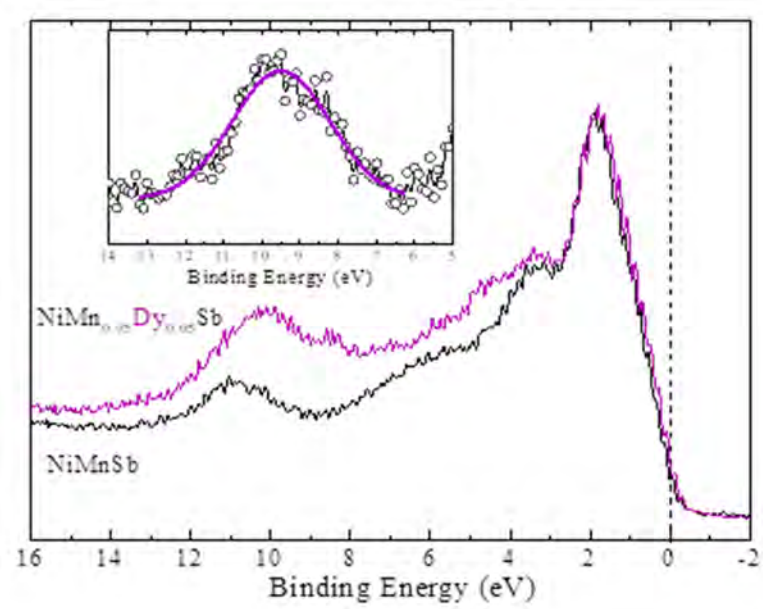

Fig. 5. XPS valence band spectra of NiMnSb and $Mn_{0.95}Dy_{0.05}NiSb$ alloys

CONCLUSIONS

XPS results on $Mn_{0.95}Dy_{0.05}NiSb$ Heusler alloy are presented. The prepared compound is single phase with a *C1b* type cubic structure. The survey spectra of the $Mn_{0.95}Dy_{0.05}NiSb$ confirm that the sample is not oxidated or contaminated.

An exchange splitting of Mn 3s core-level spectrum of about 4.6 eV was shown. The high value of the energy separation indicates a high-spin density of the 3d electrons on Mn sites and proof the existence of localized magnetic moments confined on Mn sites.

A satellite in the Ni 2p core level spectra, at about 6.5 eV higher binding energy than the main lines is shown, suggesting the *d* character in the unoccupied bands. The intensity of this satellite in parent and doped compounds is much smaller than in pure Ni showing that the Ni 3d band is almost full and the Stoner criterion for the existence of a magnetic moment on Ni sites is no longer fulfilled.

The experimentally determined binding energies, in the region of 4f and 4d core shells, are different from that of the pure element or it's oxides. These results allow us to conclude that the rare earth element occupies a lattice position in the $Mn_{0.95}Dy_{0.05}NiSb$ alloy.

The valence-band is dominated by the Ni 3d states. The Ni satellite is separated by approximately 6 eV from the centroids of the valence bands and can be attributed to the presence of the d character in the unoccupied bands. The main difference between the valence band spectra of $Mn_{0.95}Dy_{0.05}NiSb$ and NiMnSb is between 8.5 eV and 10.5 eV, due to the Dy 4f states contribution.

All the experimental results suggest that the rare earth ions occupy atomic positions in the lattice and they are not forming secondary phases.

REFERENCES

[1] R.A. de Groot, F.M. Mueller, P.G. van Engen, K.H.J. Buschow, *Phys. Rev. Lett*., 50, 2024 (1983).
[2] V.Y. Irkhin, M.I. Katsnelson, *European Physical Journal B*, 30, 481 (2002).
[3] A. Yamasaki, L. Chioncel, A. I. Lichtenstein and O. K. Andersen, *Phys. Rev. B*, 74, 024419 (2006).
[4] Öğüt, S., and K. M. Rabe, *Phys. Rev. B*, 51, 10443 (1995).
[5] I. Galanakis, and P. Mavropoulos, *J. Phys.: Condens. Matter,* 19, 315213 (2007).
[6] Kulatov, E., and I. I. Mazin, *J. Phys.: Condens. Matte*r, 2, 343 (2003).
[7] B. R. K Nanda and I. Dasgupta, *J. Phys.: Condens. Matter*, 15, 7307 (2003).
[8] I. Galanakis, P. H. Dederichs, N. Papanikolaou, *Phys. Rev. B*, 66, 134428 (2002).
[9] J.J. Attema, C.M. Fang, L. Chioncel, G.A. De Wijs, A.I. Lichtenstein, R.A. De Grootet, *J. Phys. Condens. Matter*, 16, S5517 (2004).
[10] R. Grasin, C. Rusu, A. Laslo, R. Dudric, S. Mican, M. Neumann, R. Tetean, *Phys. Status Solidi B,* 249, 1779 (2012).

STUDIA UBB PHYSICA, Vol. 66 (LXVI), 1-2, 2021, pp. 47-53
(RECOMMENDED CITATION)
doi:10.24193/subbphys.2021.05

LORENTZ NUMBER WITH PHENOMENOLOGICAL TRANSMISSION

I. GROSU[1]

ABSTRACT. We analyzed the Lorentz number for thermoelectric phenomena in the case of electronic systems, using the Landauer-Büttiker method. For the transmission coefficient we will adopt two simple phenomenological forms, constant and linear. The case of graphene with a quadratic transmission is also analyzed.

Keywords: *Thermoelectric properties, Wiedemann-Franz law, Lorentz number, Transmission, Electrons, Graphene.*

Since their discovery thermoelectric effects [1, 2, 3] have attracted attention through their theoretical explanation and many applications. At a given temperature T, in common conductors, the ratio between the heat conductance and the product temperature-electrical conductance is constant and equal to the Lorentz number $\mathcal{L}$. This result is a consequence of the fact that both charge and heat are carried by the same particles [4, 5], and this ratio is called the Wiedemann-Franz law [6]. Deviations from the Wiedemann-Franz law indicate departures from the Fermi liquid behavior [7]. In mesoscopic systems, Coulomb interaction and charge quantization can also lead to departures from the Wiedemann-Franz law [8, 9]. The importance of the Wiedemann-Franz ratio lies in the fact that the figure of merit for thermoelectric conversion ZT is directly proportional to the inverse of this ratio. In this respect it is desirable to maximize the charge flow and to minimize that of heat. The thermoelectric response of nanostructures has increased the interest in this research area [10, 11]. Recently, the thermoelectric transport properties in graphene connected molecular junctions and in interacting quantum dots in graphene were studied in Refs. [12, 13]. The effect of magnetic field on thermoelectric properties of monolayer graphene was analyzed in [14].

[1] *Babes-Bolyai University, Faculty of Physics, 1 Kogalniceanu str., 400084 Cluj-Napoca, Romania, ioan.grosu@ubbcluj.ro*

In this paper we will calculate the Lorentz number taking into account the electronic system and for two simple phenomenological forms of the transmission factor (constant and linear). Then we will discuss the Lorentz number for the case of graphene with a quadratic transmission. The obtained results can be useful in order to find out the efficiency of thermoelectric conversion.

The Wiedemann-Franz law states that the ratio between electronic thermal conductivity (K_{el}) and electrical conductivity (σ) is proportional to temperature:

$$\frac{K_{el}}{\sigma} = \mathcal{L}\,\mathrm{T} \tag{1}$$

where $\mathcal{L}$ is the Lorentz number. In the case of an ideal Fermi gas, $\beta\mu \gg 1$ ($\beta=1/k_BT$, k_B - the Boltzmann constant, and μ is the chemical potential), the Lorentz number is:

$$\mathcal{L}_0 = \frac{\pi^2}{3}\left(\frac{k_B}{e}\right)^2 \tag{2}$$

e – is the electron charge. For mesoscopic systems, in the presence of leads, using the Landauer-Büttiker formalism, one can express the Lorentz number through the energy dependent transmission $T(\varepsilon)$ by the following formula:

$$\mathcal{L} = \frac{K_{el}}{\sigma T} = \frac{L_0 L_2 - L_1^2}{e^2 T L_0^2} \tag{3}$$

where:

$$L_n = \frac{g}{h}\int d\varepsilon\; T(\varepsilon)\left(-\frac{\partial f}{\partial \varepsilon}\right)(\varepsilon-\mu)^n \tag{4}$$

with *n*= 0, 1, 2. Here *g* is the degeneracy (for classical Fermi gas $g=g_s=2$, and for graphene $g=g_sg_v=2x2=4$, where g_s and g_v are the spin and valley degeneracies), and *f*(ε) is the Fermi-Dirac distribution function. Using:

$$f(\varepsilon) = \frac{1}{2}\left[1-\tanh\frac{\beta(\varepsilon-\mu)}{2}\right] \tag{5}$$

we obtain:

$$L_n = \frac{g\beta}{4h}\int d\varepsilon\; T(\varepsilon)\;\frac{(\varepsilon-\mu)^n}{\left(\cosh\left[\frac{\beta(\varepsilon-\mu)}{2}\right]\right)^2} \tag{6}$$

where *h* is the Planck constant. In the following we will analyze the Lorentz number, using several simple forms for the transmission.

Case 1: Electronic system with $T(\varepsilon)=T_0$=const.

In this case:

$$L_0 = \frac{g\beta T_0}{4h}\int_0^\infty d\varepsilon\;\frac{1}{\left(\cosh\left[\frac{\beta(\varepsilon-\mu)}{2}\right]\right)^2} = \frac{gT_0}{2h}\left[1+\tanh\left(\frac{\beta\mu}{2}\right)\right] \tag{7}$$

When $\beta\mu \gg 1$ (low temperatures):

$$L_0 \cong \frac{gT_0}{h} \tag{8}$$

Then:

$$L_1 = \frac{g\beta T_0}{4h}\int_0^\infty d\varepsilon \; \frac{\varepsilon - \mu}{\left(\cosh\left[\frac{\beta(\varepsilon-\mu)}{2}\right]\right)^2} \tag{9}$$

or:

$$L_1 = \frac{gT_0}{\beta h}\left\{ln\left[2\cosh\left(\frac{\beta\mu}{2}\right)\right] - \frac{\beta\mu}{2}\tanh\left(\frac{\beta\mu}{2}\right)\right\} \tag{10}$$

which, for $\beta\mu \gg 1$, reduces to:

$$L_1 \cong \frac{gT_0\mu}{h}\, e^{-\beta\mu} \to 0 \tag{11}$$

Finally, L_2 is:

$$L_2 = \frac{g\beta T_0}{4h}\int_0^\infty d\varepsilon \; \frac{(\varepsilon - \mu)^2}{\left(\cosh\left[\frac{\beta(\varepsilon-\mu)}{2}\right]\right)^2} \tag{12}$$

After integration we obtain:

$$L_2 = \frac{2gT_0}{h\beta^2}\left\{\frac{\pi^2}{6} + polylog\left(2, -e^{-\beta\mu}\right) - \beta\mu\, ln\left[2\cosh\left(\frac{\beta\mu}{2}\right)\right] + \left(\frac{\beta\mu}{2}\right)^2\left[1 + \tanh\left(\frac{\beta\mu}{2}\right)\right]\right\} \tag{13}$$

where *polylog(n,y)* is the polylogarithmic function. In the low temperatures limit, $\beta\mu \gg 1$, L_2 becomes:

$$L_2 \cong \frac{2\pi^2 gT_0}{6h\beta^2} \tag{14}$$

Having these results, and in the low temperatures limit, we obtain for the Lorentz number:

$$\mathcal{L} = \frac{\pi^2}{3}\left(\frac{k_B}{e}\right)^2 \equiv \mathcal{L}_0 \tag{15}$$

Now we will consider the opposite limit when $\beta\mu \ll 1$. This case correspond to high temperatures or to low electron concentration. In this case we have the following approximations:

$$L_0 \cong \frac{gT_0}{2h}\left[1+\frac{\beta\mu}{2}\right] \tag{16}$$

$$L_1 \cong \frac{gT_0 \ln 2}{\beta h}\left[1-\frac{(\beta\mu)^2}{8\ln 2}\right] \tag{17}$$

and:

$$L_2 \cong \frac{gT_0\pi^2}{6h\beta^2}\left[1+\frac{(\beta\mu)^3}{2\pi^2}\right] \tag{18}$$

The Lorentz number becomes:

$$\mathcal{L} \cong \frac{\pi^2}{3}\left(\frac{k_B}{e}\right)^2\left\{1-\frac{12(\ln 2)^2}{\pi^2}+\beta\mu\left[\frac{12(\ln 2)^2}{\pi^2}-\frac{1}{2}\right]\right\} \tag{19}$$

After evaluating the numerical factors we get:

$$\mathcal{L} \cong 0.416\ (1+0.2019\ \beta\mu)\mathcal{L}_0 \cong 0.416\ \mathcal{L}_0 \tag{20}$$

Case 2: Electronic system with linear transmission $T(\varepsilon)=a\varepsilon$.
In this case, using eq. (4), the L_n terms will be:

$$L_0 = \frac{ga}{h\beta}\left\{\frac{\beta\mu}{2}+\ln\left[2\cosh\left(\frac{\beta\mu}{2}\right)\right]\right\} \tag{21}$$

with the approximations:

$$L_0 \cong \frac{ga\mu}{h} \tag{22}$$

for $\beta\mu \gg 1$, and:

$$L_0 \cong \frac{ga}{h\beta}\left(\ln 2+\frac{\beta\mu}{2}\right) \tag{23}$$

for $\beta\mu \ll 1$.

For L_1 we will obtain:

$$L_1 = \frac{2ag}{h\beta^2}\left\{\frac{\pi^2}{6}+\left(\frac{\beta\mu}{2}\right)^2+polylog\left(2,-e^{-\beta\mu}\right)-\frac{\beta\mu}{2}\ln\left[2\cosh\left(\frac{\beta\mu}{2}\right)\right]\right\} \tag{24}$$

In the case $\beta\mu \gg 1$:

$$L_1 \cong \frac{\pi^2 ga}{3\ h\beta^2} \tag{25}$$

and for $\beta\mu \ll 1$:

$$L_1 \cong \frac{\pi^2 ga}{6\ h\beta^2}\left(1+\frac{6\ln 2}{\pi^2}\ \beta\mu\right) \tag{26}$$

The last factor is:

$$L_2 = \frac{2ag\mu}{h\beta^2}\left\{\frac{\pi^2}{6} - \left(\frac{\beta\mu}{2}\right)^2 + \frac{\beta\mu}{2}\ln\left[2\cosh\left(\frac{\beta\mu}{2}\right)\right] - 2\,polylog\left(2, -e^{-\beta\mu}\right) - \frac{3}{\beta\mu}\,polylog(3, -e^{-\beta\mu})\right\} \quad (27)$$

In the low temperatures $\beta\mu \gg 1$, and:

$$L_2 \cong \frac{\pi^2 ga\mu}{3\,h\beta^2} \quad (28)$$

and in the opposite limit $\beta\mu \ll 1$:

$$L_2 \cong \frac{ag}{2\,h\beta^3}\left[9\zeta(3) + \frac{\pi^2\beta\mu}{3}\right] \quad (29)$$

where ζ(x) is the Riemann's zeta function. Using the results above the Lorentz number in the low temperatures limit $\beta\mu \gg 1$ becomes:

$$\mathcal{L} \cong \mathcal{L}_0\left[1 - \frac{\pi^2}{3\,(\beta\mu)^2}\right] \quad (30)$$

In the opposite limit $\beta\mu \ll 1$, and the Lorentz number is:

$$\mathcal{L} \cong \mathcal{L}_0\,\frac{3\,q}{\pi^2}\,(1 + r\,\beta\mu) \quad (31)$$

Where *q* and *r* are complicated numerical factors given by *q*=2.1721…, and *r*=0.05638… . The Lorentz number will be:

$$\mathcal{L} \cong 0.66\,\mathcal{L}_0(1 + 0.05638\,\beta\mu) \cong 0.66\,\mathcal{L}_0 \quad (32)$$

Case 3: Graphene systems (electrons and holes) with quadratic transmission $T(\varepsilon)=a\varepsilon^2$.

In the case of graphene the integral over energies in (4) is taken over the entire interval $(-\infty, +\infty)$ taking into account the holes contribution (from $-\infty$ to μ), and the electrons contribution (from μ to $+\infty$). In this way, the first factor L_0 will be:

$$L_0 = \frac{\pi^2 g_s g_v a}{3\,h\beta^2}\left[1 + \frac{3(\beta\mu)^2}{\pi^2}\right] \quad (33)$$

the second factor L_1:

$$L_1 = \frac{\pi^2 g_s g_v \beta a\mu}{24\,h}\left(\frac{2}{\beta}\right)^3 \quad (34)$$

and the third factor L_2:

$$L_2 = \frac{7\pi^4 g_s g_v a}{15\, h\beta^4}\left[1 + \frac{5(\beta\mu)^2}{7\pi^2}\right] \tag{35}$$

The calculated Lorentz number will be:

$$\mathcal{L} = \frac{21}{5}\, f\, \mathcal{L}_0 \tag{36}$$

where:

$$f = \frac{1 + 3\left(\frac{\beta\mu}{2}\right)^2\left[1 + \frac{5}{7}\left(\frac{\beta\mu}{\pi}\right)^2\right]}{\left[1 + 3\left(\frac{\beta\mu}{\pi}\right)^2\right]^2} \tag{37}$$

At the Dirac point (μ=0) the Lorentz ratio becomes:

$$\mathcal{L} = \frac{21}{5}\, \mathcal{L}_0 \equiv 4.2\, \mathcal{L}_0 \tag{38}$$

and decreases as one departs from the Dirac point. When $\beta\mu \gg 1$, the Lorentz ratio is:

$$\mathcal{L} = \mathcal{L}_0 \tag{39}$$

For highly doped graphene, with this form of transmission, the Lorentz number is similar to the classical result for the Fermi systems. Close to the neutrality point the result changes appreciably. It remains to analyze the consequence of changing of the Lorentz number on the efficiency of thermoelectric conversion, by determining the figure of merit *ZT*.

REFERENCES

1. A.Seebeck, *Pogg. Ann.* 6, 133, (1826)
2. J.C. Peltier, *Ann. chim. et. Phys.* 56, 371, (1834)
3. Lord. Kelvin, *Collected. Papers, Cambridge*. 1, 316, (1882)
4. F.J. Blatt, *"Solid. State. Physics. Advances. in. Reserch. and. Applications",* F. Seitz, D. Turnbull. eds., vol. 4, Acad. Press, NY, 199, (1957)
5. V. Pop, I. Chicinas, N. Jumate, *"Fizica. Materialelor. Metode. experimentale",* Presa Univ. Clujeana, (2001)
6. G. Wiedemann, R. Franz, *Ann. Physik.* 89, 497, (1853)
7. G. Benenti, G. Casati, K. Saito, R.S. Whitney, *Phys. Rep*. 694, 1, (2017)

8. B. Kubala, J. König, J.P. Pekola, *Phys. Rev. Lett*. 100, 066801, (2008)
9. E. Sivre, A. Anthore, F.D. Parmentier, A. Cavanna, U. Gennser, A. Ouerghi, Y. Jin, F. Pierre, *Nat. Phys.* 14, 145, (2018)
10. U. Sivan, Y. Imry, *Phys. Rev. B* 33, 551, (1986)
11. M.G. Vavilov, A.D. Stone, *Phys. Rev. B*72, 205107, (2005)
12. S.T. Rodriguez, I. Grosu, M. Crisan, I. Tifrea, *Physica. E96*, 1, (2018)
13. J.R. Isern-Lozano, J.S. Lim, I. Grosu, R. Lopez, M. Crisan, D. Sanchez, *Eur. Phys. J. Special. Topics*, 227, 1969, (2019)
14. M. Crisan, I. Grosu, I. Tifrea, *Physica. E*124, 114361, (2020)

STUDIA UBB PHYSICA, Vol. 66 (LXVI), 1-2, 2021, pp. 55-68
(RECOMMENDED CITATION)
doi:10.24193/subbphys.2021.06

COMBINED MÖSSBAUER SPECTROMETRY AND ATOM PROBE TOMOGRAPHY INVESTIGATION OF MECHANICALLY MILLED RARE EARTH / TRANSITION METAL POWDERS

JEAN-MARIE LE BRETON[1*], RODRIGUE LARDE[1], AMJAAD ABOU LATIF[1], NICOLAS MAAT[1], VIRGINIE NACHBAUR[1], OLIVIER ISNARD[2], DOMINIQUE GIVORD[2], IONEL CHICINAS[3], VIOREL POP[4]

ABSTRACT. The microstructure of mechanically milled $Nd_2Fe_{14}B$, $SmCo_5$/Fe and $SmCo_3Cu_2$/α-Fe alloys has been investigated by Mössbauer spectrometry and atom probe tomography. The structural changes that occur upon milling and subsequent annealing were characterised at a nanometer scale. Milling promotes intermixing of the elements and the formation of nanograins. In Nd-Fe-B powders, the $Nd_2Fe_{14}B$ phase is transformed into α-Fe and an amorphous Nd-Fe-B phase. In $SmCo_5$/Fe powders, Fe/Co intermixing occurs, leading to the formation of $Sm(Co,Fe)_5$ and α-Fe(Co) phases. In $SmCo_3Cu_2$/Fe powders, although Sm is partly oxidised, Fe/Co intermixing occurs as well, leading to the formation of α-Fe(Co) nanograins surrounded by $Sm(Co,Cu,Fe)_5$ intergranular regions. The combined Mössbauer and atom probe tomography investigation of rare earth / transition metal powders thus allows revealing the effect of mechanical milling and subsequent annealing on the nanostructure of the powders. These results are helpful for the understanding of the magnetic properties of the powders.

Keywords: *rare earths-transition metals powders, Mössbauer spectrometry, atom probe tomography*

[1] *Normandie University, UNIROUEN, INSA Rouen, CNRS, Groupe de Physique des Matériaux, 76000 Rouen, France*

[2] *Institut Néel, CNRS, Grenoble INP, Université Grenoble Alpes, 25 Avenue des Martyrs, 38000 Grenoble, France*

[3] *Materials Science and Engineering Department, Technical University of Cluj-Napoca, 103-105 Muncii Ave., 400641 Cluj-Napoca, Romania*

[4] *Faculty of Physics, Babes-Bolyai University Cluj-Napoca, Kogalniceanu str 1, 400084 Cluj-Napoca, Romania*

[*] *Corresponding author: jean-marie.lebreton@univ-rouen.fr*

1. INTRODUCTION

Up today, hard magnetic materials based on rare earth / transition metal phases have the best magnetic properties among the permanent magnets materials. With the aim to increase further the magnetic properties of these permanent magnet materials, it is possible to reduce the dimensions of the grains down to the nanometer scale. Such a grain size reduction can be achieved by mechanical milling and subsequent annealing.

Another way to improve the magnetic properties of rare earth / transition metal materials is to obtain nanocomposites consisting of an intimate mixture of two magnetic phases, one soft (Fe_3B, α-Fe…), and one hard ($Nd_2Fe_{14}B$, $SmCo_5$…). Such a nanostructure combines the high coercivity of the hard magnetic phase with the high magnetisation of the soft magnetic phase, the two phases being coupled by exchange [1,2].

These so-called "spring magnets" can lead to energy products $(BH)_{max}$ higher than those achieved in the existing sintered magnets [3]. However, the role of the microstructure in the spring mechanism is not well understood [1,3-6]. Several studies were performed in view of obtaining spring magnet-type magnetic materials by mechanical alloying (MA) or mechanical milling (MM) [7–14]. Since the discovery of intergrain exchange coupling, MA has become a widely used preparation technique to obtain nanocrystalline structures of magnetic materials.

With the aim at contributing to the understanding of intergrain exchange-coupling, a structural characterization at a nanometer scale of hard/soft magnetic powders is required. From this point of view, combined Mössbauer spectrometry and atom probe tomography investigations is useful.

Mössbauer spectrometry is a very useful tool for investigating structural transformations occurring during mechanical milling of rare earth / transition metal powders. Because this technique is sensitive to the environment of Fe atoms, it allows following accurately the evolution of iron containing phases upon milling and subsequent annealing. In each case, the Mössbauer investigation was completed by atom probe tomography analysis. Atom probe tomography (APT) is a high resolution analytical microscope which provides a 3D mapping at the atomic scale of the spatial distribution of atoms in the analysed specimen [15-17]. It is particularly well suited to identify small clusters and analyse chemical heterogeneities.

Here we present the results of combined Mössbauer spectrometry and atom probe tomography investigations of mechanically milled $Nd_2Fe_{14}B$/Fe, $SmCo_5$/Fe and $SmCo_3Cu_2$/Fe powders. Some results have been previously reported [18-23].

2. EXPERIMENTAL

Ingots with $Nd_2Fe_{14}B$, $SmCo_5$ and $SmCo_3Cu_2$ nominal compositions were prepared by induction melting under argon atmosphere. The purity of the starting elements was 99.9%.

The $Nd_2Fe_{14}B$ ingot was crushed and the resulting powder was sieved through a 500 μm sieve. The sieved powder was dry-milled under Ar atmosphere in a planetary mill for 1, 2, 4, 8 and 12h. The milling vials (with a volume of 80 ml) and balls (Ø 10 mm in diameter) were made of 440 C hardened steel. The ratio between the rotation speed of the disc and the relative rotation speed of the vials was Ω/ω = 333/–900 rpm with a ball-to-powder weight ratio of 10:1.

The $SmCo_5$ ingot was crushed into small pieces and it was subsequently mechanically milled for two hours in a high energy planetary mill under argon atmosphere. The obtained $SmCo_5$ powder was mixed with an Fe powder (grain size below 40 μm) in a ratio of 80 wt%($SmCo_5$)/ 20 wt%(Fe), and the mixture was mechanically milled for an additional time of 8h. The mechanically milled powder was placed in a sealed evacuated silica tube and annealed at temperatures up to 650°C for 0.5h to remove the internal strains and defects introduced during milling.

The $SmCo_3Cu_2$ ingot was crushed into small pieces and subsequently mechanically milled for 2 h under argon atmosphere. The $SmCo_3Cu_2$ powder thus obtained was mixed with an iron powder (grain size below 40 μm) in a ratio of 70 wt% ($SmCo_3Cu_2$)/30 wt% (Fe). The mixture was mechanically milled under argon atmosphere using the high-energy planetary mill. Several milling times were used ranging from 1.5 to 9 h. In order to investigate the influence of the annealing on the structural evolution of the $SmCo_3Cu_2$/Fe powder, samples of milled powder were sealed inside evacuated silica tubes for further heat treatments. These treatments were performed at temperatures ranging from 400 to 450°C for times ranging from 1 min to 2 h.

^{57}Fe Mössbauer spectrometry experiments were performed at room temperature in transmission geometry, using a ^{57}Co source in a rhodium matrix. The Mössbauer spectra were fitted according to a least squares method [24]. The isomer shift (relative to metallic α-Fe at room temperature) and hyperfine field are denoted δ and B respectively.

The APT experiments were performed with a Laser Assisted Wide Angle Tomographic Atom Probe from CAMECA. For sample preparation, a single particle with a diameter in the range 1-50 μm was mounted on a stainless steel fine tip needle with conductive epoxy glue, using an ex-situ micro-manipulator. The particle

was tip-shaped using a focused Ga ion beam (30 kV) [25]. To reduce Ga implantation and avoid structural damages, the final step of milling was performed at low acceleration voltage (2 kV). The tips were analyzed at 80 K in an ultrahigh vacuum chamber at a pressure of 10^{-9} mbar. The femtosecond laser pulse system used was an amplified ytterbium-doped laser (Amplitude System s-pulse) with a 350 fs pulse length and a 332 nm wavelength.

3. RESULTS

3.1. $Nd_2Fe_{14}B$ powder

The room temperature Mössbauer spectra of the $Nd_2Fe_{14}B$ powder before milling and milled for 2 and 12 hours are shown in figure 1. One can see a clear evolution of the Mössbauer spectrum with milling time, indicating important structural changes induced by mechanical milling.

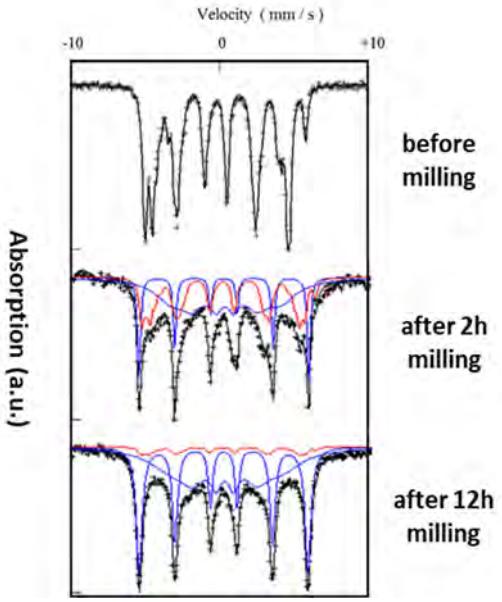

Figure 1 *– Room temperature Mössbauer spectra of the Nd-Fe-B powder before milling, and after milling for 2h and 12h. In the spectra of the milled powders, the red contribution corresponds to the $Nd_2Fe_{14}B$ phase, the blue sextet contribution corresponds to the α-Fe phase and the blue large contribution corresponds to an amorphous contribution.*

The spectrum of the powder before milling was fitted with the contribution of the $Nd_2Fe_{14}B$ phase. The spectra of the milled powders were fitted, according to a fitting procedure previously described [26], with three contributions: the contribution of the $Nd_2Fe_{14}B$ phase, the contribution of the α-Fe phase and, a contribution typical for an amorphous phase. As the milling time increases, the relative intensity of the $Nd_2Fe_{14}B$ phase contribution decreases, as those of both α-Fe and amorphous phases increase. This clearly shows the disappearance of the $Nd_2Fe_{14}B$ phase induced by milling and its transformation into α-Fe and amorphous phases.

A 3D reconstruction of a volume of the powder milled for 2 hours derived from APT analysis is shown in figure 2a. The corresponding Nd, Fe and B concentration profiles in the analyzed volume are also shown. One can clearly see the presence of three regions with different compositions:

- a region constituted of a mixture of iron, neodymium and boron (left part of the figure), corresponding to the $Nd_2Fe_{14}B$ phase also detected in the Mössbauer spectrum,

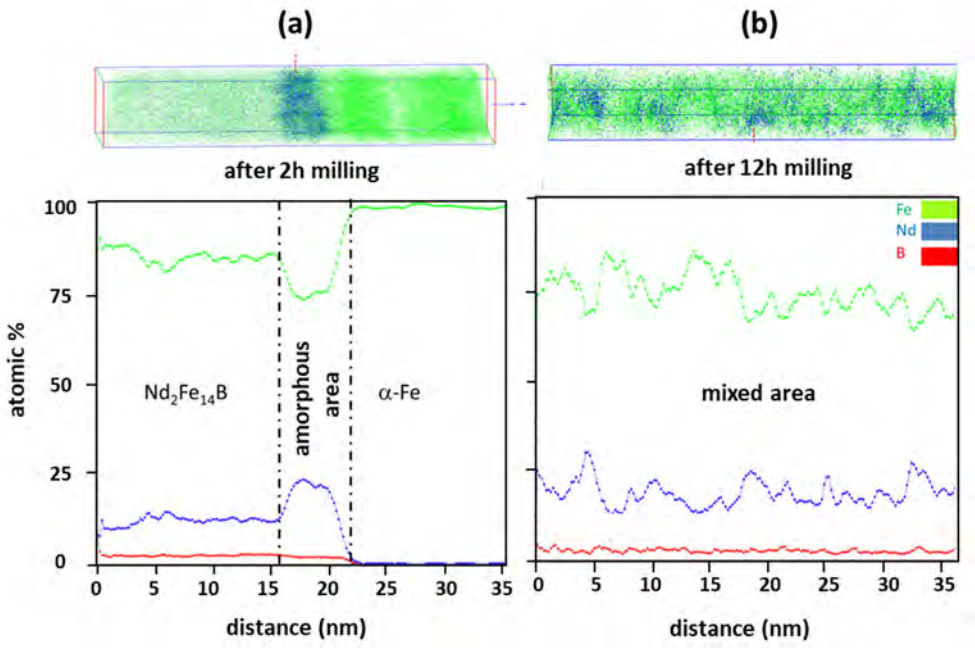

Figure 2 *–3D reconstruction obtained by APT of an analysed volume of the Nd-Fe-B powder milled for 2h (a) and 12h (b) and corresponding concentration profiles.*

- a neodymium enriched Nd-Fe-B region (middle part of the picture), attributed to the amorphous contribution fitted in the Mössbauer spectrum,
- a region almost entirely constituted of Fe atoms (right part of the figure), corresponding to the α-Fe Mössbauer contribution.

A 3D reconstruction of a volume of the powder milled for 12 hours derived from APT analysis is shown in figure 2b. The corresponding Nd, Fe and B concentration profiles in the analyzed volume are also shown. A so-called mixed area is observed, revealed by variations of the Fe and Nd composition at the nanometer scale. This indicates that the powder milled for 12 hours contains nanosized regions that are not pure and present diffuse interfaces. Increasing the milling time thus promotes the intermixing of Nd, Fe and B elements leading, in agreement with the Mössbauer analysis, to the almost complete disappearance of the $Nd_2Fe_{14}B$ phase and to the formation of Nd-Fe-B amorphous regions and α-Fe regions, mixed at a nanometer scale.

3.2. $SmCo_5$/Fe powder

The room temperature Mössbauer spectra of the $SmCo_5$/Fe powder before milling and milled for 2 and 8 hours are shown in figure 3. An evolution of the Mössbauer spectrum with milling time is observed, related to structural changes induced by mechanical milling.

The spectrum of the powder before milling was fitted with the contribution of the α-Fe phase, in relation with the fact than that before milling, all the iron atoms are present in the α-Fe phase. The spectra of the milled powders were fitted according to a fitting procedure previously described [21], with two contributions. These contributions are:

- a magnetic contribution with a hyperfine field between 33 and 35 T typical of an Fe-Co alloy, corresponding to a Fe-Co phase,
- a magnetic contribution with a mean hyperfine field typical of a rare-earth / transition metal alloy, corresponding to a Sm-Co-Fe phase.

As the milling time increases, the relative intensity of the Sm-Co-Fe phase contribution increases, as that of Fe-Co phase decreases. This shows that milling induces an intermixing of Fe and Co atoms, leading to the introduction of Co atoms in the α-Fe phase and Fe atoms in the $SmCo_5$ phase. These two phases are thus denoted α-Fe(Co) and $Sm(Co,Fe)_5$ respectively.

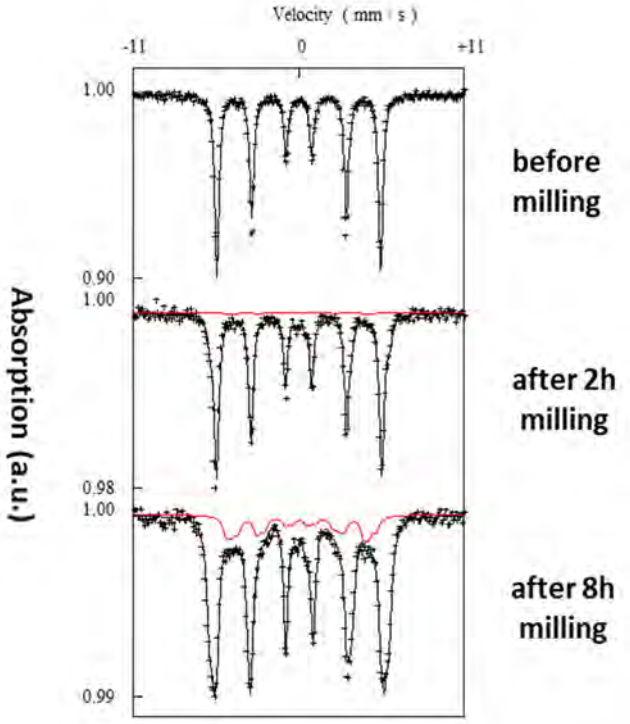

Figure 3 *– Room temperature Mössbauer spectra of the $SmCo_5$/Fe powder before milling, and after milling for 2h and 12h. In the spectra of the milled powders, the red contribution corresponds to the $Sm(Co,Fe)_5$ phase.*

The room temperature Mössbauer spectra of the $SmCo_5$/Fe powder milled for 8 hours and annealed for 0.5 hour at 500 and 550°C are shown in figure 4. As compared with the spectrum of the as-milled powder, one can see that the contribution of the Sm-Co-Fe phase increases with the annealing temperature, in agreement with an increase of the Fe/Co intermixing.

A 3D reconstruction of a volume of the powder milled for 8 hours derived from APT analysis, is shown in figure 5. The figure shows the spatial distribution of the Sm, Co, and Fe atoms in the analysed volume. A slice taken from the 3D reconstruction is shown in the figure, presenting the individual spatial distribution of each type of atoms. The Sm atoms are only detected in Sm-Co-rich regions. The regions where Sm is not present correspond to the Fe rich regions in the Fe map, being of a few nanometers in size. The Fe atoms are also present in the Sm-rich regions. The Co

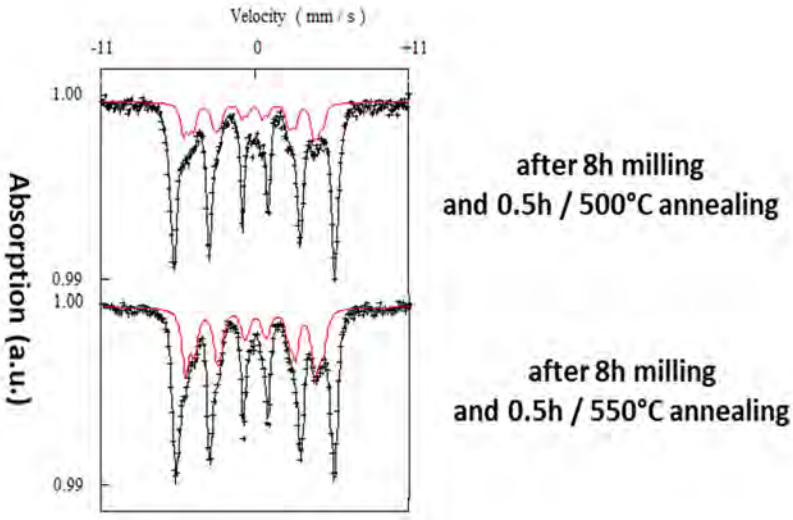

Figure 4 *– Room temperature Mössbauer spectra of the $SmCo_5$/Fe powder after milling and annealing for 0.5h at 500 and 550°C. The red contribution corresponds to the $Sm(Co,Fe)_5$ phase.*

atoms are detected in both the Sm-rich and the Fe-rich regions, their concentration being higher in the Sm-rich regions. The mean composition of the Sm-rich regions is 20±2% Sm, 70±2% Co and 10±2% Fe, being consistent with a $Sm(Co,Fe)_5$ phase. The mean composition of the Fe-rich regions is 75±2% Fe, and 25±2% Co.

These results are fully consistent with the Mössbauer analysis and confirm that mechanical milling leads to Fe/Co intermixing, leading to the presence in the as-milled powders of two phases: a $Sm(Fe,Co)_5$ phase and a $Fe_{75}Co_{25}$ phase. These two phases are present as grains with a nanometer size.

A 3D reconstruction of the $SmCo_5$/Fe powder milled for 8h and annealed for 0.5h at 550°C is shown in figure 6. The nanoscale morphology of the annealed powder is comparable to that of the as-milled powder, as the powder contains nanosized Fe(Co) clusters embedded in the $Sm(Co,Fe)_5$ phase. The mean Fe content in the $Sm(Co,Fe)_5$ phase is slightly higher than the value measured in the as-milled sample, being 15±2%. The Co content in the Fe(Co) is statistically higher after annealing amounting to 45±2% Co. These variations of the atomic concentrations upon annealing confirm that the Fe/Co interdiffusion is thermally activated. The increase of the Fe content in the Sm-rich regions and the increase of the Co content in the Fe-rich regions upon annealing are consistent with the results of the Mössbauer analysis.

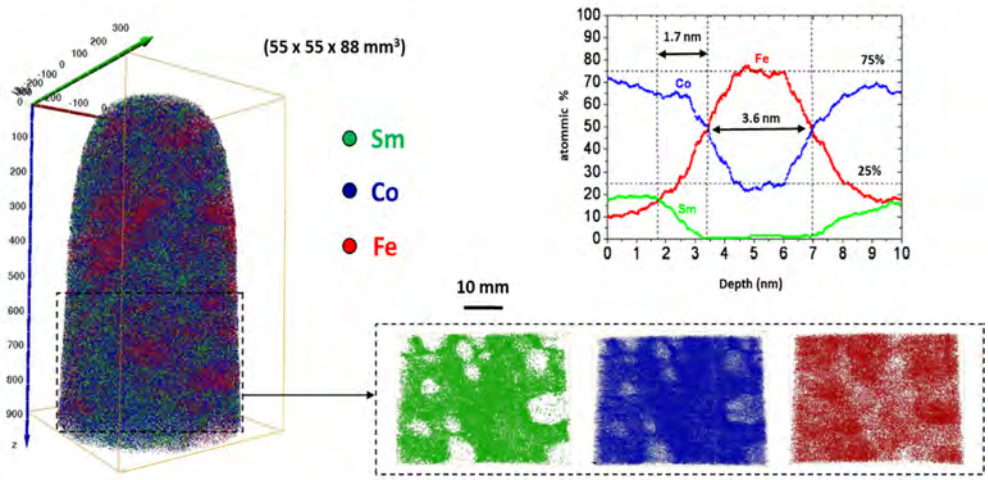

Figure 5 *– 3D reconstruction obtained by APT of an analysed volume in the $SmCo_5$/Fe powder milled for 8h, and concentration profile through a Fe-rich region. The distribution of Sm, Co and Fe atoms in a 30 nm thick slice taken from the analysed volume is shown.*

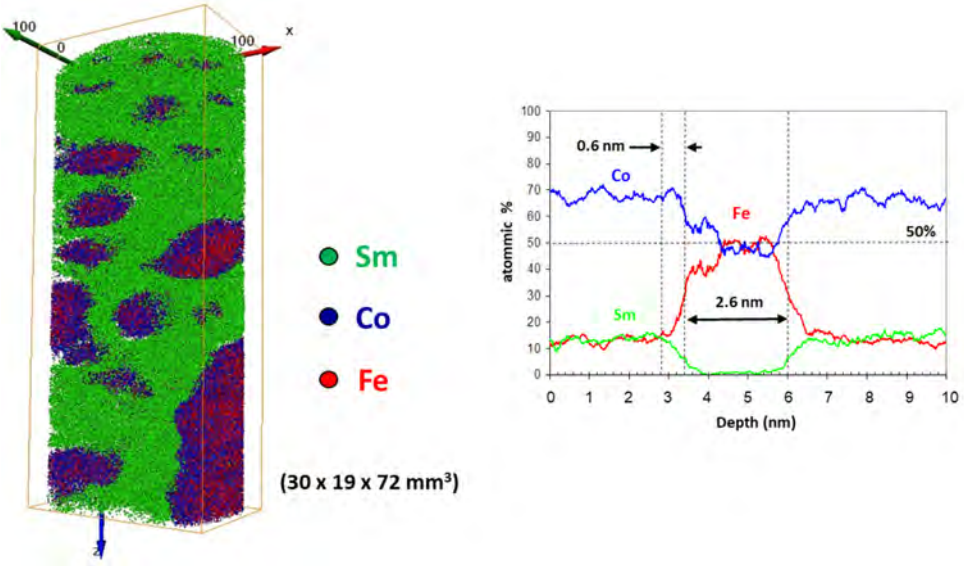

Figure 6 *– 3D reconstruction obtained by APT of an analysed volume of the $SmCo_5$/Fe powder milled for 8h and subsequently annealed for 0.5h at 550°C and concentration profile through a Fe-rich region.*

3.3. $SmCo_3Cu_2$/Fe powder

The room temperature Mössbauer spectra of the $SmCo_3Cu_2$/Fe powder before milling and milled for 9 hours are shown in figure 7. The room temperature spectrum of the powder milled for 9 hours and subsequently annealed for 0.5 hours at 450°C is shown in the same figure.

The spectrum of the powder before milling was fitted with the contribution of the α-Fe phase, in relation with the fact than that before milling, all the iron atoms are present in the α-Fe phase. The spectra of the milled powders were fitted with two contributions:

- a magnetic contribution with a hyperfine field between 33 and 35 T typical of an Fe-Co alloy, corresponding to a Fe-Co phase,
- a magnetic contribution with a mean hyperfine field typical of a rare-earth / transition metal alloy, corresponding to a Sm-Co-Cu-Fe phase.

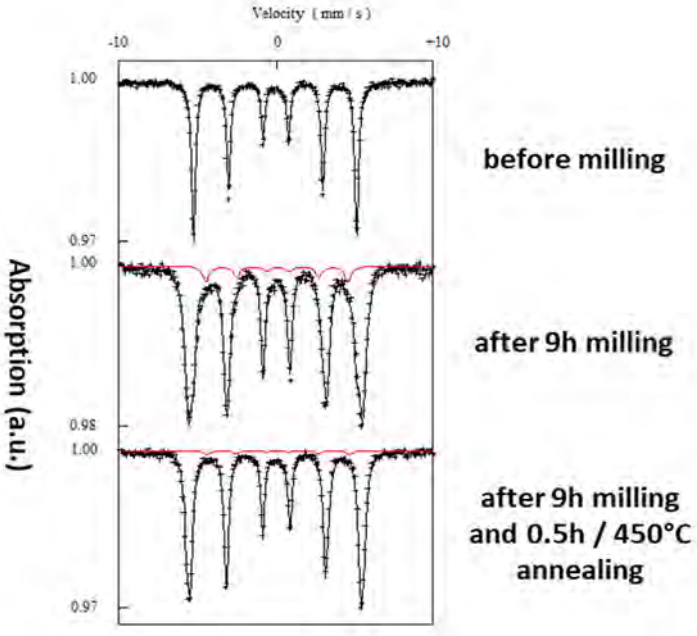

Figure 7 *– Room temperature Mössbauer spectra of the $SmCo_3Cu_2$/Fe powder before milling, after milling for 9h and after milling for 9h and subsequent annealing for 0.5h at 450°C. The red contribution corresponds to Sm(Co,Fe,Cu) regions.*

After 9 hours milling, the relative intensity of the Sm-Co-Cu-Fe phase contribution is lower than that of the Sm-Co-Fe phase in the $SmCo_5$/Fe powder after 8 hours milling. This suggests that the Fe/Co intermixing upon milling is lower in the $SmCo_3Cu_2$/Fe powder than in the $SmCo_5$/Fe powder.

After annealing, the Mössbauer spectrum of the powder milled for 9 hours is mainly composed of the contribution of the Fe-Co phase, as the relative intensity of the Sm-Co-Cu-Fe phase is very small, being lower than in the as-milled powder. This indicates that only a few Fe atoms are present in the Sm-rich phase after annealing, suggesting that the Fe/Co intermixing is not as important as in the $SmCo_3Cu_2$/Fe powders. As compared with the behaviour of the $SmCo_5$/Fe powder upon annealing, the behaviour of the $SmCo_3Cu_2$/Fe powder upon milling and subsequent annealing could be related to the presence of Cu atoms.

3D reconstructions of a volume of the powder milled for 9 hours, before and after annealing for 0.5 hour at 450°C, derived from APT analysis, are shown in figure 8. Slices taken from the 3D reconstruction are shown in the figure, presenting the individual spatial distributions of Sm, Co, Cu and Fe atoms.

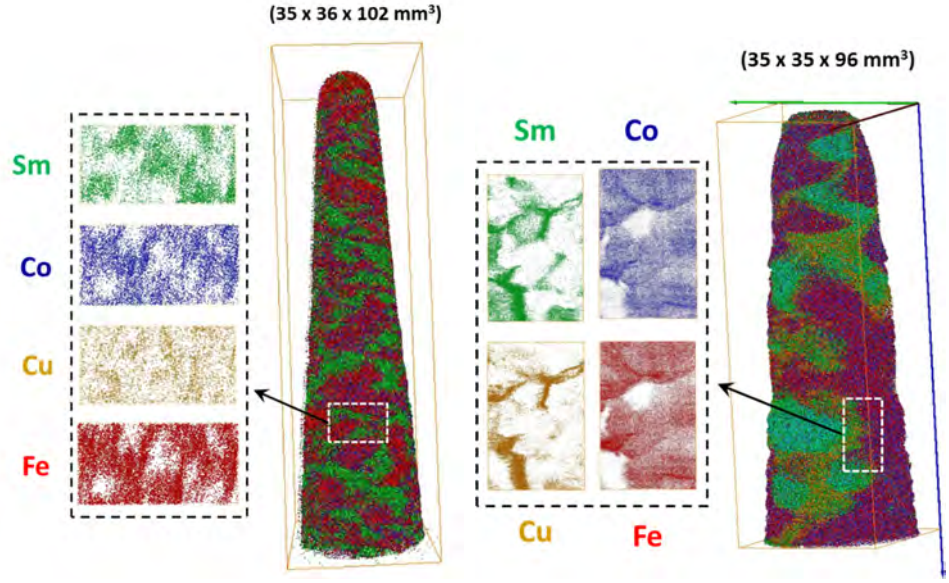

Figure 8 *– 3D reconstruction obtained by APT of an analysed volume in the $SmCo_3Cu_2$/Fe powder milled for 9h before (left) and after (right) annealing for 0.5h at 450°C. The distributions of Sm, Co, Cu and Fe atoms in a 5 nm thick slice taken from the analysed volume are shown.*

In the as-milled powder, one can observed the presence of Sm-rich regions, containing a few Co and Fe atoms, and Sm-poor regions, containing a high amount of Co and Fe atoms. Cu atoms are present in the whole analysed volume, with a concentration that is more important in Sm-rich regions than in Sm-poor regions.

In the annealed powder, three different regions are observed: Sm-rich regions with almost no Co, Fe or Cu atoms, Sm-poor regions with a high amount of Co and Fe atoms, and Sm-Co-Cu-Fe regions that seem to correspond to intergranular regions. The Sm-rich regions could correspond to Sm oxides.

These results are in agreement with Mössbauer analysis, showing that milling induces Fe/Co intermixing, leading to the formation of a Fe-Co phase and Sm-Co-Cu-Fe regions. However, the proportion of the Sm-Co-Cu-Fe phase is low, as Sm-rich regions almost pure in Sm are observed that could correspond to Sm oxides. Annealing promotes the formation of Fe-Co nanograins surrounded by intergranular Sm-Co-Cu-Fe regions.

4. CONCLUSION

The combined Mössbauer and APT investigation of rare earth / transition metal powders allows revealing the effect of mechanical milling and subsequent annealing on the nanostructure of the powders.

Milling $Nd_2Fe_{14}B$ powder leads to the formation of nanosized regions that are not pure and present diffuse interfaces. The intermixing of Nd, Fe and B elements is promoted. Nd-Fe-B amorphous regions and α-Fe regions, mixed at a nanometer scale, are formed.

Milling $SmCo_5$/Fe powders induces Fe/Co intermixing, and leads to the formation of $Sm(Fe,Co)_5$ and α-Fe(Co) phases that are present in grains with a nanometer size. Upon annealing, the Fe/Co interdiffusion is thermally activated, inducing an increase of both the Fe content in the $Sm(Fe,Co)_5$ phase and the Co content in the α-Fe(Co) phases.

Milling $SmCo_3Cu_2$/Fe powders induces Fe/Co intermixing, and leads to the formation of a Fe-Co phase, and Sm-Co-Cu-Fe regions. However, the proportion of the Sm-Co-Cu-Fe phase is very low, as Sm-rich regions almost pure in Sm are present as well, that could correspond to Sm oxides. Annealing promotes the formation of Fe-Co nanograins surrounded by intergranular Sm-Co-Cu-Fe regions.

These results show that the combined Mössbauer spectrometry and atom probe tomography investigation of mechanically milled rare earth / transition metal powders allows obtaining both structural and chemical information at a nanometer scale that is thus useful for the understanding of magnetic interactions between nanograins.

REFERENCES

[1] E.E. Fullerton, J.S. Jiang, M. Grimsditch, C.H. Sowers, S.D. Bader, *Physical Review B* 58 (1998) 12193
[2] E.E. Fullerton, J.S. Jiang, S.D. Bader, *Journal of Magnetism and Magnetic Materials* 200 (1999) 392
[3] E.F. Kneller, R. Hawig, *IEEE Transaction on Magnetics* 27 (1991) 3588
[4] R. Skomski, *Journal of Applied Physics* 76 (1994) 7059
[5] R. Skomski, *Journal of Physics Condensed Matter* 15 (2003) R841
[6] R. Skomski, J.M.D. Coey, *Permanent Magnetism*, Institute of Physics Publishing, Bristol
[7] J. Roskilde, J. Petzold, *Journal of Magnetism and Magnetic Materials* 242–245 (2002) 84
[8] P.A.P. Wendhausen, B. Gebel, D. Eckert, K.H. Muller, *Journal of Applied Physics* 75 (1994) 6019
[9] M. Venkatesan, C. Jiang, J.M.D. Coey, *Journal of Magnetism and Magnetic Materials* 242-245 (2002) 1350
[10] K. O'Donnell, J.M.D. Coey, *Journal of Applied Physics* 81 (1997) 6311
[11] L. Wei, W. Qun, X.K. Sun, Z. Xin-Guo, Z. Tong, Z. Zhi-Dong, Y.C. Chuang, *Journal of Magnetism and Magnetic Materials* 131 (1994) 413
[12] J.X. Zhang, L. Bessais, C. Djega-Mariadassou, E. Leroy, A. Percheron-Guegan, Y. Champion, *Applied Physics Letters* 80 (2002) 1960
[13] D.L. Leslie-Pelecky, R.L. Schalek, *Physical Review B* 59 (1999) 457
[14] V. Neu, L. Schultz, *Journal of Applied Physics* 90 (2001) 1540
[15] A. Cerezo, P.H. Clifton, A. Gomberg, G.D.W. Smith, *Ultramicroscopy* 107 (2007) 720–725.
[16] D. Blavette, B. Deconihout, A. Bostel, J.-M. Sarrau, M. Bouet, A. Menand, *Review of Scientific Instruments* 64 (1993) 2911–2919
[17] M.K. Miller, R.G. Forbes, *Materials Characterization* 60 (2009) 461–469
[18] N. Maât, R. Lardé, V. Nachbaur, J.-M. Le Breton, O. Isnard, V. Pop, I. Chicinas, *Journal of Applied Physics* 124 (2018) 223905
[19] R. Lardé, J.-M. Le Breton, A. Maître, D. Ledue, O. Isnard, V. Pop, I. Chicinas, *Journal of Physical Chemistry C* 117 (2013) 7801-7810
[20] V. Pop, E. Dorolti, C. Vaju, E. Gautron, O. Isnard, J.-M. Le Breton, I. Chicinas, *Romanian Journal of Physics* 55 (2010) 127-136

[21] J.-M. Le Breton, R. Lardé, H. Chiron, V. Pop, D. Givord, O. Isnard, I. Chicinas, *Journal of Physics D: Applied Physics* 43 (2010) 085001
[22] V. Pop, O. Isnard, D. Givord, J.-M. Le Breton, I. Chicinas, *Journal of Optoelectronics and Advanced Materials* 10 (2008) 1872-1876
[23] V. Pop, O. Isnard, I. Chicinas, D. Givord, J.-M. Le Breton, *Journal of Optoelectronics and Advanced Materials* 8 (2006) 494-500
[24] J. Teillet, F. Varret (1983) unpublished MOSFIT program
[25] K. Thompson, D. Lawrence, D.J. Larson, J.D. Olson, T.F. Kelly, B. Gorman, *Ultramicroscopy* 107 (2007) 131–139
[26] G. Khélifati, J.-M. Le Breton, L. Aymard, J. Teillet, *Journal of Magnetism and Magnetic Materials* 218 (2000) 42–48

STUDIA UBB PHYSICA, Vol. 66 (LXVI), 1-2, 2021, pp. 69-78
(RECOMMENDED CITATION)
doi:10.24193/subbphys.2021.07

NEAR ROOM-TEMPERATURE TEMPERATURE MAGNETOCALORIC EFFECT IN $Pr_{0.63-x}Ho_xSr_{0.37}MnO_3$ MANGANITES

ALEXANDRA LUDOȘAN[1], I.G. DEAC[1*]

ABSTRACT. Near room-temperature magnetic and magnetocaloric properties of the compounds $Pr_{0.63-x}Ho_xSr_{0.37}MnO_3$ (x=0, 0.05) were investigated. The parent compound $Pr_{0.63}Sr_{0.37}MnO_3$ has a large magnetocaloric effect around its Curie temperatures of about 300 K. Partially replacing of Pr^{3+} ions with Ho^{3+} ions in $Pr_{0.63}Sr_{0.37}MnO_3$ gives rise to disorder which leads to the decrease of the Curie temperature without a significant reduction of the magnetocaloric effect. The samples were prepared by solid state reaction and were found to be single phase by x-ray diffraction. The magnetic measurements reveal paramagnetic to ferromagnetic second order phase transitions. For the sample with x = 0, the magnetic entropy change $|\Delta S_M|$ was in the range from 1.91 J/kg⋅K (RCP = 42 J/kg) forμ_0 ΔH = 1 T to 4.86 J/kg⋅K (*RCP* = 184 J/kg) for μ_0 ΔH = 4 T. For the sample with x = 0.05, the magnetic entropy change $|\Delta S_M|$ was in the range from 1.61 J/kg⋅K (*RCP* = 57.9 J/kg) forμ_0 ΔH = 1 T to 4.38 J/kg⋅K (*RCP* = 236 J/kg) for μ_0 ΔH = 4 T and T_c = 216 K. These values recommend these materials to be potential candidates to be used in near room-temperature refrigeration applications.

Keywords: *Perovskite manganites, phase transition, magnetocaloric effect.*

INTRODUCTION

Magnetocaloric effect (MCE) is a magneto-thermodynamic phenomenon which consists in the (irreversible) change of the temperature of a material when a magnetic field is applied. When cooling result in a cycle which consist in magnetization and demagnetization of the magnetocaloric material, this effect can be used as an alternative of the conventional vapor compression domestic refrigerators [1]. Magnetic

[1] *Babeş-Bolyai University, Faculty of Physics, 1 Kogălniceanu str., 400084 Cluj-Napoca, Romania*
* *Corresponding author: Iosif.deac@phys.ubbcluj.ro*

cooling is seen as an alternative for the conventional vapor compressing domestic refrigerators which usually work 20 -30 ^{0}C below room temperature. Gadolinium was found to show the largest magnetocaloric effect in the range from 270 to 310 K with a relative cooling power (RCP) of the order of 240 J/kg but the cost of this material is prohibitive of about 3000 euro/kg [2]. In the last decade a great deal of interest was devoted to find such materials with large MCE and reasonable costs [2]. Large magnetic entropy changes were also found in the perovskite mixed valence manganese oxides or in $Ln_{1-x}A_xMnO_3$ manganites (where Ln is a lanthanide and A is a divalent alkali) [3]. Some of these manganese oxides show large $|\Delta SM (T;\mu_0 H)|$ values comparable to those of the intermetallic compounds (i.e., $|\Delta SM (T;\mu_0 H)| \sim 4–6$ J kg^{-1}K^{-1} when $\mu_0 \Delta H = 5$ T) [4].

Here we propose such a magnetocaloric material, the $Pr_{0.63-x}Ho_xSr_{0.37}MnO_3$ perovskite manganite where x =0; 0.01. The parent compound is ferromagnetic below Curie temperature which is closed to 300 K and has a large MCE around this T_C. The partially substitution of Ho^{3+}ions (atomic radius 1.75 Å) for Pr^{3+} ions (atomic radius 1.18 Å) generates structural disorder which result in the decrease of Curie temperature to be in the range of the conventional domestic refrigeration.

In this paper we analyze in detail the magnetic and magnetocaloric properties of the $Pr_{0.63-x}Ho_xSr_{0.37}MnO_3$ perovskite manganites which are promising for application in magnetic cooling.

EXPERIMENTAL

The samples with nominal compositions $Pr_{0.63-x}Ho_xSr_{0.37}MnO_3$ with x = 0; 0.05 were prepared by standard solid-state reaction from high purity amounts of Pr_6O_{11}, $SrCO_3$, Mn_2O_3 and Ho_2O_3. The powders were mixed and calcinated at 1000^0 C (24 h), then they were pressed in into pellets and sintered at 1300^{0}C (30 h). The samples were checked by x-ray powder diffraction at room temperature by using a Brucker Advance D8 AXS diffractometer with CuKα radiation. A commercial cryogen-free VSM magnetometer (Cryogenic Ltd.) was used for magnetic measurements in the temperature range from 100 to 500 K and in applied magnetic fields from 0 to 4 T.

The magnetocaloric effect was estimated, calculating the magnetic entropy change $\Delta S_M (T,\mu_0 H)$ when the applied magnetic field $\mu_0 H_0$ is turn off to zero. The isothermal $M(\mu_0 H)$ curves were measured at a temperature interval of 5 K around the magnetic transition. In the case of second order magnetic phase transitions, the magnetic entropy change is given by [1]:

$$\Delta S_M(T,\mu_0 H_0) = \frac{1}{\Delta T}\int_0^{\mu_0 H_0}[M(T+\Delta T,\mu_0 H) - M(T,\mu_0 H)]d(\mu_0 H) \quad (1)$$

The relative cooling power (RCP) measures the heat transfer between warm and cold sources and can be calculated with the formula:

$$RCP = \Delta S_M(\max) \times \delta T_{FWHM} \quad (2)$$

$\Delta S_M(\max)$ is the peak value of ΔS_M (T,$\mu_0 H$) and δT_{FWHM} is the full width at half maximum (FWHM) of ΔS_M (T,$\mu_0 H$) vs. T curve for a given applied field. A good magnetocaloric material, needs both a large value of ΔS_M as well as a broad $\Delta S_M(T)$ curve.

RESULTS AND DISCUSSION

The x-ray diffraction patterns indicated that the samples are perovskite and they are single phases as shown in Fig. 1. The samples have orthorhombic *Pbnm* type structure, with the lattice constants a = 5.429 Å; b = 7.667 Å; c = 5.470 Å, for x = 0 and a = 5.432 Å; b = 7.673 Å; c = 5.476 Å, for x = 0.05.

In Figs. 2 and 3 are shown the temperature dependences of magnetization for the two samples taken in 0.05 T. The Curie temperatures are estimated as the point where the derivatives of the $M(T)$ curves dM/dT have a minimum, as can be seen in the inset. For the sample with x = 0 we have T_C = 298 K while for x = 0.05 the T_C = 215 K.

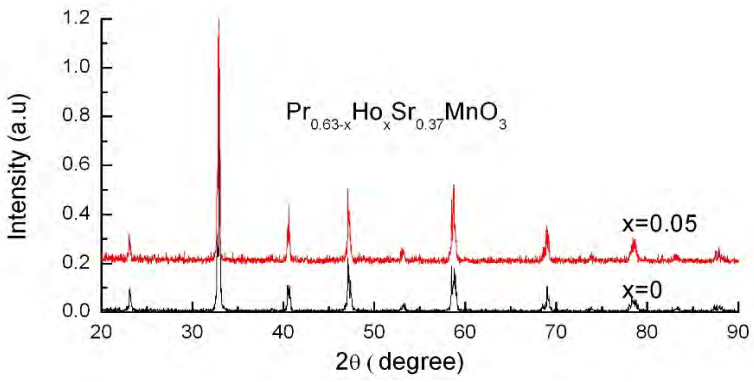

Fig. 1. X-ray diffraction patterns of the $Pr_{0.63-x}Ho_xSr_{0.37}MnO_3$ samples with x = 0; and x = 0.05.

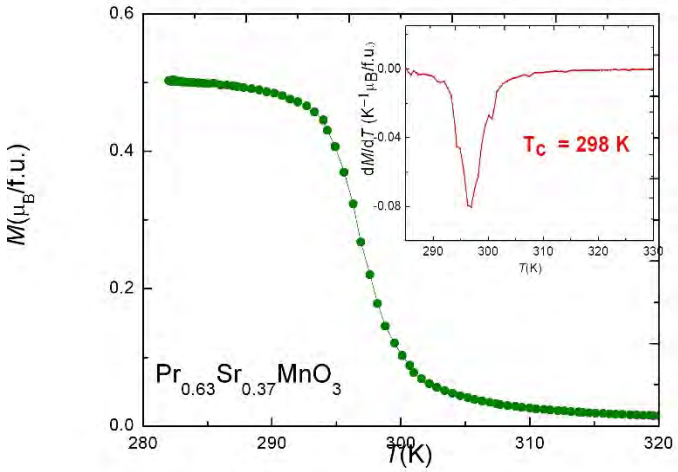

Fig. 2. *M(T)* for $Pr_{0.63}Sr_{0.37}MnO_3$ sample measured in 0.05 T. Inset: d*M*/d*T* vs. *T.*

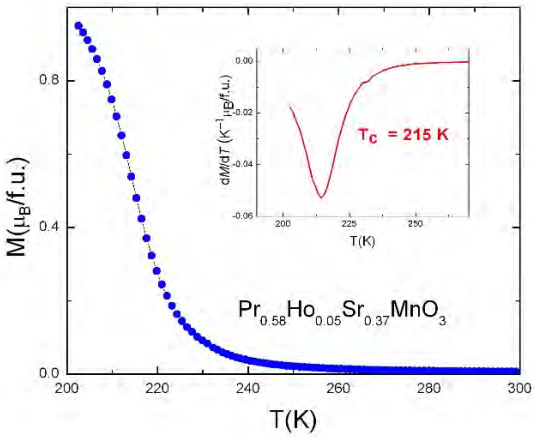

Fig. 3. *M(T)* for $Pr_{0.58}Ho_{0.05}Sr_{0.37}MnO_3$ sample measured in 0.05 T. Inset: d*M*/d*T* vs. *T.*

The magnetic field dependence on magnetization $M(\mu_0 H)$ for the two samples are displayed in Figs. 4 and 5.

As can be seen in Figs. 4 and 5, at low temperatures and in high applied magnetic fields the magnetizations tend to saturate [5], but still keeping a small linear increase. This behavior is the consequence of the presence of Pr^{3+} ions in a distorted crystal field [6].

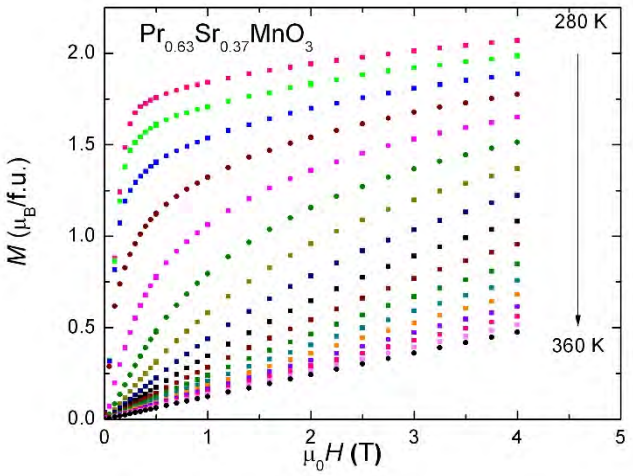

Fig. 4. *M(μ₀H)* for $Pr_{0.63}Sr_{0.37}MnO_3$ sample in the temperature range 280 – 360 K, taken at 5 K interval, from 1 to 4 T

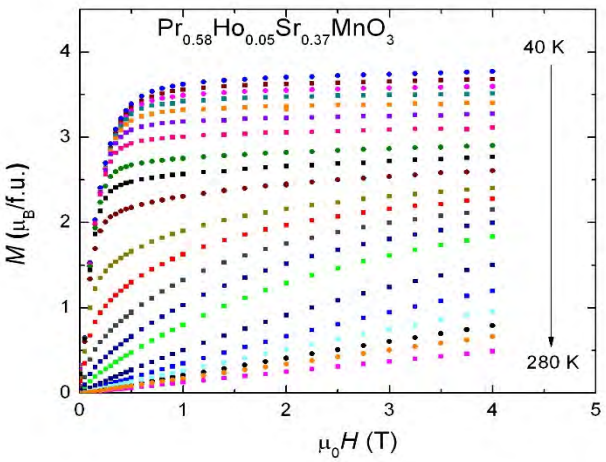

Fig. 5. *M(μ₀H)* for $Pr_{0.58}Ho_{0.05}Sr_{0.37}MnO_3$ sample in the temperature range 40 – 300 K taken at 5 K interval, from 1 to 4 T.

The magnetization dependences on temperature (Figs. 2 and 3) and on applied magnetic field (Figs. 4 and 5), indicate ferromagnetic behavior for the two samples, below the Curie temperatures, with small paramagnetic contributions from Pr^{3+} ions. The magnetocaloric effect can be estimated in terms of magnetic entropy change ΔS_M (T,$\mu_0 H$) and of relative cooling power *RCP*.

The approximation given by formula (1) is valid for a second order magnetic phase transition. The order of a magnetic phase transition can be established analyzing the so-called Arrot plot (M^2 vs $\mu_0 H/M$ around the transition) [7] using the Banerjee criterion [8]. If the slopes of these curves are positive the transition is of second order. If negative slope curves are present the transition is first order.

The Arrot plots for our samples are shown in Figs. 6 and 7.

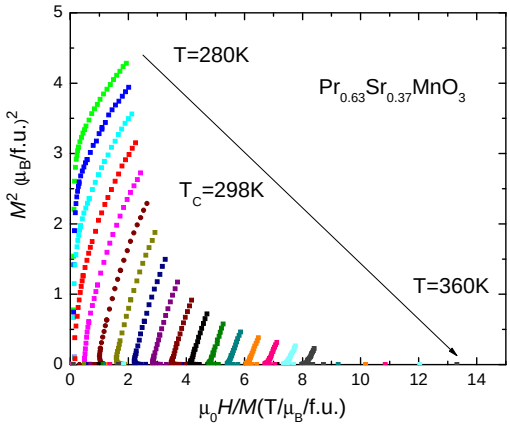

Fig. 6. Arrot plots for $Pr_{0.63}Sr_{0.37}MnO_3$ sample obtained from measured M vs. $\mu_0 H$ isotherms.

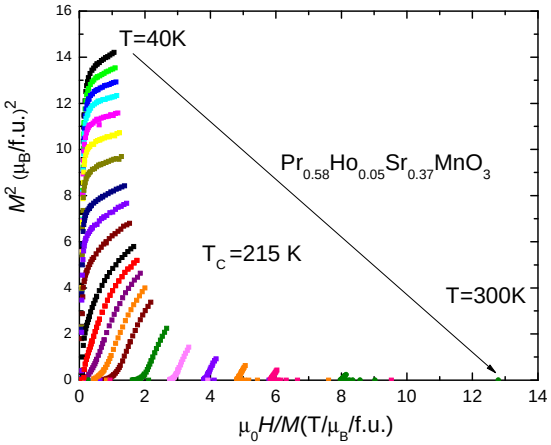

Fig. 7. Arrot plots for $Pr_{0.58}Ho_{0.05}Sr_{0.37}MnO_3$ sample obtained from measured M vs. $\mu_0 H$ isotherms.

As can be seen from these plots all the M^2 vs μ_0H/M curves have positive slopes, indicating the second order character of the phase transition.

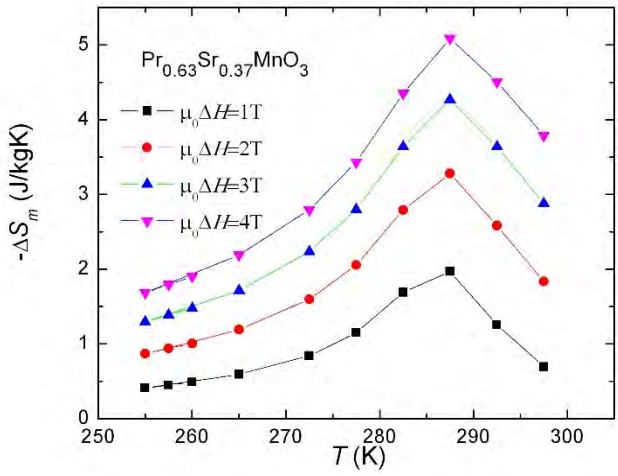

Fig. 8. The magnetic entropy change – ΔSM as a function of temperature for $\mu_0\Delta H$=1,2,3 and 4T, in $Pr_{0.63}Sr_{0.37}MnO_3$.

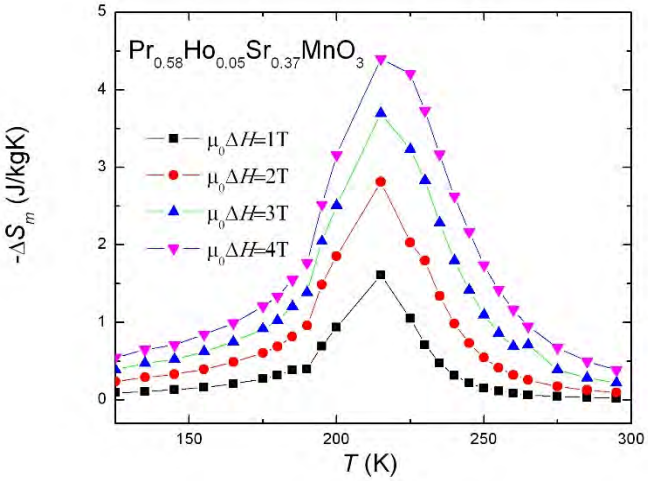

Fig. 9. The magnetic entropy change – ΔSM as a function of temperature for $\mu_0\Delta H$=1,2,3 and 4T, in $Pr_{0.58}Ho_{0.05}Sr_{0.37}MnO_3$.

In these cases, by using the formula (1) we calculated the magnetic entropy change for our samples, and the temperature dependences of $-\Delta S_M(T)$ are plotted for different values of $\mu_0\Delta H$ between 1 and 4 T as shown in Figs. 8 and 9.

The maximum values of magnetic entropy change curves are located in the vicinity of the Curie temperature T_C, for both of ours samples, 298 K for x = 0 and 216 K for x = 0.01. The transition range enlarges in higher applied magnetic fields, and δT_{FWHM} also increases. This behavior results in a large relative cooling power, *RCP,* corresponding to a material with a higher cooling efficiency. The shapes of the $-\Delta S_M$ (T) curves are rather symmetric with respect to the T_C's, which is also important for a magnetic refrigerator. The maximum values of $\Delta S_M(T)$ reach 5.09 J/kg·K (*RCP* = 184 J/kg) for μ_0 ΔH = 4 T for the sample with x = 0 and 4.38 J/kg·K (*RCP* = 236J/kg) for μ_0 ΔH = 4 T for the sample with x = 0.01.

Some quantitative parameters related to magnetocaloric effect in the two samples are given in Tables 1 and 2.

Table 1. T_C, $-\Delta S_M^{max}$, δT_{FWHM} and *RCP* when $\mu_0\Delta H$ = 1, 2, 3 and 4 T for the sample $Pr_{0.63}Sr_{0.37}MnO_3$

$\mu_0\Delta H$ (T)	T_C (K)	$-\Delta S_M^{max}$ (J.kg^{-1}·K^{-1})	δT_{FWHM} (K)	*RCP* (J·kg^{-1})
1	288	1.96	22	42.0
2	289	3.27	24	79.2
3	289	4.26	34	143.5
4	289	5.09	38	184.7

As can be seen from the Table 1 and 2, both the samples show large maximum value of the magnetic entropy change $-\Delta S_M^{max}$. When Ho^{3+} ions substitute for Pr^{3+} the $-\Delta S_M^{max}$.do not depreciate to much (from 5.09 to 4.40 J.kg^{-1}·K^{-1} for $\mu_0\Delta H$ = 4T); *RCP* increases (from 184.7 to 236.5 J·kg^{-1} for $\mu_0\Delta H$ = 4T) and T_C was strongly decreased from 298 to 215 K.

Such a behavior is expected in a compound that presents a large lattice distortion and consequently a strong spin disorder. Since we have a high ionic size mismatch between Pr^{3+} and Ho^{3+} the local disorder created will result in a drastically reduction of Curie temperature and in broadening of the magnetic phase transition. But the strong spin-lattice coupling in $Pr_{0.63-x}Ho_xSr_{0.37}MnO_3$ compounds may keep large values for the magnetic entropy change, for a large MCE [9].

Table 2. T_C, $-\Delta S_M^{max}$, δT_{FWHM} and *RCP* when $\mu_0\Delta H$ = 1, 2, 3 and 4 T for the sample $Pr_{0.58}Ho_{0.05}Sr_{0.37}MnO_3$

$\mu_0\Delta H$ (T)	T_C (K)	$-\Delta S_M^{max}$ (J.kg^{-1}·K^{-1})	δT_{FWHM} (K)	*RCP* (J·kg^{-1})
1	215	1.61	36	57.9
2	216	2.81	43	120.8
3	218	3.70	49	182.3
4	216	4.40	54	236.5

This behavior suggests the possibility of tuning the Curie temperature of the $Pr_{0.63-x}Ho_xSr_{0.37}MnO_3$ compounds to cover the temperature range of the conventional domestic refrigerators by reducing the Ho ions concentration below x = 0.05, while the magnetic entropy change still maintains large values.

CONCLUSIONS

Magnetic properties and magnetocaloric effect in $Pr_{0.63-x}Ho_xSr_{0.37}MnO_3$ manganites (where x = 0; 0.01) were studied in detail. The compounds have ferromagnetic behavior below the Curie temperature. Replacing Pr^{3+} ions by Ho^{3+} ions results in a drastically reduction of the Curie temperature (T_C =215 K), while the magnetic entropy change and the relative cooling power still keep large values ($-\Delta S_M^{max}$ = 4.40 J/kg·K and *RCP* = 236 J/kg for ì$_0$ Ä*H* = 4 T) which recommend these compounds to be used in refrigeration applications in near room-temperature range.

ACKNOWLEDGMENTS

This work was supported by the Romanian Ministry of Research an Innovation through CCCDI-UEFISCDI, by Complex Projects of Frontier Research [PN-III-P4-ID-PCCF-2016-0112] (I.G.D.).

REFERENCES

1. A.M. Tishin, Y.I. Spichkin, The Magnetocaloric Effect and Its Applications, Institute of Physics, Bristol, 2003.
2. K.A. GschneidnerJr., V.K. Pecharsky, A.O. Tsokol, *Rep. Prog.Phys.* 68 (2005) 1479 –1539.
3. M.-H. Phan, S.-C. Yu, *J. Magn. Magn. Mater.* 308 (2007) 325–340.
4. V.B. Naik, S. K. Barik, R. Mahendiran, B. Raveau, *Appl. Phys. Lett.* 98 (112506) (2011) 1–3.
5. A. Varvescu, I.G. Deac, *Physica B* 470-471 (2015) 96–101.
6. R.-M. Thomas, V. Skumryev, J.M.D. Coey, *J. Appl. Phys.* 85 (1999) 5384–5386.
7. A. Arrott, *Phys. Rev.* 108(1957) 1394–1396.
8. S.K. Banerjee, *Phys. Lett.* 12 (1964) 16–17.
9. Y.I. Spichkin, A.M. Tishin, *J. Alloy. Compd.* 403 (2005) 38–44.

STUDIA UBB PHYSICA, Vol. 66 (LXVI), 1-2, 2021, pp. 79-90
(RECOMMENDED CITATION)
doi:10.24193/subbphys.2021.08

THE EFFECT OF ALKALI AND SURFACTANT CONCENTRATION, TEMPERATURE AND STIRRING ON THE CLEANING EFFICIENCY OF THE CARBON STEEL SURFACE

A. MIHIS[1], V. DANCIU[1,2], C.A. SALAGEAN[1,3], I. SZÉKELY[3,4], M.V. RACOLTA-PAINA[1], S.C. TRIPON[5,6], L.C. COTET[1,2], K. MAGYARI[1,4], L. BAIA[1,3,4]

ABSTRACT Electrostatic painting is the fastest and most efficient technology through industrial paints due to its impact on the environment, and also for its very easy application on different surfaces. The first and most important stage of the electrostatic painting is to clean the surface to be painted by removing the dirt, lubricants, oils, metal oxides or welding residues. In order to increase the efficiency of carbon steel surface cleaning, the influence of alkali and surfactant concentrations, temperature and stirring was investigated. To produce a uniform surface required for the electrostatic painting, some degreased samples were subjected to pickling operation using aqueous HCl solution.

Keywords: *carbon-steel, degreasing, pickling, ultrasonication*

INTRODUCTION

A relatively new painting process, which is especially used in industrial or commercial applications, is electrostatic painting. This is the fastest and most efficient technology through industrial paints due to its impact on the environment,

[1] *Laboratory for Advanced Materials and Applied Technologies, Institute for Research, Development and Innovation in Applied Natural Sciences, Babeș-Bolyai University, Fantanele 30, Cluj-Napoca RO-400294, Romania*

[2] *Faculty of Chemistry and Chemical Engineering, Babeș-Bolyai University, Arany Janos 11, RO-400024, Cluj-Napoca, Romania*

[3] *Faculty of Physics, Babeș-Bolyai University, M. Kogalniceanu 1, Cluj-Napoca RO-400084, Romania*

[4] *Centre of Nanostructured Materials and Bio-Nano Interfaces, Institute for Interdisciplinary Research on Bio-Nano-Sciences, Treboniu Laurian 42, Cluj-Napoca RO-400271, Romania*

[5] *Electron Microscopy Centre, Faculty of Biology and Geology, Babeș-Bolyai University, 44 Republicii, 400015 Cluj-Napoca, Romania*

[6] *Integrated Electron Microscopy Laboratory, National Institute for Research and Development of Isotopic and Molecular Technologies, 67-103 Donath, 400293 Cluj-Napoca, Romania*

* *Corresponding author: lucian.baia@ubbcluj.ro*

and also for its very facile application on different surfaces. At the same time, this type of painting can have a long warranty period compared to other painting methods. The electrostatic painting process is composed of several essential steps. The first stage is the chemical treatment which consists in removing dirt, lubricants, oils, metal oxides or welding residues from the part to be painted. Usually, these impurities come from mechanical processes of brushing or polishing. In the degreasing process, the organic pollutants due to mechanical or heat treatments are removed. In the pickling process, inorganic substances (rust, welding residues, stains, solid particles) are eliminated [1]. The degreasing efficiency depends both on the composition of the degreasing solution and the composition of the steel's pollutant. The degreasing mixture acts on the surface tension of the polluting particles and contains substances which facilitates emulsion, solubilization, flocculation and steel surface wetting action. The steel's pollutant are substances with polar groups that are absorbed onto the surface of the steel or by free fatty acids that form soaps adherent to the metal surface. In general, for chemical degreasing, a solution consisting of mild or strongly alkaline electrolyte, salt mixture and surfactants is used. The degree of electrolyte alkalinity depends on the sheet metal to be degreased. For degreasing steel and stainless steel, strong alkaline electrolyte is used. As a result of the chemical reaction between the alkaline substance and the oils and/or fats, these pollutants are removed by saponification. The salt mixture serves as a so-called builder substance and forms the basis of the solution. The surfactant lowers the surface tension and promotes, at a certain concentration, the formation of micellar solutions instead of molecular solutions [2-4]. The application of the degreasing mixture is done either by spraying or by immersion. The spraying application is used to eliminate large quantities of residues. In this case, the mixture is composed of alkali with silicates and phosphates. The immersion process involves introduction of the product in a high temperature alkaline solution. The high temperature reduces the viscosity of the impurities, increases the rate of chemical reactions. Therefore, the degreasing power is mainly due to the combined action of temperature, emulsifying power of the solution and mechanical or ultrasound agitation [5].

Agitation cleaning is ideal for hard metal objects that are placed on a moving platform. By moving the platform, the cleaning agent comes in contact with the bulk of the object and removes the contamination. Ultrasonic cleaning utilizes certain physical forces which occur when liquids are agitated by sound waves created by ultrasonic generators. The microscopic bubbles of vacuum created by ultrasonic stirring, form and collapse thousands of times each second. With each implosion, strong enough shockwaves to remove surface contamination are produced. The efficiency of ultrasonic stirring depends on the intensity of ultrasonic cavitation in the liquid, stirring time, temperature and chemical composition of the degreasing

solution. The increase of temperature determines the decrease of the liquid viscosity and the amount of dissolved gas, which leads to increasing the cavitation intensity. The moderate increasing of the liquid temperature brings it closer to its vapor pressure, and so the most effective form of cavitation, in which the cavitation bubbles are filled with the vapor of the cavitating liquid, is achieved. The optimum temperature for the most highly caustic cleaners is between 80-90^{o}C, the chemical effect being strongly enhanced at this temperature.

The current paper investigates the effect of alkali (PRESOL 7120, 6-90g/l) and surfactant (AB40, 2.5 to 10 ml/l) concentration, temperature (50 to 70^{o}C) and stirring type (magnetic or ultrasonic) and time (5 to 15 min) on the degreasing/ pickling efficiency of the carbon steel (S235 plate). To produce a uniform surface characteristic required for the electrostatic painting, some chosen degreased samples were subjected to pickling operation for 15 min using 15% aqueous HCl solution.

EXPERIMENTAL

Materials and Methods

To evaluate the influence of different parameters on the degreasing / pickling efficiency, samples of carbon steel plate S235 (C% - max 0.22; Mn% - max 1.60; S% - max 0.05; P% - max 0.05; Si% - max 0.05) from CAN STEEL PRODUCTION SRL, having dimensions (20x10x1) mm, are used. The steel samples were clamped to a support placed on the edge of the Berzelius cup (V-150ml) so that the entire sample surface was immersed in the degreasing solution. After each degreasing / pickling operation, the samples were three times washed with distilled water and then dried with hot air.

To prepare the degreasing electrolyte PRESOL 7120 was used (COVENTYA S.A.S, 92588 CLICHY CEDEX – FRANCE) consisting of sodium hydroxide (50-100%) and disodium metasilicate (10-25%) which was dissolved in distilled water. The Presol concentration was varied between 6 and 90 g/l.

Surfactant AB 40 consisting of C12-14 alcohols (ethoxylated and sodium sulphates salts) 25-50%, non-ionic surfactant < 2.5%, sodium dodecylbenzene sulphonate 10-25% and phosphoric acid < 2.5% was used for adjusting the surface tension of the degreasing electrolyte. Its concentration ranged from 2.5 to 10 ml per liter of degreasing electrolyte. To prepare the 15% aqueous HCl solution used at pickling operation it was used HCl 37% from Sigma-Aldrich.

For stirring of the degreasing electrolyte, a magnetic stirrer MSH-20D (WITEG LABORTECHNIK GmbH, Wertheim Germany) provided with a heating system and temperature sensor, respectively, an ultrasonic cleaner (ultrasound power- 60W, volume 1.3L) equipped with temperature and duration control system, produced by ISOLAB LABORGERÄTE GmbH, Germany was used. The Presol concentration was determined by titration with 1N HCl in the presence of the phenolphthalein until that a colour change from violet to colourless was observed. Concentration of degreaser in the bath was calculated using the formula: C_{Presol} (g/l) = $V_{ml\ of\ HCl}$ x 5.56.

The surface tension of degreasing solutions was measured using the drop volume method and the formula:

$$\sigma = \sigma' \cdot \frac{n'}{n} \cdot \frac{\rho}{\rho'}, \quad (1)$$

where σ', n' and ρ' represent surface tension, drop number and density for distilled water, while n and ρ represent the number of drops and density, respectively, for degreasing solution [6]. The degreasing efficiency was followed by scanning electron microscopy-energy-dispersive X-ray (SEM-EDX) using a Hitachi SU8230 scanning electron microscope, at an electron acceleration of 30kV, obtaining images between 30x to 50,000x magnification. The samples were sectioned to the size of 0.5 / 0.5 cm, using a diamond disk with the Micracut 151 device. Then, the samples were fixed on brass supports (stabs) of the microscope with the help of double-sided carbon sticks from Agar Scientific with a diameter of 12 mm and with silver paste also from Agar Scientific. For all samples, images were taken at identical magnifications: 30x, 100x, 500x, 1000x, 5000x, 10,000x, 20,000x, 50,000x. EDX (Energy-dispersive X-ray spectroscopy) analyses were performed using AZtech software from Oxford Instruments, obtaining at least two spectra per sample. A mapping analysis of the distribution of chemical elements in the sample was also performed.

RESULTS AND DISCUSSION

As it can be seen from **Fig.1 A**, the surface tension decreases with the increasing surfactant concentration. In the logarithmic representation of the surface tension as a function of the surfactant concentration there are two linear regimes, namely below and above the critical micelle concentration (CMC) (see **Fig. 1B**). The common procedure to determine the CMC from experimental data is to look for the intersection of two straight lines traced through plots of the measured property versus the surfactant concentration. The CMC is the surfactant concentration from which the micelles are formed. Above the CMC, the interfacial surfactant concentration does not change any more and the surface tension of the solution is practically constant.

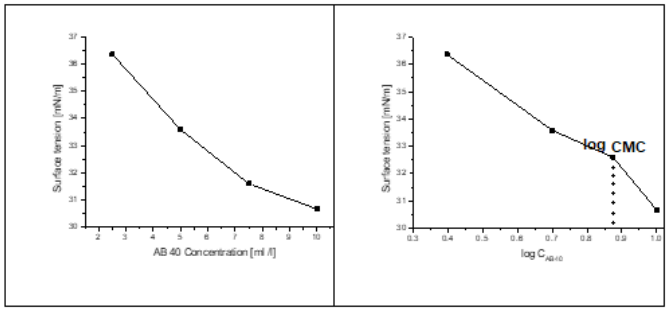

Fig. 1. Surface tension of the AB 40 aqueous solution for different concentration of surfactant (**A**) and surface tension vs. logarithm of AB 40 concentration (**B**). The errors were found to be of maximum 5% of the measured values.

In **Fig. 2** it can be seen that the value of the surface tension increases with increasing of the Presol concentration.

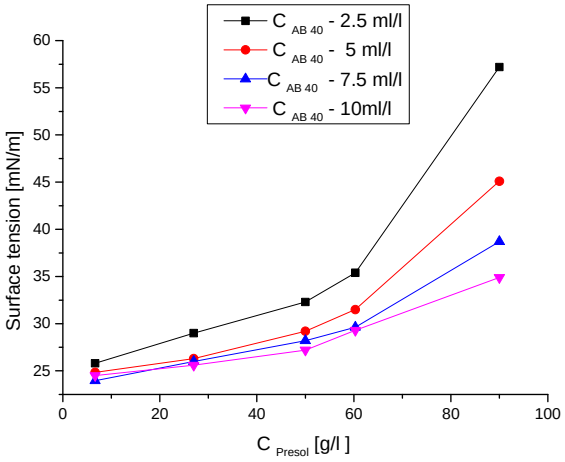

Fig. 2. Surface tension of the degreasing solution vs. Presol 7120 concentration at different AB 40 surfactant concentrations

This means that Presol is tensioinactive, its concentration being lower in the surface layer than inside of the liquid phase. However, it can be observed that as the surfactant concentration increases from 2.5 to 10ml/l, the surface tension decreases. This decreasing surface tension is due to the fact that in the surface layer the concentration of the dissolved substances is larger than inside the liquid phase, so the molecules dissolved are adsorbed at the interface.

In the graphical representation of the surface tension vs. AB 40 concentration (see **Fig.3**) it can be observed that as the Presol concentration increases, the change of slope takes place at increasing values of surfactant concentration. This means that the increase of the Presol concentration, in the degreasing solution, leads to delay in the onset of micelle formation, respectively to the increase of the critical micellar concentration of the AB 40 surfactant (see **Table 1**).

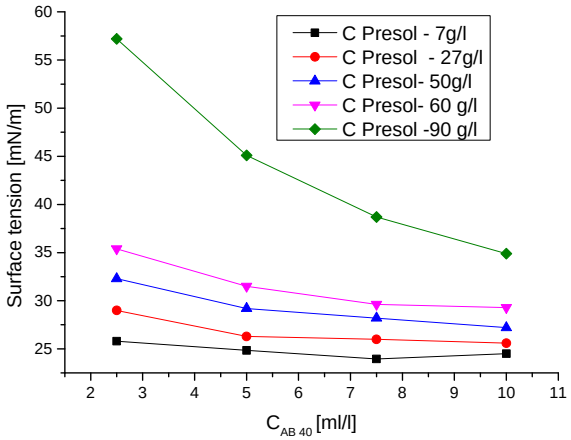

Fig. 3. Surface tension of the degreasing solution vs. AB 40 surfactant concentration at different Presol 7120 concentrations

In the degreasing process, the formation of micelles is desirable and therefore the knowledge of the CMC is very important. Critical micellar concentration specifies the limiting concentration for meaningful use and it is a measure of the efficiency of a surfactant.

Table 1. Critic micellar concentration of the surfactant AB 40 at different Presol concentration

C_{Presol} [g/l]	log CMC	$CMC_{AB\ 40}$ [ml/l]
0	0.875	7.5
7	0.699	5
27	0.699	5
50	0.699 - 0.875	5 - 7.5
60	0.875	7.5
90	>1	>10

In the **Figs. 4 and 5** the SEM images, and the elemental composition determined by EDX of the carbon steel sample, before and after degreasing operation, are showed.

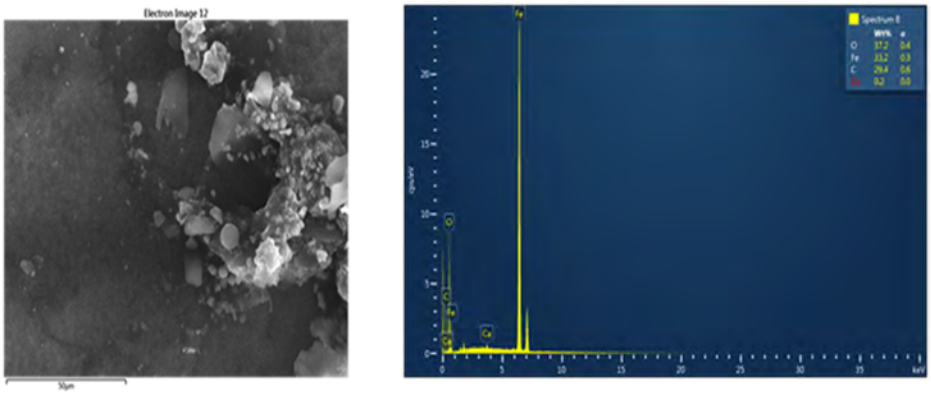

Fig. 4. Selected SEM image of the non-degreased carbon steel sample and its elemental composition determined by EDX

The experiments performed under different stirring speeds highlighted the beneficial effect of electrolyte agitation on the cleaning process of the sample. As can be seen from **Fig. 6**, after 15 minutes of degreasing of the carbon steel sample at temperature of 60^{O}C, in a solution containing 50 g/l Presol and 7.5 ml/l AB 40, the percentage of carbon determined by EDX analysis, decreases from 29.9 to 17.8 and respectively from 29.9 to 14.3% with increasing agitation speed from 400 to 800rpm.

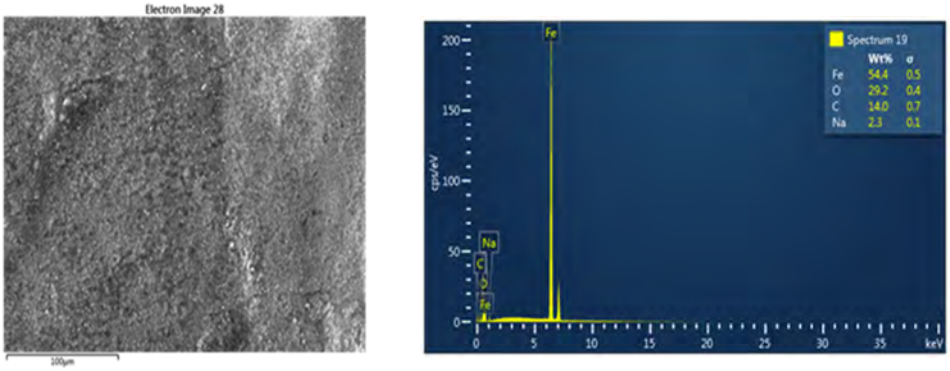

Fig. 5. Selected SEM image of the carbon steel sample degreased in the electrolyte containing 50g/l Presol and 10ml/l AB 40, at 70^{0}C, 600rpm, 5min and its elemental composition determined by EDX

As the cleaning solution dissolves the surface contaminant, a saturated layer develops at the interface between the fresh cleaning solution and the contaminant.

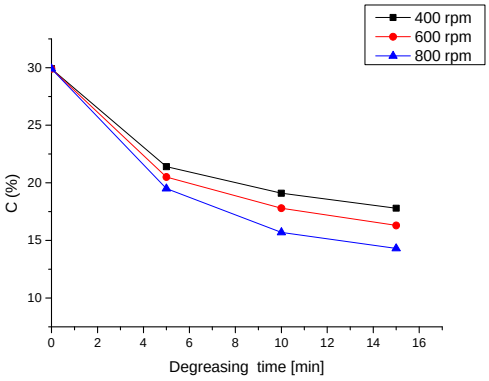

Fig. 6. Decreasing the percentage of carbon vs. degreasing time using a solution with 50 g/l Presol and 7.5 ml/l AB 40 at different stirring speeds and temperature of 60^{O}C

Saturated solution can no longer attack the contaminant and therefore the cleaning action stops. By increasing of the stirring, a fresh degreasing solution can reach easier the contaminant. Increasing the temperature of the degreasing electrolyte from 50 to 70^{0}C favors the removal of organic pollutants from the surface of the carbon steel sample, the percentage of carbon decreasing from 8.5 to 5.3% at 50^{0}C and respectively from 8.5 to 3.2 % at 70^{0}C (see fig.7). Higher temperatures decrease the contaminants viscosity, and increase the diffusion of the degreasing solution to the steel surface, allowing easier contaminant removal. Increasing the Presol concentration from 30 to 90g/l leads to decrease of the carbon concentration from 14.2 to 1.8% after 15 min of degreasing at 70^{0}C and a stirring speed at 800rpm (see fig.8). Increasing the Presol concentration, increase the NaOH concentration which converts, by saponification, the natural fats, i.e., esters of glycerol and higher fatty acids, into glycerol and the sodium salt. These substances are water soluble and are easy removed by rinsing. The mineral fats (oils) are not decomposed by alkalis but are dispersed and suspended in alkaline solutions through an emulsification process. As the increase of the Presol concentration also increases the concentration of the sodium metasilicate (present in Presol degreaser along with NaOH). This being an excellent emulsifying and suspending agent the increase of its concentration determines the improvement of the degreasing efficiency [7].

To dissolve iron oxides from the surface of carbon steel sample and to clean light rust without any significant attack on the steel itself, the HCl acid pickling was used. HCl pickling has the advantages of lower costs, lower acid consumption and greater utilization of the acid, greater versatility and more uniform product quality than sulfuric acid pickling. Pickling rate increases as acid concentration and for this reason an acid solution with a concentration of 15% HCl was used.

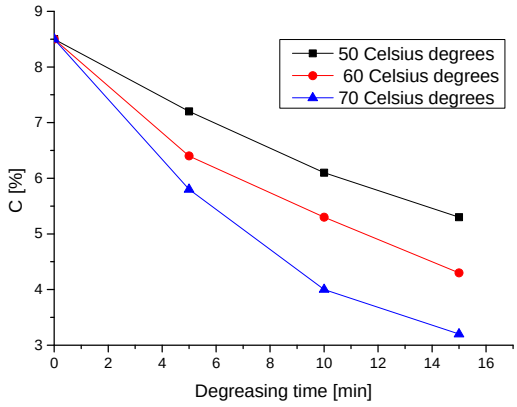

Fig. 7. Decreasing of the percentage of carbon vs. degreasing time using a solution with 50 g / l Presol and 7.5 ml / l AB 40 at a stirring speed of 600rpm

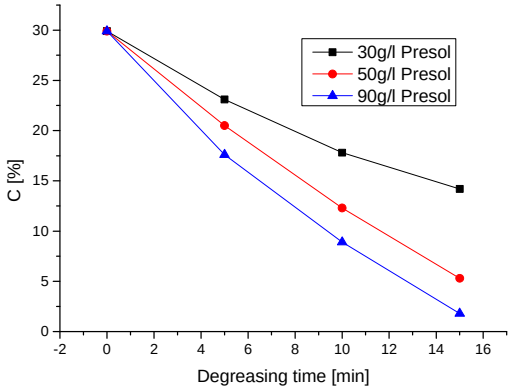

Fig. 8. Decreasing of the percentage of carbon vs. degreasing time at temperature of 70^0C using a solution with different concentration of Presol, an AB 40 concentration of 7.5 ml/l and a stirring speed of 800rpm

As it can be seen from **Fig. 9**, after 15 min of HCl pickling at room temperature, the oxygen concentration of the degreased sample decreased from ~37 to ~5%. Practically, the acid dissolves the iron oxides presence on the steel surface according to the following reaction mechanism:

$$Fe_2O_3 + Fe + 6HCl = > 3\ FeCl_2 + 3H_2O$$
$$Fe_3O_4 + Fe + 8HCl = > 4FeCl_2 + 4H_2O$$
$$FeO + 2HCl = > FeCl_2 + H_2O$$

By iron oxides elimination, the HCl pickling permits proper adherence of a subsequent metallic coatings and promotes surface smoothness of the finished product.

As it can be seen from **Fig. 10**, the pickling operation can be avoided by using steel degreasing in the presence of ultrasound. It is observed that by degreasing in the presence of ultrasound for 5 min, the iron oxides are practically removed from the surface of the steel sample. The effect of ultrasonication is consistent with the micro-agitation helping both the dissolution of soluble contaminants and the removal of insoluble particles. Ultrasonic activity enhances also the effect of many chemical reactions by high pressures and temperatures created at the implosion sites. Ultrasonic cavitation and implosion effectively displace the saturated layer on the steel surface to allow fresh degreasing solution to come into contact with the contaminant remaining to be removed [8].

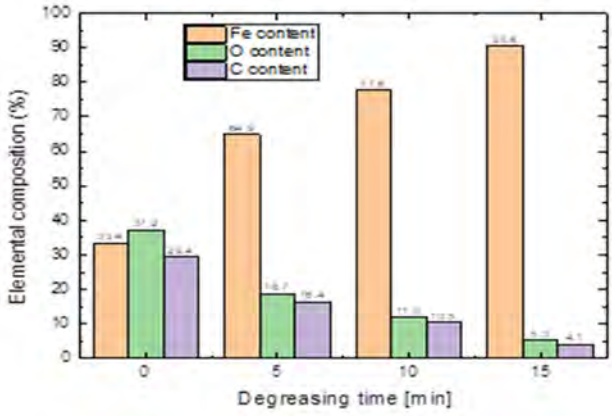

Fig. 9. Elemental composition of the carbon steel samples degreased at 70^0C and magnetic stirred (600rpm) with an aqueous solution containing 50g/l Presol and 7.5 ml/l AB 40, and then pickled in 15 % hydrochloric acid for 15 min, the stirring speed being 400rpm

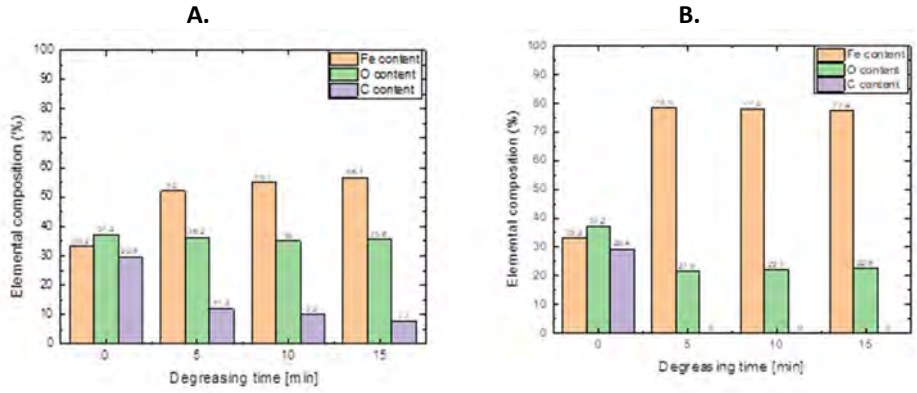

Fig. 10. Elemental composition of the carbon steel samples vs. degreasing time at 70^0C, in an aqueous solution containing 50g/l Presol and 7.5 ml/l AB 40 using magnetic stirrer (600rpm) (**A**) or performing degreasing in the presence of ultrasound (**B**)

Properly utilized, ultrasonics is a technology of today, the ultrasonic energy contributes significantly to the speed and effectiveness of immersion cleaning processes.

CONCLUSIONS

Increase of the Presol concentration leads to delay in the onset of micelle formation, respectively to the increase of the critical micellar concentration of the AB 40 surfactant. The AB 40 concentration must be at least 7.5ml/l for Presol concentration greater than 50g/l.

With Presol concentration and electrolyte temperature increasing, from 50 to 90g/l, and respectively from 50 to 70^0C, the efficiency of the steel surface cleaning process has improved.

To dissolve iron oxides from the surface of carbon steel sample and to clean light rust without any significant attack on the steel itself the HCl acid pickling can be used after the degreasing stage or performing degreasing in the presence ultrasound.

ACKNOWLEDGMENT

The authors acknowledge UBB TeMATIC-Art P_40_374 project for the financial support.

REFERENCES

1. R. Crookes, “Pickling and Passivation Stainless Steel, Materials and Application series”, Editor Euro Inox, Second Edition 2007, vol. 4
2. G. Kjærheim, “Introduction of Modern Methods for Degreasing of Metal Parts”. In: “Cleaner Technologies and Cleaner Products for Sustainable Development, NATO ASI, Springer-Verlag Berlin Heidelberg, 1995, Series 2
3. https://www.nitty-gritty.it/en/stainless-steel-degreasing-part-1/
4. M.L. Free, “The Use of Surfactants to Enhance Particle Removal from Surfaces”, In Developments in Surface Contamination and Cleaning, Vol. 1: Fundamentals and Applied Aspects, Editors: R. Kohli, K. L. Mittal, 2nd ed.”, Elsevier Inc., 2016, chapter 13
5. G. Critchlow, “General Introduction to Surface Treatments”, Handbook of Adhesion Technology, Springer-Verlag Berlin Heidelberg, 2011
6. E. Chifu, M. Tomoaia Cotisel, I. Albu, A. Mocanu, M.I. Salajan, C.Racz, D.V. Pop, “Metode experimentale in chimia si biofizica coloizilor si a interfetelor”, Presa Universitara Clujeana, 2004
7. A.E. Hargreaves, “Chemical Formulation: An Overview of Surfactant-based Preparations Used in Every Day Life”, Royal Society of Chemistry, 2003
8. Fuchs, F. John, “Ultrasonic Cleaning: Fundamental theory and application”, NASA. Marshall Space Flight Center, Aerospace Environmental Technology Conference, Blackstone Corp. Jamestown, NY, United States, 1995

STUDIA UBB PHYSICA, Vol. 66 (LXVI), 1-2, 2021, pp. 91-110
(RECOMMENDED CITATION)
doi:10.24193/subbphys.2021.09

PERPENDICULAR MAGNETIC ANISOTROPY AND ITS ELECTRIC FIELD MANIPULATION IN MAGNETIC MULTILAYERED HETEROSTRUCTURES

ROXANA-ALINA ONE[1], SEVER MICAN[1], CORIOLAN VIOREL TIUSAN[1,2,3] *

ABSTRACT. Understanding of underlying physics related to the Perpendicular Magnetic Anisotropy (PMA) in magnetic heterostructures represents a major issue for its exploit in random-access memory (MRAM) devices. Using ab-initio analysis, we reveal some basic aspects related to the anatomy of PMA and its variation with electric field in various *X*/Fe/MgO(001) multilayer configurations (*X*=Cr, Au, V, Ag, Pt, Pd,…) compatible with standard experimental architectures of magnetic tunnel junction devices. Our study quantifies and underlines the significant role of the Rashba interfacial field on PMA. We explain and correlate the sign, the magnitude, and the electric field dependence of the PMA, the Rashba coefficient α_R and the Dzyaloshinskii–Moriya (DMI) asymmetric exchange interaction parameter. Moreover, when varying the Fe thickness in X/Fe/MgO(001) systems, we observe oscillations of PMA with the number of Fe monolayers, explained within the framework of quantum wells of the Δ_1 Bloch symmetry electrons in Fe. Further atomistic micromagnetic simulations including different Fe layer thicknesses and the corresponding PMA predict macroscopic magnetization characteristics in realistic experimental systems.

Keywords: *perpendicular magnetic anisotropy, electric field control of PMA, magnetic tunnel junctions, magnetic multilayer heterostructures, atomistic magnetic simulations.*

INTRODUCTION

Perpendicular Magnetic Anisotropy (PMA) in ultrathin magnetic films represents one of the most challenging topics for data storage applications, related to both high thermal stability and low switching currents in spin-transfer-torque

[1] *Babeș-Bolyai University, Faculty of Physics, 1 M. Kogălniceanu, 400084, Cluj-Napoca, Romania*
[2] *Technical University of Cluj-Napoca, Department of Physics and Chemistry, 28 Memorandumului, 400114, Cluj-Napoca, Romania*
[3] *National Center of Scientific Research, France*
* *Corresponding author: coriolan.tiusan@ubbcluj.ro*

magnetic random-access memories (MRAM). A deep understanding of fundamental underlying physics related to the PMA anatomy in magnetic multilayer structures represents a major issue for further exploit in MRAM devices [1]. The control of the interfacial magnetic anisotropy by external electric fields leads to a novel strategy for the control of the magnetization in spintronic devices with enhanced energetic efficiency [2]. Within this paradigm, energy consumption of few fJ/bit [3,4] and sub-nanosecond switching times can be achieved [5]. Despite obvious recent advances, the control of ultra-thin ferromagnetic layers magnetism by external electric field remains a complex topic with complex mechanisms simultaneously involved. It is commonly accepted that the PMA in ultrathin magnetic heterostructures has interfacial origin: proximity effects at the interfaces with non-magnetic materials with enhanced spin-orbit coupling (e.g. Pt, Au…) and intrinsic electric field and specific hybridization at interfaces with oxides (e.g. MgO). Within this last framework, an external electric field would trigger a modulation of the magnetic anisotropy via the following competing effects: (i) E-field induced surface charge doping (change of orbitals occupancy [6,7]); (ii) E-field influence on the interfacial dipole field that exists at the ferromagnetic/insulator interface even in the absence of an external magnetic field. The anisotropy energy is not located at the interface but extends towards the bulk like an attenuated wave [8]; (iii) the E-field effect on the interfacial Rashba spin-orbit coupling that affects the magnetic anisotropy energy via a Dzyaloshinskii-Moriya mechanism [9]; (iv) E-field induced ion migration [10]. Within this still open fundamental topic one can argue that the electric field control of the anisotropy is driven by collective mechanisms and that a better understanding of the underlying physics could lead to an enhancement of potential capabilities for energetically efficient magnetization manipulation in spintronic devices.

In this study we involve ab-initio analysis and atomistic magnetic calculations to unveil some basic aspects related to the anatomy of PMA and its variation with electric field in *X*/Fe/MgO(001) multilayer configurations (*X*=Cr, Au, V, Pd, Pt, Ag…) compatible with standard experimental architectures of magnetic tunnel junction devices. Moreover, our study quantifies and underlines the significant role of the Rashba interfacial field on PMA, explaining and correlating the sign, the magnitude, and the E-field dependence of the PMA, the Rashba coefficient α_R and the Dzyaloshinskii–Moriya (DMI) asymmetric exchange interaction parameter. In *X*/Fe/MgO(001) systems with a variable Fe thickness we illustrate oscillations of PMA with the number of the Fe monolayers related to quantum well effects. Based on electronic structure characteristics extracted from the ab-initio calculations, we performed atomistic micromagnetic simulations to predict macroscopic magnetization characteristics corresponding to nanostructures with different Fe thicknesses and related PMA amplitudes.

THEORETICAL DETAILS

The theoretical study of the PMA and its field control has been performed using the ab-initio *Full Potential Linear Augmented Plane Wave FP-LAPW* code *Wien2k* [11]. In our calculations we involved a super-cell model thoroughly chosen to describe the *X*/Fe/MgO(001) multilayer configuration.

Magnetic anisotropy calculations in Wien2k

The magnetic anisotropy energy (MAE) has been calculated within a fully relativistic spin orbit scheme using total energy and force theorem approaches [12], both providing similar results. Within the total energy approach, the MAE is calculated as the difference between the total energy *E*[*uvw*] deduced from spin orbit calculation with the magnetization along the [*uvw*] crystallographic direction and the total energy corresponding to the magnetization along the easy axis:

$$MAE = E[uvw] - E[easy\ axis]$$

The force theorem approach is a perturbative formalism in which the MAE between two different magnetization directions $\vec{m}_1$ and $\vec{m}_2$ is given by:

$$MAE = \sum_{i,k}^{occ} \varepsilon_i^1(\vec{m}_1, k) - \sum_{i,k}^{occ} \varepsilon_i^1(\vec{m}_2, k)$$

where the superscript 1 denotes the band energies calculated using the fully relativistic charge/spin density of magnetization $\vec{m}_1$.

Spin-orbit coupling in Wien2k

The quantum mechanics description of electrons, consistent with the theory of special relativity is provided by the Dirac equation: $H_D\Psi = \varepsilon\Psi$, where H_D is the Dirac Hamiltonian: $H_D = c\vec{\alpha}\cdot\vec{p} + \beta mc^2 + V$.
$\alpha_k = \begin{pmatrix} 0 & \sigma_k \\ \sigma_k & 0 \end{pmatrix}$, $\beta_k = \begin{pmatrix} 1 & 0 \\ 0 & -1 \end{pmatrix}$ and σ_k are the Pauli matrices: with: $\sigma_x = \begin{pmatrix} 0 & 1 \\ 1 & 0 \end{pmatrix}, \sigma_y = \begin{pmatrix} 0 & -i \\ i & 0 \end{pmatrix}$, $\sigma_z = \begin{pmatrix} 1 & 0 \\ 0 & -1 \end{pmatrix}$. H_D and the wave function are 4-dimensional objects. Within the non-relativistic limit of the Dirac equation the electrons are moving with velocities much smaller than the speed of light. Some

relativistic effects can be neglected, and they can be described by the Pauli equation which considers the interaction of the particle spin with an external electromagnetic field. The corresponding Pauli Hamiltonian can be written as:

$$H_P = -\frac{\hbar}{2m_0}\nabla^2 + V_{eff} + \mu_B \vec{\sigma} \cdot \vec{B}_{eff} + \xi\left(\vec{\sigma} \cdot \vec{l}\right)$$

The first term is the kinetic term in the Schrödinger equation, the second term is an electrostatic effective potential, the third term is a Stoner term describing the Zeeman interaction of the spin with an external effective magnetic field and the fourth term the spin-orbit coupling term. $\vec{\sigma}$ is the Pauli matrices vector $\vec{\sigma} = \left(\sigma_x, \sigma_y, \sigma_z\right)$ and ξ is the constant of the spin-orbit interaction. The matrix of the Pauli Hamiltonian is 2x2 in the spin space. Due to the Pauli spin operators the wave function is a 2-component vector (spinor), each component $\Psi_{1(2)}$ being associated to a spin orientation 1=up, 2=down): $H_P \begin{pmatrix} \Psi_1 \\ \Psi_2 \end{pmatrix} = \varepsilon \begin{pmatrix} \Psi_1 \\ \Psi_2 \end{pmatrix}$.

The effective potential is a sum of an external potential, an electrostatic Hartree term and an exchange-correlation potential: $V_{eff} = V_{ext} + V_H + V_{xc}$. The effective magnetic field is composed by an external field and an exchange correlation field: $B_{eff} = B_{ext} + B_{xc}$. Both exchange correlation potential V_{xc} and magnetic field B_{xc} are defined within the Density functional Theory (DFT) in either Local Density Approximation (LDA) or Generalized Gradient Approximation (GGA).

Exchange and correlation

From the DFT LDA exchange-correlation energy defined as an integral of the exchange-correlation energy ϵ_{xc} per particle of a homogeneous electron gas of electronic charge density *n(**r**)* and spin density $\vec{m}(\boldsymbol{r})$:

$E_{xc}(n, \vec{m}) = \int n\epsilon_{xc}(n, \vec{m})dr^3$ one can calculate V_{xc} and B_{xc} as functional derivatives: $V_{xc} = \frac{\partial E_{xc}(n,\vec{m})}{\partial n}$ and $\vec{B}_{xc} = \frac{\partial E_{xc}(n,\vec{m})}{\partial \vec{m}}$. Within the LDA approach we get: $V_{xc} = \epsilon_{xc}(n, \vec{m}) + n\frac{\partial \epsilon_{xc}(n,\vec{m})}{\partial n}$ and $\vec{B}_{xc} = n\frac{\partial \epsilon_{xc}(n,\vec{m})}{\partial \vec{m}}\hat{m}$ with $\vec{B}_{xc}$ parallel with $\hat{m}$.

Relativistic effects in Wien2k

In Wien2k the relativistic effects are included inside of the muffin-tin atomic spheres where the potential has a spherical symmetry leading to relativistic

equations in a spherical atomic geometry. Therefore, different types of electrons are differently treated, as follows:

(i) *The core electrons* within the atomic sphere region are "fully" relativistic, the core states are fully occupied and obey the spin-compensated Dirac equation in a spherical potential that include the SOC.

$$\left[-\frac{\hbar}{2m_0}\nabla^2 + V_{eff} + \mu_B\vec{\sigma}\cdot\vec{B}_{eff} - \frac{p^4}{8{m_0}^3c^2} - \frac{\hbar^2}{4{m_0}^2c^2}\frac{dV}{dr}\frac{\partial}{\partial\vec{r}} + \frac{1}{2{m_0}^2c^2}\frac{1}{r}\frac{dV}{dr}\left(\vec{l}\cdot\vec{s}\right)\right]\Phi = \varepsilon\Phi$$

First and second term give non-relativistic Schrödinger equation. The third term is a Stoner or Zeeman correction describing the interaction with an external magnetic field. Fourth and fifth terms are mass and Darwin relativistic correction, respectively. The last term corresponds to the spin-orbit coupling (SOC). For spin-polarized potential, spin up and spin down are calculated separately, the density is averaged according to the occupation number. The SOC mixes up and down states, $j = l + s$ is a good quantum number.

(ii) *The valence electrons* inside the atomic muffin-tin spheres are treated with scalar-relativistic approximation. All relativistic effects are included except the SOC that can be further included in «second variation».

(iii) *The valence electrons* belonging to the interstitial region are treated as non-relativistic.

Computational issues

Having in view the extreme sensitivity of the magnetic anisotropy energy to the *k*-space meshing, first, the convergence of the total energy with respect to the total number of *k*-points has been thoroughly performed. Within the total energy approach, using spin-orbit calculation, the perpendicular magnetic anisotropy (PMA) has been calculated as the total energy difference between the configurations where the magnetization was set along perpendicular to the film's plane and in-plane directions. The perturbative formalism of the force theorem approach provides the MAE from the band energies calculated using the fully relativistic charge and spin density of magnetizations corresponding to two distinct directions. Within these formalisms, the electric field (E-field) has been applied using a zig-zag additional potential in the Hamiltonian, as implemented by Stahn et al [13]. Therefore, for different values of electric field, the MAE can be calculated to provide theoretical

insight on its electric field dependence. Quantitatively, the response of the PMA with respect to applied external electric field has been further described in terms of the β coefficient, defined as the slope of the variation of the surface perpendicular anisotropy K_s with the electric field *E*, felt by the ferromagnetic ultrathin film.

Calculation of the Rashba parameter α_R from Wien2k band structure

The spin-orbit term of the non-relativistic Dirac (Pauli) Hamiltonian: $H_{SO} = \frac{\hbar}{(2m_0c)^2}\vec{\nabla}V \cdot (\vec{\sigma} \times \vec{p})$ can be simplified for 2 dimensional electronic systems with the confinement direction (e.g. *Oz* in a Cartesian system) perpendicular to the propagation direction (within the *xOy* plane) leading to the Rashba Hamiltonian: $H_R = \alpha_R \vec{\sigma}(\vec{k} \times \vec{e}_z)$ where $\alpha_R = \frac{\hbar^2}{(2m_0c)^2}\frac{\partial V}{\partial z}$ is the Rashba constant which is a measure of the spin-orbit interaction and $\vec{e}_z$ the unit vector of the *Oz* (electron confinement) direction. From its definition, one can see that α_R is proportional with the electric field $E = -\frac{\partial V}{\partial z}$ aligned along the *Oz* direction. We will see later that in a multilayer stack, at the interface between two different materials, such kind of electric fields naturally exist and lead to Rashba spin-orbit interaction effects. The SO-coupling is exacerbated at the metal surfaces: the breaking of the translational symmetry in surface is equivalent to a potential gradient felt by the electron. In the case when a metal-insulator (or metal semiconductor) interface is created in a multilayer heterostructure, a depletion zone appears with a corresponding significant interfacial electric field. By diagonalizing the Rashba Hamiltonian, the eigenvalues will be:

$$E_{\pm}(k_{II}) = \frac{\hbar^2 k_{II}^2}{2m_0} \pm \alpha_R |k_{II}|$$

representing parabolic bands with an offset of the parabola minimum in positive (or negative) *k* values (Rashba splitting). The minimum of the parabola can be found as $\frac{\partial E}{\partial k} = 0 \Rightarrow k_0 = \frac{m_0 \alpha_R}{\hbar^2}$ so that $E_{\min} = E_0 = \frac{\hbar^2 {k_0}^2}{2m_0}$ that leads to $E_0 = \frac{k_0 \alpha_R}{2}$. From this equation wee see that α_R can be calculated when knowing the values of *E* and *k* corresponding to the minimum of the parabolic dispersion band: $\alpha_R = \frac{2E_0}{k_0}$. As we will see in the section related to results, we have used this equation to extract the Rashba parameter from the Rashba offset of the parabolic bands calculated for different supercell models describing our magnetic multilayer heterostructures. Experimentally, the spin-orbit constant α_R can be extracted from ARPES (Angular Resolved Photoemission) [14,15].

Atomistic calculations

The results issued from the ab-initio calculations, e.g., atom projected magnetic moments, PMA, DMI, have been used as input parameters for atomistic calculations performed within the framework of the atomistic code *VAMPIRE* [16]. The main input files for running the atomistic code contain information about materials and properties that enter in the sample composition: sandwiches of magnetic or nonmagnetic materials, alloys, etc. and system configurations: dimensions, simulation described in detail with all the necessary parameters (atomic positions with the exchange matrix components and type of exchange (isotropic, vectorial, tensorial). Within the atomistic magnetic calculation approach implemented in *VAMPIRE* the atoms have been considered as individual interacting entities with a given magnetic moment. Similarly to the macroscopic LLG approach, the spin dynamics is obtained by integrating the Landau–Lifshitz-Gilbert (LLG) equation applied at the atomistic level for the atomic spins. Here, the atomistic LLG equation:

$$\frac{\partial \vec{\boldsymbol{S}}_i}{\partial t} = -\frac{\gamma}{(1+\lambda^2)}\left[\vec{\boldsymbol{S}}_i \times \vec{H}^i_{eff} + \lambda \vec{\boldsymbol{S}}_i \times (\vec{\boldsymbol{S}}_i \times \vec{H}^i_{eff})\right]$$

describes the interaction of an atomic spin moment $\vec{\boldsymbol{S}}_i$ with an effective magnetic field $\vec{H}^i_{eff}$ of each spin *i* derived from the complete spin Hamiltonian $\mathcal{H}$ including all the interaction and anisotropy terms describing the modeled system (e.g., exchange, anisotropy, Zeeman interaction with external applied fields):

$$\mathcal{H} = \mathcal{H}_{exc} + \mathcal{H}_{ani} + \mathcal{H}_{app}; \qquad \vec{H}^i_{eff} = -\frac{1}{\mu_S}\frac{\partial \mathcal{H}}{\partial \vec{\boldsymbol{S}}_i}$$

where μ_S is the local spin moment, γ is the absolute value of the gyromagnetic ratio, λ the microscopic Gilbert damping parameter. The effect of the temperature has been included using the Langevin dynamics [17] assuming that the thermal fluctuations on each atomic site can be represented by a Gaussian white noise term $\Gamma(t)$ whose width is proportional with the temperature value. The corresponding thermal field will be: $H^i_{th} = \Gamma(t)\sqrt{\frac{2\lambda k_B T}{\gamma \mu_S \Delta T}}$, where k_B is the Boltzmann constant and *T* is the temperature of the system. To determine the time dynamics of systems of spins, the stochastic LLG equation is solved numerically (integrated) within the Heun predictor corrector scheme.

In this paper, the simulations have been performed for cylindrical Au/Fe/MgO multilayer nanostructures with a diameter of 15 nm (the integration range of the LLG equations). Periodic boundary conditions (PBC) have been included to calculate magnetic properties of macroscopically large magnetic heterostructure systems. As input for the *VAMPIRE* code, we have used thickness dependent PMA and atom resolved magnetic moments extracted from *Wien2k* ab-initio calculations performed on super-cell models describing the realistic Au/Fe/MgO(001) systems with variable Fe thicknesses.

RESULTS AND DISCUSSION

Ab-initio calculations

A typical supercell model used in our ab-initio calculations is depicted in fig. 1. As we mentioned, in the calculation the electric field can be introduced via a zig-zag potential term in the Hamiltonian. Following the zig-zag potential E-field implementation within the Wien2k code by Stahn et al [13], the supercell contains the multilayer sequence in half of its volume, the other half being a vacuum region. Therefore, a constant *E*-field equal to $-\Delta V/\Delta z$ will be localized at the Fe/MgO interface, the amplitude and sign of the electric field being driven by the *V* ramp amplitude and the choice of an ascending or descending *V* ramp in that region. The *k*-space mesh used in our calculation was $25\times25\times1$, which resulted from a preliminary study of the total energy convergence with respect to the total number of *k*-points in the Brillouin zone. Having in view the sensitivity of the MAE to energy development parameters in *Wien2k*, especially when including relativistic local orbitals (LAPW+l_0), we set E_{max}=100, meaning that all scalar relativistic eigenstates are included when the spin-orbit-coupling is switched on. The size of the basis set used in the expansion of the wave function was $R \cdot K_{max}$=7, where *R* is the smallest atomic muffin-tin sphere radius, R_{MT}, times the largest *K*-vector, K_{max}.

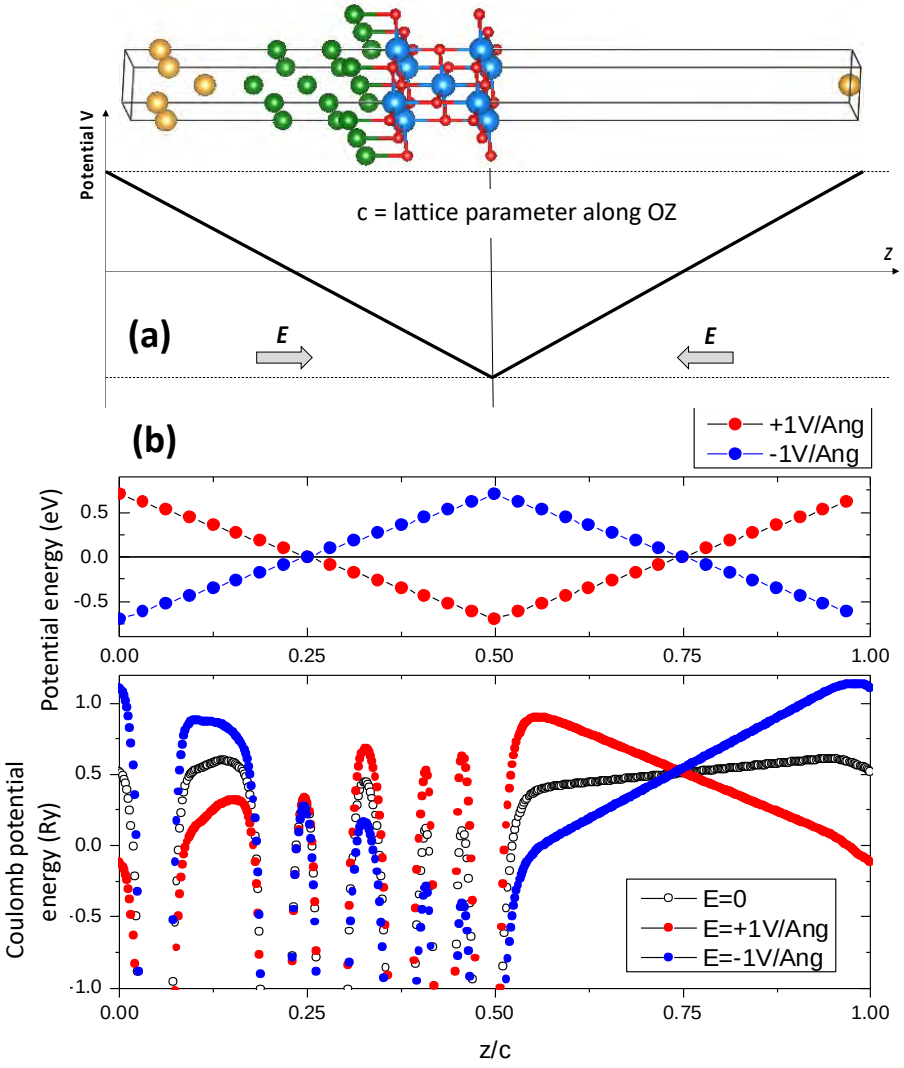

Fig. 1. (a) Supercell model used to describe the *X*/Fe/MgO(001) system; here the thickness of Fe is 5 monolayers (ML). Zig-zag potential leading to a constant $\vec{E} = -\nabla V = -\frac{dV}{dz}\vec{e}_z$ in the half of the supercell where the *X*/MgO interface is placed. The sign of the applied electric field is determined by the sign of the chosen ramp slope; (b) Potential energy corresponding to the ramp potential and self-consistently calculated Coulomb potential on each atom in the supercell.

Having in view the complexity of the problem, the computational tasks have been performed within a *k*-point parallelization scheme using a 48-CPU workstation. From the ab-initio calculations, for various *X*/Fe/MgO configurations, we obtained the following main results, synthetized in table 1:

Table 1. Calculated magnetic anisotropy energy (MAE) for various multilayer heterostructure systems in which the ultrathin Fe is sandwiched between *X* and MgO with *X* = V, Au, Pd, Ag, MgO, Pt. The number represents the # of monolayers. The slope of the MCA variation with applied electric field is β. We also indicate the lattice parameters used in the ab-initio calculations.

System	MAE (V=0) E_{perp}-E_{plan}	MAE (V=0)	β	a=b	Crystallographic phase
	meV	erg/cm^2= mJ/m^2	fJ/Vm	Å	
V3/Fe5/MgO-vid	0.54	0.94	68.44	3.02996	cubic (100)
Au3/Fe5/MgO-vid	0.71	1.37	-32.26	2.883162	cubic (100)
Au3/Fe5-Pt1/MgO-vid	5.86	11.28	-56.65	2.883162	cubic (100)
Pd3/Fe5/MgO-vid	0.43	0.83	17.3	2.883162	cubic (100)
Pd3/Fe5-Pt1/MgO-vid	5.13	9.87	87.46	2.883162	cubic (100)
Ag3/Fe5/MgO-vid	1.35	2.59	-	2.888263	cubic (100)
MgO/Fe3-MgO-vid	1.91	3.71	-	2.8689	cubic (100)
Pt3/Co5/MgO-ot-aPt-vid	0.23	0.58	-43.43	2.7709	hexa (111)

(i) The calculated systems mostly present perpendicular magnetic anisotropy, i.e., the most stable configuration corresponds to the magnetization being aligned along the *z*-direction. However, for some systems: Cr3/Fe5/MgO(001), Pt3(001)/Fe5/MgO, Pt3(111)/Co5/MgO, the ground state corresponds to a configuration in which the magnetization lies in-plane.

(ii) The perpendicular anisotropy can be significantly enhanced if one monolayer of Pt is inserted at the top interface, between Fe and MgO. Moreover, the adjunction of the top Pt layer changes the response of the PMA with respect to an external applied electric field.

(iii) The electric field response of the PMA is specific for each system. One can tailor the amplitude and the sign of the variation by changing the chemical nature of the bottom interface *X*/Fe (fig. 2).

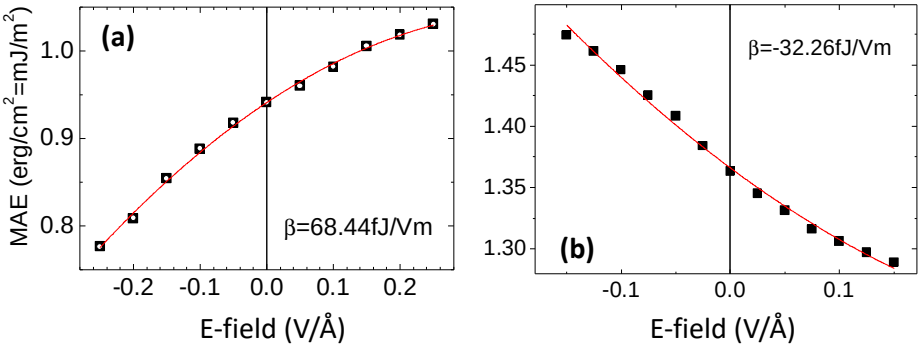

Fig. 2. Magnetic anisotropy energy dependence on electric field (E-field) for (a) V3/Fe5/MgO and (b) Au3/Fe5/MgO systems. Open circles in (a) correspond to Force theorem, black squares to total energy MAE calculations. The sign of the variation slope is different, indicating the significant role of the bottom *X*/Fe interface (*X*=V, Au) on the PMA and its field variation.

The opposite sign variation of the PMA with the E-field can be explained by considering the Rashba field at the bottom *X*/Fe interface whose sign depends on the relative work-functions of Fe and *X* metals (see fig. 3), as theoretically predicted by Barnes et al [9]. The effect of an external electric field on the intrinsic fields $E_1 = E_T$ ($E_2 = E_B$) at the top (bottom) interfaces is illustrated in fig. 4, the analysis being performed for Au/Fe/MgO system.

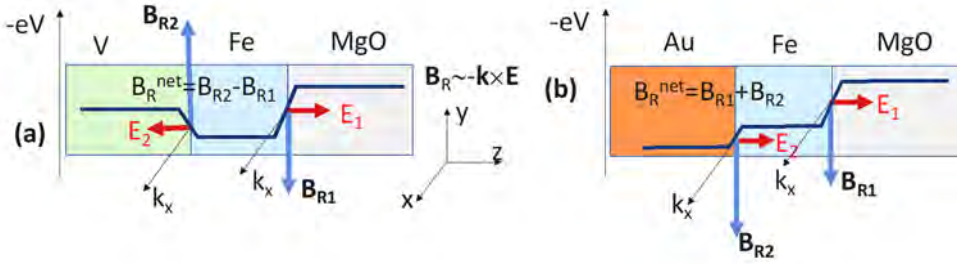

Fig. 3. Potential profiles, Rashba fields B_R related to the intrinsic electric fields at the top (1)=Fe/MgO and the bottom (2)=*X*/MgO interfaces in (a) V3/Fe5/MgO and (b) Au3/Fe5/MgO systems. In (a), $E_{ext} < 0$ decreases E_1 (so B_{R1}) => B_R^{net} (and α) increases. In (b) $E_{ext} < 0$ decreases E_1 (so B_{R1}) => B_R^{net} (and α) decreases.

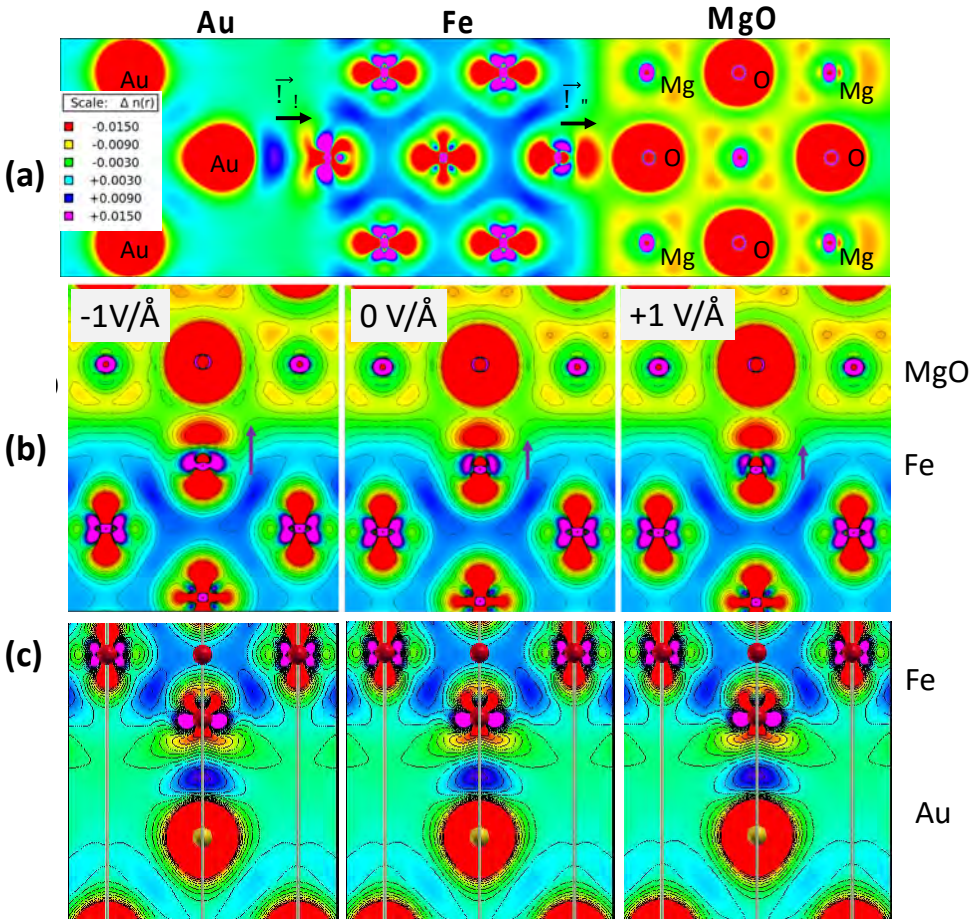

Fig. 4. Valence charge density plots for the Au3/Fe5/MgO stack: (a) complete stack, (b) zoom at the top Fe/MgO and (c) bottom Au/MgO interfaces illustrating the effect of an external electric field on the interface intrinsic fields E_1 (top) and E_2 (bottom).

As expected, we clearly illustrate that the external electric field only influences the top interface, being completely screened at the metallic bottom Au/Fe interface (no field effect observed, fig. 4(c)). The variation of the electric field E_1 at the top interface Fe/MgO when an external field is applied can be directly correlated to the charge and magnetic moment variation for the interface Fe(/MgO) atom, issued from the ab-initio calculation and illustrated in fig. 5. We see from the analysis depicted in fig. 5 that a positive external electric field increases the charge

on the interface Fe atom (the depletion decreases) and this corresponds to a decrease of the Fe magnetic moment, as expected for its "roughly" $3d^6$ configuration. From the Rashba splitting of the band structure corresponding to opposite orientations of the magnetization with respect to the crystallographic axes (directions with **k**⊥**M**) we calculated the Rashba parameter α_R (see fig. 6): $\alpha_R = \frac{2E_0}{k_0}$ where E_0 corresponds to the minimum of the parabolic dispersion and k_0 the corresponding wave vector where *E(k)* has a local minimum.

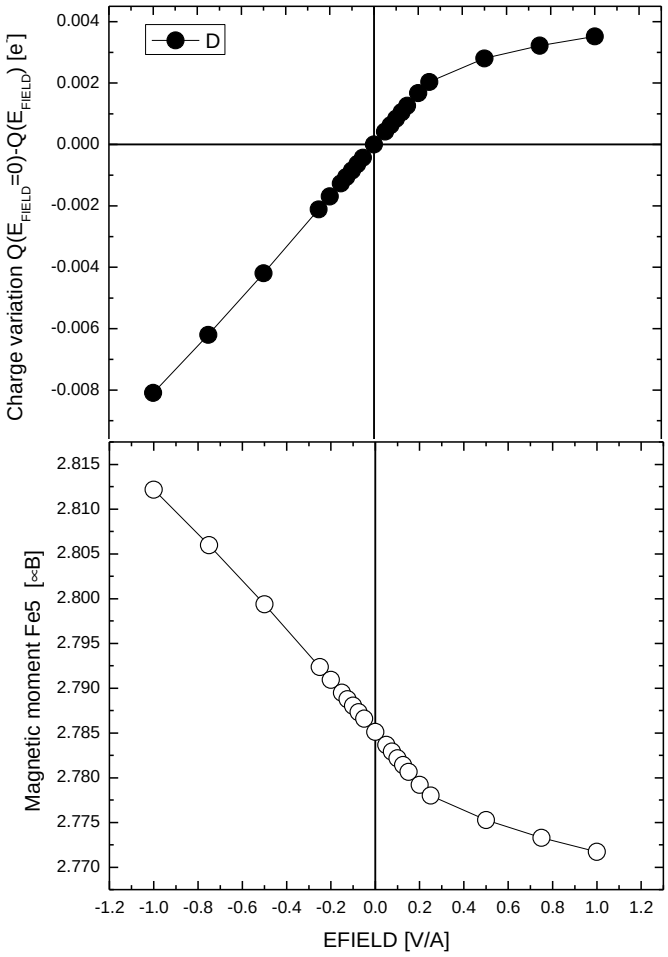

Fig. 5. Charge variation within the muffin-tin sphere of the interface Fe(/MgO) atom (top panel) and corresponding magnetic moment with respect to the external applied electric field (Volt/Angstrom units).

In this way, we demonstrate that opposite sign Rashba parameters can be obtained in V/Fe/MgO and Au/Fe/MgO systems, corresponding to opposite Rashba offset in *k* of the surface Fe parabolic bands in the *X*/Fe/MgO stack, where *X*=V and Au (fig. 6). While the top interface Fe/MgO is identical in the two configurations, it is obvious that the opposite offset sign is related to the bottom interface, demonstrating the major influence of the Rashba fields at both top and bottom interfaces on the PMA and the net α_R.

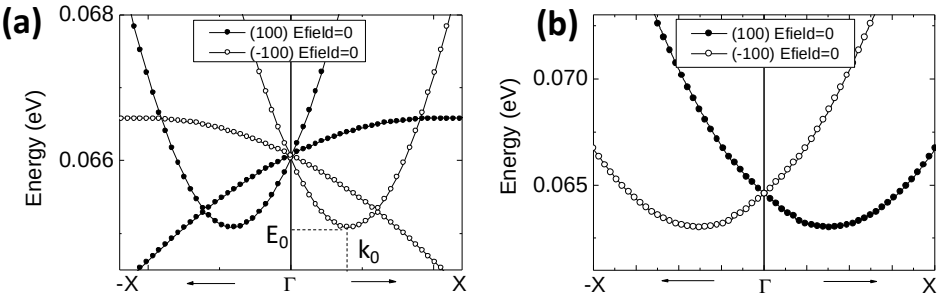

Fig. 6. Parabolic band dispersion of surface bands of Fe in *X*/Fe5ML/MgO system, where *X*=V (a) and X=Au (b). The bands corresponding to the magnetization *M* parallel to (100) and (-100) are oppositely shifted in *k* due to the net Rashba field whose sign is determined by both bottom *X*/Fe and top Fe/MgO interfaces (see explanation related to fig. 3). $E_{\min} = E_0 = \frac{\hbar^2 {k_0}^2}{2m_0}$.

This illustrates that the bottom interface Rashba magnetic field B_{R2} has a long-range influence and, by its sign and amplitude, can modulate the net Rashba field in the stack (see fig. 3).

(iv) Within the framework of a still under debate issue in the literature, in which the asymmetric exchange Dzyaloshinskii-Moriya interaction can be triggered by a Rashba mechanism [18], we calculated the DMI constant from the Rashba splitting and the Rashba constant α_R: $DMI = 2k_R A$, where *A* is the Fe exchange stiffness (21 pJ/m [19]), $k_R[\text{Å}^{-1}] = 0.2619 * \alpha_R[eV\text{Å}]\, m_e$, m_e is the effective mass of the electrons in Fe, estimated to be equal to 0.57 from the fit of the parabolic bands illustrated in fig. 6(b) - corresponding to Au/Fe/MgO system. Using this algorithm, we calculated, explained and correlated the sign, the magnitude and the electric field dependence of the PMA, the Rashba coefficient α_R and the Dzyaloshinskii–Moriya (DMI) asymmetric exchange interaction parameter in different *X*/Fe/MgO(001) systems (see example in fig. 7 for Au/Fe/MgO system). It is important to mention

that the sign of the DMI, correlated to the sign of the Rashba parameter, has a significant importance in magnetic heterostructures: It determines the topological charge of chiral structures (domain walls and skyrmions) and the direction of their velocity when manipulated by spin transfer torques related to spin currents in emerging generation of race-track memories [20, 21]. Therefore, a major issue of our calculations is related to the prediction of an original strategy for the DMI sign, amplitude, and E-field control via the interface engineering in experimental magnetic multilayered stacks.

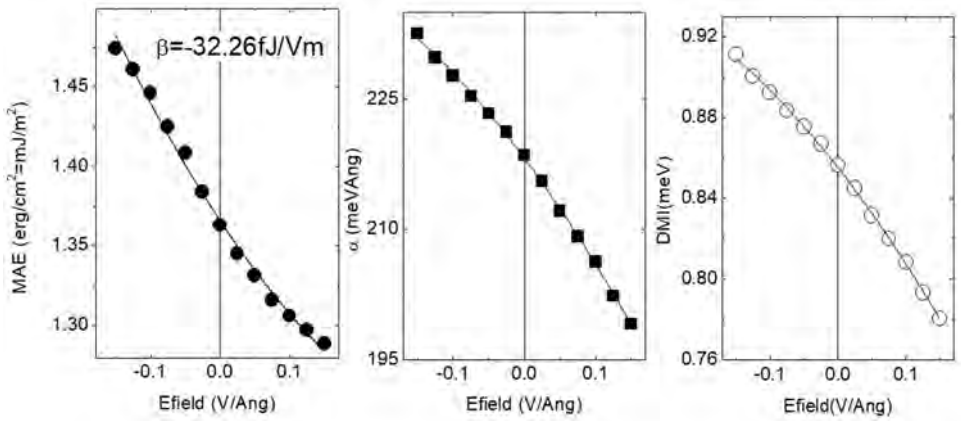

Fig. 7. Typical curves of electric field dependence of PMA, α_R and DMI in the Au/Fe(5ML)/MgO system.

(v) When varying the Fe thickness in X/Fe/MgO(001) systems, with *X*=V, Cr, Au, we observe clear oscillations of PMA with the number of the Fe monolayers (fig. 8).

We explained these oscillations within the framework of quantum wells of the Δ_1 Bloch symmetry Fe electrons, as we previously demonstrated in spin dependent transport experiments in Fe/Cr/Fe/MgO single crystal MTJs [22], where similar quantum well effects and oscillation period of the tunnel conductance has been observed. The predicted PMA oscillations with the ferromagnetic layer thickness represent a major issue for understanding the PMA and the DMI in realistic experimental system with sizable roughness and thickness fluctuations, even at an atomic level. In a first step, in this work, we performed atomistic micromagnetic calculations of magnetic properties (hysteresis curves) of Au/Fe(*t*)/MgO nanostructures with a variable thickness *t* = 3, 4, 5 ML both at 0 K and room temperature.

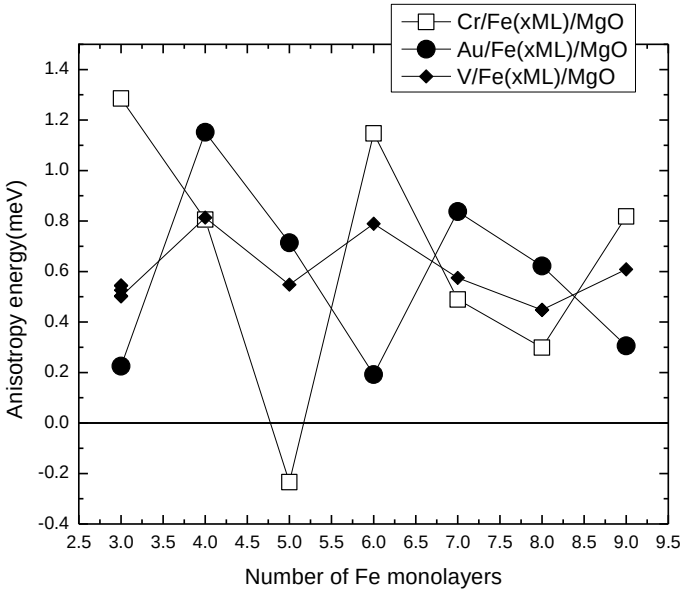

Fig. 8. Magnetic anisotropy energy for X/Fe/MgO(001) slabs where *X*=Cr(001), Au(001), V(001), extracted from ab-initio calculations. Positive (negative) MAE correspond to perpendicular (in-plane) magnetization (PMA) configurations.

Atomistic simulations for Au/Fe/MgO system modelled as flat terraces

In order to extend the theoretical analysis of the Au/Fe/MgO system to larger dimensions, we chose to simulate a layered structure in the atomistic framework. Following this approach, we can represent with high fidelity the case of MBE terraces and, in addition, we can benefit from the time and resources efficiency that this numerical tool provides us with.

Three samples were modelled as flat slabs of constant thickness, with periodic boundary conditions – Table 2. The hysteresis loops have been simulated with a field applied along the *Oz* direction. By doing so, we avoid the well-known computational expenses of working with a tremendously large number of dipole field cubic macrocells, but we can still use the smallest macrocell size for a high precision dipole field calculation. The input parameters such as the layer resolved magnetic moments per atom and anisotropy constants were obtained from the first principles method. A convergence study at T = 0 K was performed in order to establish the suitable simulation parameters of the hysteresis loops, in agreement with the Stoner-Wohlfarth model.

For *T*=0 K, without considering the dipole field, all of the samples display rectangular hysteresis loops with coercivities in perfect agreement with the Stoner Wohlfarth model, as represented in Table 2. If we add the dipole field to our model, only the 4ML and 5ML samples preserve their coercivity, as the 3ML sample magnetization becomes tilted in-plane. It can be observed that the coercive field varies with the thickness in a similar fashion as the anisotropy energy. Also, it is worth mentioning that the rectangular shape of the hysteresis loops is the evidence of a perpendicular magnetization orientation. This is a numerical confirmation that can be verified experimentally in a range of ultra-low temperatures, where the effect of thermal fluctuations is diminished.

Table 2. Coercive field values determined analytically and from atomistic simulations at 0 K for the investigated samples.

Sample name/ no. atomic layers	**Thickness (nm)**	**Hc Stoner-Wohlfarth (*T*=0K) limit (T)**	**Hc atomistic with dipole field (*T*=0 K) (T)**
3ML / 3 atomic layers	0.429	0.99	In-plane oriented
4ML/ 4 atomic layers	0.572	3.88	1.76
5ML/ 5 atomic layers	0.715	1.95	0.10

When thermal fluctuations are added to the system, the dipolar and the thermal field compete with the anisotropy and in some situations, they will tilt the magnetization orientation from an out-of-plane to an in-plane configuration. Such a case is depicted in fig. 9, where hysteresis loops simulated at room temperature for different sample thicknesses are shown. At *T* = 300 K one can observe that the perpendicular magnetic anisotropy is strongly dependent on the thickness. For 3ML and 5ML it can be observed that the magnetization adopts an in-plane orientation, while for the 4ML thickness it is oriented perpendicular to the film plane. The effect of the thermal fluctuations can be observed in the coercivity.

The addition of the dipole field leads to lower coercive field values compared to the ones predicted by the Stoner-Wohlfarth model. Also, the thermal fluctuations have been observed to contribute to this effect. We mention that the magnetic behavior illustrated in fig. 9 follows the variation of the PMA with the thickness issued from the ab-initio calculations (see fig. 8) where a local maximum in PMA was found for 4ML of Fe.

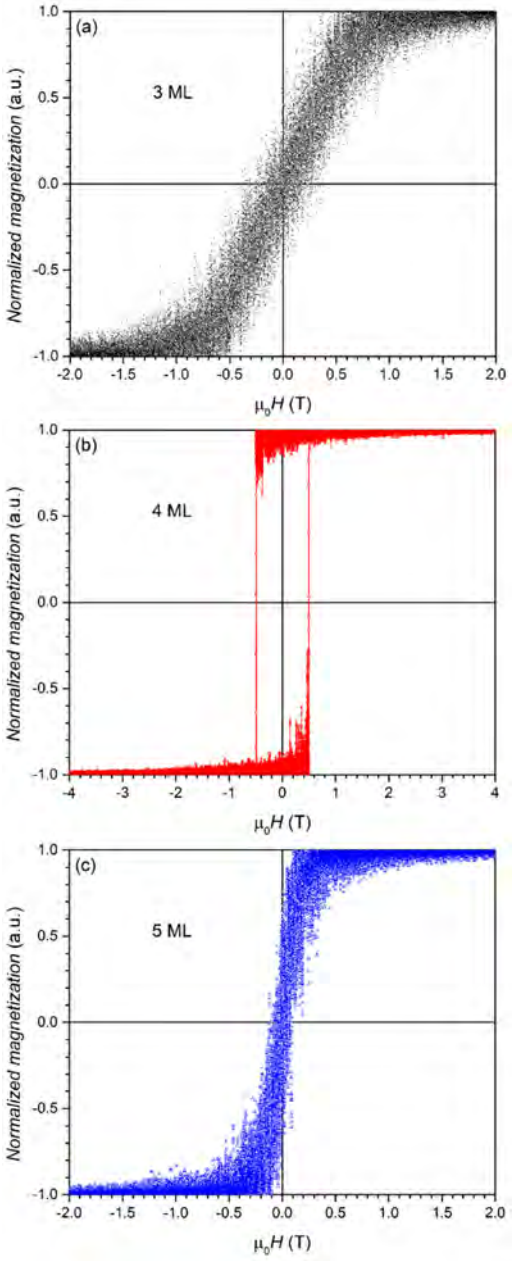

Fig. 9. Hysteresis loops at *T*=300 K obtained from atomistic simulations: (a) 3ML; (b) 4ML; (c) 5ML.

The results of our atomistic magnetic simulation indicate that to design experimental devices based on the Au/Fe/MgO system suitable for room temperature applications related to PMA one must optimize the deposition process to obtain a ferromagnetic thickness around 4ML (0.572 nm). A further coming study will consider the effect of thickness fluctuation to approach the realistic situation of experimental samples.

CONCLUSIONS

Using ab-initio calculations we have investigated some major mechanisms related to the perpendicular magnetic anisotropy and its variation with external magnetic fields. Our calculation addresses multilayer stacks with ultrathin ferromagnetic layers sandwiched between a bottom non-magnetic metal and a top MgO insulator, as commonly found in magnetic tunnel junction architectures. We point out the major contribution of the Rashba mechanism, related to interfacial intrinsic electric fields, on both PMA and DMI and underline the possibility to tailor these properties via some interfacial engineering. In this way one can tune the magnitude and the voltage response of the PMA and the sign and the magnitude of the DMI, major requests in storage and synaptic devices based on magnetic chiral structures (domain walls and skyrmions). Oscillations of the PMA with the thickness of the ferromagnetic materials have been also predicted and correlated to quantum well effects already observed by our team in spin polarized transport in Cr/Fe/MgO/Fe magnetic tunnel junctions. Finally, using atomistic magnetic simulations we have calculated macroscopic magnetic properties in Au/Fe/MgO nanostructures as a first step towards the understanding of magnetic characteristics of realistic experimental system with sizable roughness and thickness fluctuations, even at atomic level.

ACKNOWLEDGEMENTS

C.T. acknowledges funding from the project «MODESKY» ID PN-III-P4-ID-PCE-2020-0230, No. UEFISCDI:PCE 4/04.01.2021 and is grateful to M. Chshiev for fruitful discussions about PMA and the E-field manipulation anatomy. Moreover, the implementation of the current research further confirms and sustains the durability of previous funding projects: «SPINTRONIC» POS CCE Project: ID. 574, cod SMIS-CSNR 12467, «SPINTAIL» ID PN-II-PCE-2012-4-0315, No. UEFISCDI:23/29.08.2013 and «EMERSPIN» ID PN-III-P4-ID-PCE-2016-0143, No. UEFISCDI:22/12.07.2017.

REFERENCES

1. B. Dieny, M. Chshiev, *Rev. of Mod. Phys.,* vol. 89, (2017).
2. D. C. M. Yamanouchi, F. Matsukura, H. Ohno, *Science*, 301, 943-945 (2003).
3. S. Kanai, F. Matsukura, H. Ohno, *Appl. Phys. Lett.*, 108, 192406 (2016).
4. C. Grezes, F. Ebrahimi, J. G. Alzate, X. Cai, J. A. Katine, J. Langer, B. Ocker, P. Khalili Amiri, K. L. Wang, *Appl. Phys. Lett.,* 108, 012403 (2016).
5. E. G. V. Krizakova, G. Sala, F. Yasin, S. Couet, G. S. Kar, K. Garello, P. Gambardella, *Nature Nanotechnology*, 15, 111 (2020).
6. M. K. Niranjan, C-G. Duan, S. S. Jaswal, E. Y. Tsymbal, *Appl. Phys. Lett.,* 96, 222504 (2010).
7. K. H. He, J. S. Chen, Y. P. Feng, *Appl. Phys. Lett.*, 99, 072503 (2011).
8. F. Ibrahim, H. Yang, A. Halla, M. Chshiev, *Phys. Rev. B*, 93, 014429 (2016).
9. S. E. Barnes, J. Ieda, S. Maekawa, *Sci. Rep.*, 4, 4105 (2015).
10. T. Srivastava, M. Schott, R. Juge, V. Křižáková, M. Belmeguenai, Y. Roussigné, A. Bernand-Mantel, L. Ranno, S. Pizzini, S-M. Chérif, A. Stashkevich, S. Auffret, O. Boulle, G. Gaudin, M. Chshiev, C. Baraduc, H. Béa, *Nano Lett.*, 18, 4871 (2018).
11. P. Blaha, K. Schwarz, F. Tran, R. Laskowski, G. K. H. Madsen, L. D. Marks, *J. Chem. Phys*., 152, 074101 (2020).
12. X. Wang, D-S. Wang, R. Wu, A.J. Freeman, *J. Magn. Magn. Mater.*, 159, 337 (1996).
13. J. Stahn, U. Pietsch, P. Blaha, and K. Schwarz, *Phys. Rev. B*, 63, 165205, (2001).
14. G. Nicolay, F. Reinert, S. Hufner, P. Blaha, *Phys. Rev. B,* 65, 033407 (2002);
15. F. Reinert, G. Nicolay, S. Schmidt, D. Ehm, S. Hufner, *Phys. Rev. B* 63, 115415 (2001).
16. R. F. L. Evans, W. J. Fan, P. Chureemart, T. A. Ostler, M. O. A. Ellis, R. W. Chantrell, *J. Phys.: Condens. Matter*, 26, 103202 (2014).
17. W.F. Brown Jr, *IEEE Trans. Magn.* 15, 1196 (1979).
18. H. Yang, O. Boulle, V. Cros, A. Fert, M. Chshiev, *Sci. Rep.*, 8, 12326 (2018).
19. C. Antoniak, J. Lindner, K. Fauth, J.-U. Thiele, J. Minár, S. Mankovsky, H. Ebert, H. Wende, M. Farle, *Phys. Rev. B*, 82, 064403 (2010).
20. S. S. P. Parkin, M. Hayashi, L. Thomas, *Science,* 320, 190 (2008).
21. J. Sampaio, V. Cros, S. Rohart, A. Thiaville, and A. Fert, *Nat. Nanotechnol.,* 8, 839 (2013).
22. F. Greullet, C. Tiusan, F. Montaigne, M. Hehn, D. Halley, O. Bengone, M. Bowen, and W. Weber, *Phys. Rev. Let.* 99, 187202, (2007).

STUDIA UBB PHYSICA, Vol. 66 (LXVI), 1-2, 2021, pp. 111-120
(RECOMMENDED CITATION)
doi:10.24193/subbphys.2021.10

THE NATURE OF Mn-Mn COUPLING IN Mn-Ni-Al ALLOYS

V. REDNIC[1*], M. COLDEA[2], V. POP[2], M. NEUMANN[3]

ABSTRACT. The occurrence of ferro - and antiferromagnetism in Mn-Ni-Al alloys is governed by the sign of the direct exchange interaction between the Mn magnetic ions. Experimentally has been found that, if the separation between the Mn magnetic ions is greater than the critical value d_{cr}= 2.91 Å, they are ferromagnetic and if the distance is less than the critical value, they are antiferromagnetic. The value of Mn local magnetic moment depends on the number of Al atoms in the first vicinity but the dominant factor is the Mn-Al distance. The nature of Mn-Mn exchange coupling was studied through X-ray diffraction, magnetic and XPS measurements.

Keywords: *exchange coupling, local magnetic moments, crystallographic structure, electronic structure*

INTRODUCTION

The problem of local moments confined to the transition 3d metals (T) sites, i.e., localized behaviour in some aspects of itinerant electrons, is one of the most important issues in the physics of the magnetic alloys and intermetallic compounds [1]. The condition for the existence of the local moment at the T site is $\pi\Delta / U < 1$, where Δ is the width of the d states and U is the Coulomb correlation energy between d electrons [2]. The occurrence of ferro and antiferromagnetism in alloys and intermetallic compounds of 3d metals Mn, Cr, Fe is governed by the sign of the direct exchange interaction between the magnetic ions. Experimentally has been found that, in general, if the separation between the magnetic ions is greater than a critical value d_{cr}, they are ferromagnetic and if the distance is less

[1] *National Institute for Research and Development of Isotopic and Molecular Technologies, P.O. Box 700, 400293 Cluj-Napoca, Romania*
[2] *Babes-Bolyai University, Faculty of Physics, Kogalniceanu 1, 400084 Cluj-Napoca, Romania*
[3] *University of Osnabrück, Fachbereich Physik, 49069 Osnabrück, Germany*
* *Corresponding author: vasile.rednic@itim-cj.ro*

than the critical value, they are antiferromagnetic. In general, the Mn alloys and intermetallic compounds are antiferromagnetic when the distance between the Mn atoms d_{Mn-Mn} is less than 2.9 Å [3]. Experimentally, the critical Mn-Mn distance of 2.83 Å has been estimated in NiAs-type Mn compounds [3,4]. On the other hand, the magnetic τ-phase of MnAl alloy shows ferromagnetism at a high Curie temperature despite the very short Mn-Mn distance of 2.77 Å [5]. This, the so-called Mn dilemma, is based on the simple Bethe-Slater picture of direct exchange coupling between magnetic atoms [6, 7]. It was found that super-exchange interaction between Mn atoms via p-electrons of Al atoms causes antiferromagnetism in MnAl τ-phase. The ferromagnetism in this system results from the suppression of the super-exchange interaction due to the substitution of excess Mn atoms for the Al atoms, so the Mn-Mn distance does not strongly affect the magnetism in this alloy [5].

In the phase diagram of Mn-Ni-Al ternary system there are many domains of solid solution [8]. Maintaining constant the concentration of one element, one can varies the concentration of the other two elements. In this case are changing the crystalline structure, the number of near- neighbours atoms with d-orbitals, the vicinity of Mn atoms, the distances between the Mn atoms and implicitly the strength and the sign of the interaction between the neighbouring local moments.

The aim of this paper is to study, through X-ray diffraction, magnetic and XPS measurements, the nature of Mn-Mn exchange in the Mn-Ni-Al alloys.

EXPERIMENTAL

The investigated alloys were prepared by the argon arc melting method. The samples were melted repeatedly (at least four times) in the same atmosphere to ensure homogeneity. The weight loss of the final furnace-cooled samples was found to be less than 1%. The purity of starting materials was 99.999% for Al and 99.99% for Mn and Ni. XRD measurements were performed on polished surfaces using a Bruker D8 Advance diffractometer, due to the hardness of the samples. The magnetic measurements were performed using a vibrating sample magnetometer (VSM) in the temperature range 4– 850 K and fields up to 10 T. The XPS spectra were recorded using a PHI 5600ci ESCA spectrometer with monochromatized Al Kα radiation at room temperature. The pressure in the ultra-high vacuum chamber was in the 10^{-10} mbar range during the measurements. The samples were cleaved in situ and the surface cleanness was checked by monitoring the O 1s and C 1s core levels in the survey spectra.

RESULTS AND DISCUSSIONS

The nature of Mn-Mn exchange coupling is described by two main characteristics namely, the sign and the strength of the exchange coupling. The sign of the exchange coupling is mostly given by the Mn-Mn distance, while the strength depends on the number and type of the surrounding atoms as well as the distance between them.

The sign of Mn-Mn exchange coupling

One of the most representative system where the influence of Mn-Mn critical distance can be observed is **$Ni_{1-x}Mn_xAl$**. The electronic structure and magnetic properties of $Ni_{1-x}Mn_xAl$ (x=0, 0.2, 0.3, 0.4, 0.5, 0.6, 0.8) were presented [9]. X-ray diffraction patterns show that all the alloys are single phases with the same CsCl (B2) structure type. In the elementary cell Al atoms occupies the 1a position while Mn and Ni atoms occupy the 1b position (see figure 1). When two Mn atoms are situated in the centre of two neighbouring elementary cells, the shorter Mn-Mn distance is equal to the lattice parameter. In this system the lattice parameter is close to the critical Mn-Mn distance (~2.9 Å). Furthermore, the lattice parameter (see figure 1) increases monotonically with Mn concentration from a=2.875 Å for NiAl to a=2.966 Å for $Ni_{0.2}Mn_{0.8}Al$.

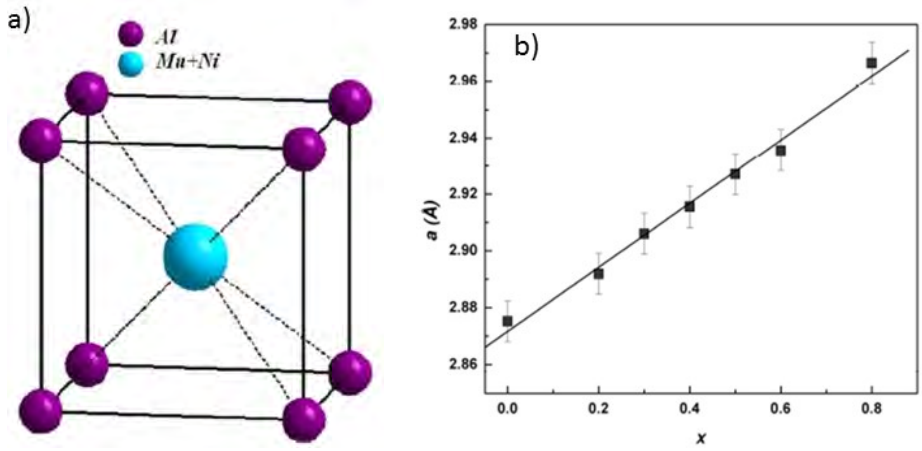

Fig. 1. Elementary cell representation (a) and lattice parameter variation as a function of Mn content (b) in $Ni_{1-x}Mn_xAl$ alloys.

The temperature dependence of the spontaneous magnetization, presented in figure 2, shows a ferromagnetic behaviour of the investigated alloys. Nevertheless, a small anomaly in the magnetization of the ferromagnetic component can be observed at low Mn concentration (x = 0.2 and 0.3). This anomaly, known as "pinning effect", comes from the exchange interaction at the interfaces of an antiferromagnetic and a ferromagnetic entity, and proves the formation of Mn-Mn antiferromagnetic pairs.

At low Mn concentration the lattice parameter is smaller than the critical distance favouring the formation of Mn-Mn antiferromagnetic pairs, but in the same time, at small Mn concertation there is a smaller probability to have two Mn atoms in the centre of two neighbouring cells. This explains the ferromagnetic behaviour of these alloys and also the presence of a small antiferromagnetic phase.

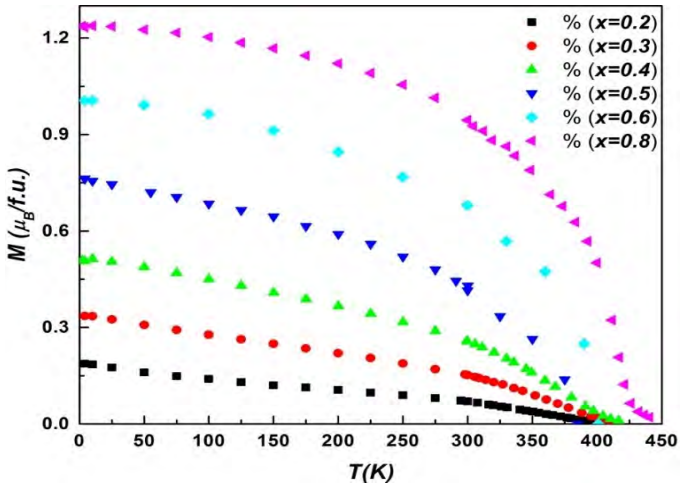

Fig. 2. Temperature dependence of spontaneous magnetization of $Ni_{1-x}Mn_xAl$ alloys. [9]

Once the Mn concentration increases, the probability of having two Mn atoms in the centre of two neighbour cell increases, suggesting an increase in the number of antiferromagnetic Mn-Mn pairs. The experimental results show that the antiferromagnetic component is barely visible for x=0.4 and disappears for higher Mn concentration. This can be explained by the increase of the lattice parameter, and consequently the Mn-Mn distance, at values above 2.9 Å. This means that even if there are two Mn atoms in centre of two neighbour cells, the distance between them is higher that the critical distance and consequently the exchange coupling is ferromagnetic.

The "pinning" effect was also observed in **$Mn_{1-x}Al_xNi$ alloys** [10], where a coexistence of antiferromagnetism (B2 phase) and ferromagnetism ($L2_1$ phase) was observed for $0.6 \leq x < 1$ alloys. The B2 phase has the same structure with the $L2_1$

phase of Heusler alloys, having the unit cell equals with the 8-th part from the last one (see figure 3). In the $L2_1$ structure, where the Mn atoms are separated by Al atoms, the shortest Mn-Mn distance is about 4.1Å, while in B2 phase the Mn and Al atoms are randomly arranged, thus the near-neighbour Mn–Mn distance is about 2.9 Å.

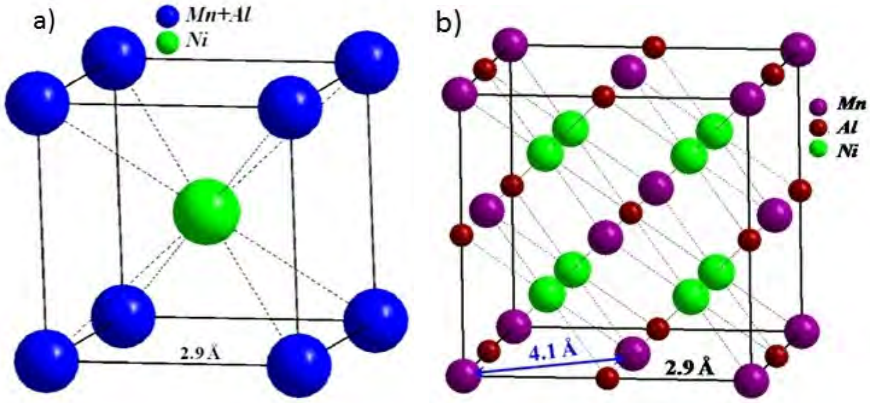

Fig. 3. Representation of ClCs (a) and Heusler (b) structure type.

In order to determine the ferromagnetic (FM) and antiferromagnetic (AFM) contributions to the measured magnetization and to estimate the corresponding Curie and Néel temperatures T_C and respectively T_N, we have used the Honda-Arrot plot for each temperature, according to the relation [11]:

$$\chi_m = \chi_{AFM} + M_{FM}/H \quad (1)$$

where χ_m is the measured susceptibility, χ_{AFM} the susceptibility of the antiferromagnetic component, M_{FM} the saturation magnetization of the ferromagnetic component and H the applied magnetic field. A linear dependence of χ_m versus H^{-1} in higher magnetic fields was evidenced for each temperature, showing that in the studied field range, saturation has been obtained. In figure 4 are shown the temperature dependence of the as determined susceptibility χ_{AFM} and magnetization M_{FM}, respectively. The curves $\chi_{AFM}(T)$ present a downward at certain temperatures, referred as the Néel temperatures.

The Mn-Mn exchange coupling depending on Mn-Mn distance was also evidenced in **$Ni_{0.7-x}Al_xMn_{0.3}$ alloys**. The crystallographic and electronic structure of $Ni_{0.7-x}Al_xMn_{0.3}$ alloys were presented [12]. The $Ni_{0.7-x}Al_xMn_{0.3}$ (x=0.3, 0.4 and 0.5) alloys are single phase having CsCl (B2) structure type. The lattice parameter varies from 2.9 Å for x=0.3 to 2.94 A for x=0.5. The lattice parameter and implicit the Mn-Mn atomic distance is just in the region of Mn-Mn critical distance and the effect on magnetic properties are significant as it can be seen in figure 5.

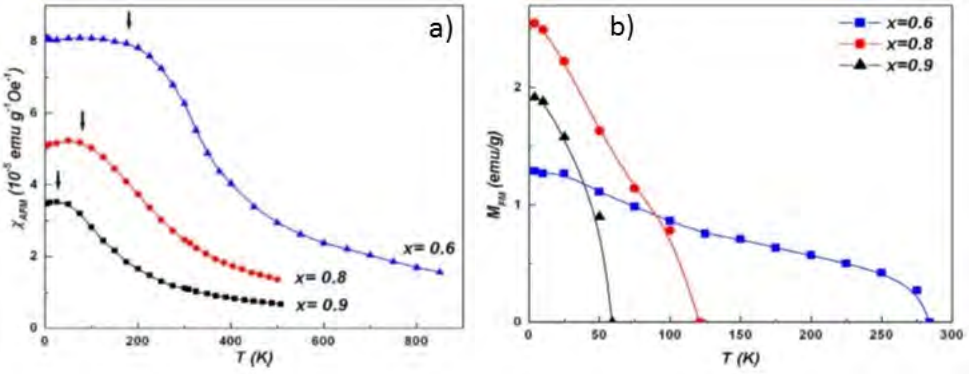

Fig. 4. The temperature dependence of the magnetic susceptibility χ_{AFM} (a) and the magnetization (b) of $Mn_{1-x}Al_xNi$ alloys. The arrows indicate the Néel temperatures. [10].

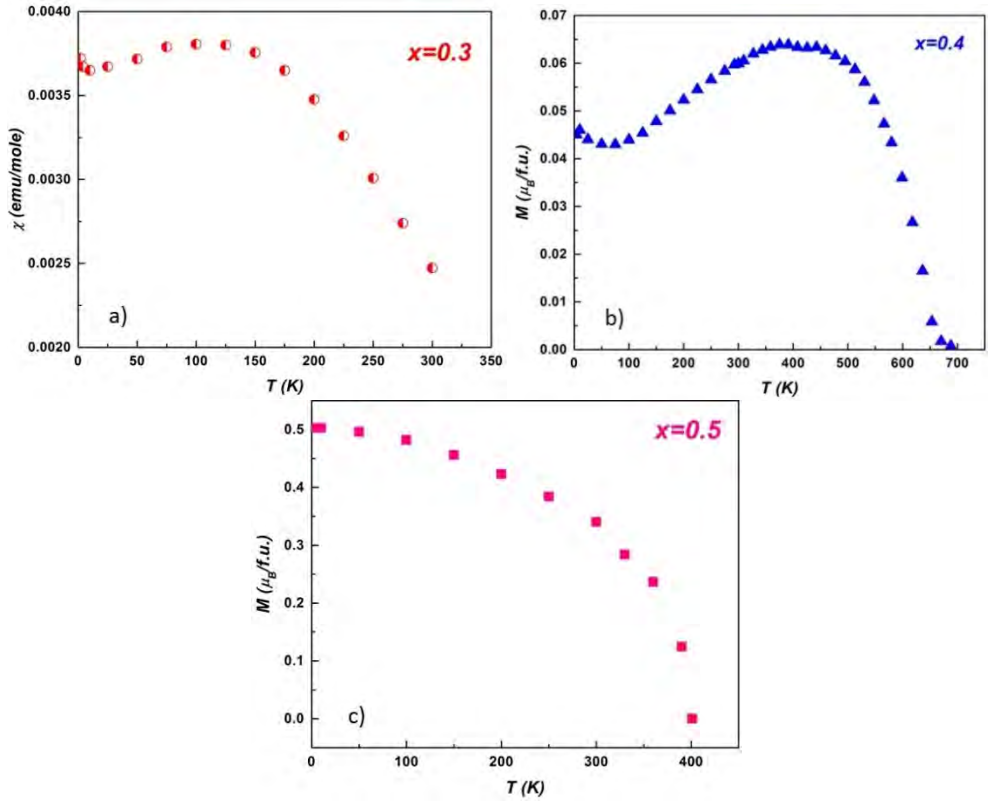

Fig. 5. The temperature dependence of magnetic susceptibility (a) and the spontaneous magnetization (b and c) of Ni0.7-xAlxMn0.3 alloys.

The $Ni_{0.4}Al_{0.3}Mn_{0.3}$ alloy has the lattice parameter a≈2.90Å. At this distance the Mn-Mn coupling is antiferromagnetic. The $Ni_{0.3}Al_{0.4}Mn_{0.3}$ alloy has the lattice parameter a little bit larger a≈2.914Å, but seems to be at the limit distance between the AFM and FM coupling. This could be a reason why this alloy has ferrimagnetic behaviour. The lattice parameter of the $Ni_{0.2}Al_{0.5}Mn_{0.3}$ alloy is larger (a≈2.94Å) and it has a ferromagnetic behaviour. This means that at this distance the coupling between the Mn atoms is parallel.

The strength of Mn-Mn interaction

The strength of Mn-Mn interaction and consequently the value of Mn local magnetic moments strongly depend on surrounding atoms. The Mn magnetic moment is sensitive to the type, the number and the distance to the atoms from the first coordination shell. These factors will influence the hybridization degree of Mn 3d band. In Mn-Ni-Al system, the Al atoms bring 3 valence electrons. The hybridization between Mn 3d state and Al 3sp states leads to a partial filling of Mn 3d band and consequently a reduction on Mn magnetic moment (the higher the hybridization degree the lower Mn magnetic moment will be). The hybridization degree depends on the number of Al atoms from Mn first coordination shell and Mn-Al distance. To support these affirmations we analysed the influence of Mn 3d - Al 3sp hybridization on Mn magnetic moment in two systems: a) $Mn_{1-x}Al_xNi$ (0 - 8 Al atoms in the first vicinity of Mn atoms, at d_{Mn-Al}≈2.9Å) and b) $Ni_{1-x}Mn_xAl$ (8 Al atoms in the first vicinity of Mn atoms, at d_{Mn-Al}≈2.5Å). XPS measurements correlated with magnetic measurements are further presented for both cases.

a) The Mn 3s spectra for MnNi, $Mn_{0.9}Al_{0.1}Ni$ and $Mn_{0.8}Al_{0.2}Ni$ are shown in figure 6. The shoulder around 79 eV corresponds to the Ni 3p satellite situated at about 12 eV higher binding energy from the main line [13].

The experimental spectra were fitted with two components corresponding to Mn 3s exchange splitting, the Ni 3p satellite and a Shirley background type. Figure 6b presents the curve fitting results of MnNi compound, after background and Ni 3p satellite subtraction. Similar results were obtained for the other two alloys $Mn_{0.9}Al_{0.1}Ni$ and $Mn_{0.8}Al_{0.2}Ni$. All spectra exhibit a well-defined magnetic exchange splitting of about 5 eV, arising from the exchange interactions between the 3s core hole and open Mn 3d shell. This splitting corresponds to a spin S≈2 and a magnetic moment of $4\mu_B$/Mn, suggesting that at this Mn-Al distance (2.9 Å) the Mn 3d band is not affected by the hybridization with Al 3sp states. Magnetic measurements confirm just a small variation of Mn magnetic moments, once the Al concentration increases, compared to MnNi compound [10].

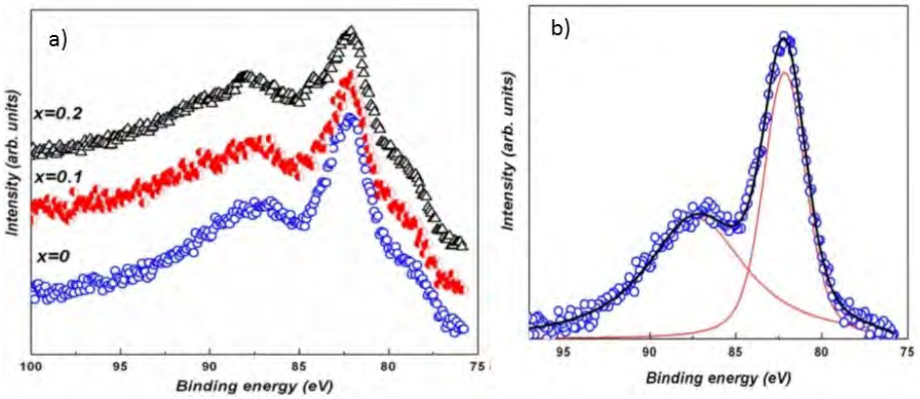

Fig. 6. Mn 3s XPS spectra of $Mn_{1-x}Al_xNi$ alloys (a) and Mn 3s curve fitting results of MnNi compound (b). [10]

b). In the second system $Ni_{1-x}Mn_xAl$, the Mn 3s core level spectra show an exchange splitting of around 4 eV, which is smaller compared to the exchange splitting in $Mn_{1-x}Al_xNi$ alloys (5.2 eV). The exchange splitting is proportional with the Mn local magnetic moment [13]. Figure 7 presents the curve fitting results of $Mn_{0.8}Ni_{0.2}Al$ alloy, after background subtraction, and the similar spectrum of MnNi compound for comparation.

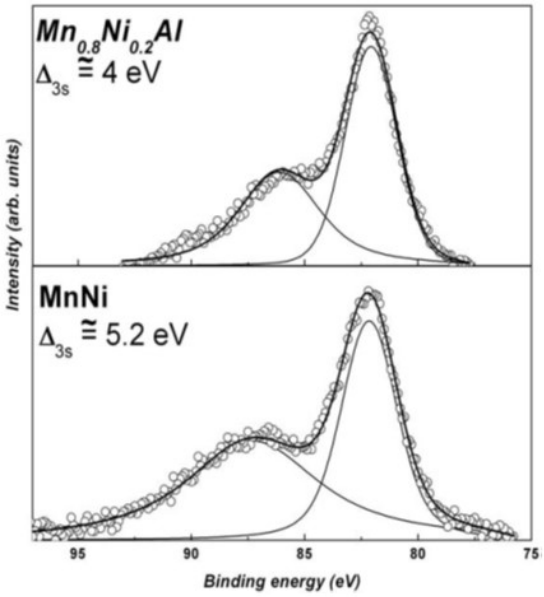

Fig. 7. Mn 3s curve fitting results of $Mn_{0.8}Ni_{0.2}Al$ alloy and MnNi compound. [9]

The strong Mn 3d - Al 3sp hybridization is due to the high number of Al atoms in the Mn first vicinity, namely 8 Al atoms at ~2.5 Å. This explains the small values of the Mn magnetic moments (below $2\mu_B$) in $Ni_{1-x}Mn_xAl$ alloys [9] comparing to $Mn_{1-x}Al_xNi$ alloys.

The Mn magnetic moment slowly increases with Mn concentration [9]. This variation can be associated with the increase of the lattice parameter which leads to a decreasing in the Mn 3d - Al 3sp hybridization degree.

CONCLUSIONS

We evidence a value of about 2.91 Å as the critical Mn-Mn distance in Mn-Ni-Al alloys. Experimentally we demonstrated that, if the separation between the Mn atoms is greater than this critical value, the exchange coupling is ferromagnetic and if the distance is smaller than the critical value, the exchange coupling is antiferromagnetic. The value of Mn local magnetic moment depends on the number of Al atoms in the first vicinity but the dominant factor is the Mn-Al distance. When the Mn-Al distance is about 2.9 Å the Mn 3d band is not affected by the hybridization but, at lower Mn-Al distance (~2.5 Å) the hybridization between Mn 3d and Al 3sp states leads to a partial filling of Mn 3d band and a drastically reduction of Mn local magnetic moment.

REFERENCES

[1] V. Yu. Irkhin, M. I. Katsnelson, A. V. Trefilov, *J. Phys.: Cond. Matter.*, 5, 8763 (1993).
[2] P.W.Anderson, *Phys. Rev.*, 124, 41-53 (1961).
[3] V. Seshu Bai, T. Rajasekharan, *J. Magn. Magn. Mat.*, 42, 198-200 (1984).
[4] R. Forrer, *Ann.de Phys.*, 7, 605 (1952).
[5] Suguru Sato, Shuichiro Irie, Yuki Nagamine, Tasashi Miyazaki, Yuji Umeda, *Scientific reports*, https://doi.org/10.1038/s41598-020-69538-2
[6] J. C. Slater, *Phys. Rev.*, 36, 57 (1930).
[7] H. Bethe, „Handbook of Physics", Vol 24/2 (Springer-Verlag, Berlin, 1933) p. 595.
[8] V. Raghavan, *Journal of Phase Equilibria and Diffusion*, 27 (5), 493-496 (2006).
[9] V. Rednic, O. Isnard, M. Neumann, L. Rednic, M. Coldea, N. Aldea, *J. Optoelectron. Adv. Mat.*, 13(11-12), 1519-1523 (2011).
[10] V. Rednic, M. Coldea, S. K. Mendiratta, M. Valente, V. Pop, M. Neumann and L. Rednic, *J. Mag. Mag. Mat.*, 321, 3415–3421 (2009).
[11] L. F. Bates, "Modern Magnetism", Cambridge Univ. Press, Cambridge, 1951.

[12] V. Rednic, M. Coldea, O. Isnard, M. Neumann and L. Rednic, *Studia Universitatis Babes-Bolyai Physica*, LIV (1), 79-85 (2009).
[13] S. Hüfner, “Photoelectron Spectroscopy Principles and Applications”, Springer-Verlag, Berlin (1995), p. 89.

STUDIA UBB PHYSICA, Vol. 66 (LXVI), 1-2, 2021, pp. 121-131
(RECOMMENDED CITATION)
doi:10.24193/subbphys.2021.11

NONTHERMAL PLASMA IN CONTACT WITH LIQUIDS

S.D. ANGHEL[1]

ABSTRACT. The current work shows the generation methods of atmospheric pressure plasma in liquids or on liquids. The optical diagnosis proves the nonthermal character of generated plasmas. They were tested for dyes degradation, nanostructures synthesis and for obtaining of plasma activated water. The activated water preserves its new characteristics for at least three weeks and is a promising agent for bacterial inhibition.

Keywords*: in/on-liquid plasma, dye degradation, nanoparticles synthesis, plasma activated water, bacterial inhibition.*

INTRODUCTION

Although the gas discharges in liquids were known for many years due to their applications in various fields, during the last decades the non-thermal plasmas generated in liquids or in contact with liquids have been intensively investigated [1]. The researchers' attention was focused on two main directions: (a) plasma generation, plasma diagnostics and discharge mechanism clarification [2–4]; and (b) possible applications: decontamination, sterilization and purification processes [5–10], nanoparticles and polymers synthesis [11] and analytical spectrometry [12]. Generally, this kind of plasma is generated between two electrodes immersed in liquid or between an electrically powered electrode and a liquid which is in contact with a grounded electrode [1]. The voltage applied between electrodes can be continuous or time variable (sinusoidal or rectangular pulses, see Table 1). The ignition mechanism of plasma in liquids was most frequently related to the presence of gas bubbles in liquid. A gas can be bubbled into the liquid or gas micro-bubbles are the result of chemical and physical processes occurring in the liquid. When a bubble is very close to the powered electrode (mostly sharpened in order to create high electric fields), electric discharges like streamers or micro-arcs could be generated.

[1] *Babeș-Bolyai University, Faculty of Physics, 1 Kogălniceanu str., 400084 Cluj-Napoca, Romania*

Table 1. Electrode geometries for the generation of plasma in liquids.
Plasma gases: O_2, Ar, He, N_2, air.

Electrodes geometry	Ref.	Inter-electrode distance [mm]	Electrical parameters
tube-to-plate	[5]	5-10	pulse: 6 kV, 1 μs, 4.5 A_{pk}
plate-to-plate	[6]	10	pulse: 20 kV, 6 μs, 300 A_{pk}
	[7]	2-3	pulse: 8 kV, 0.2 μs, 4 A_{pk}
	[8]	0.5	DC: 0.7 kV, 40 mA
	[9]	7.5	pulse: 22 kV, 0.2 μs, 250 A
pin-to-plate	[3]	6	pulse: 15 kV, 2.5 μs, 1000 A_{pk}
multi pin-to-plate	[10]	10-15	DC high voltage
wire-to-cylinder	[13]	1 (quartz)	sinus, 13.56 MHz, 80 W

2. PLASMA GENERATION

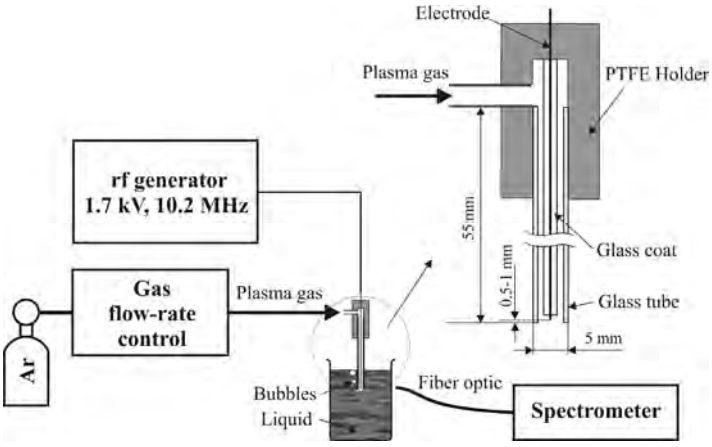

Fig. 1. The experimental set-up and a detail of the in-liquid plasma reactor.

Fig. 1 presents the schematics of the experimental set-up when plasma is generated in liqiud. The plasma reactor is composed of a metal wire electrode (Kanthal) placed via a holder piece in a quartz tube through which plasma gas flows with adjustable flow rate. The electrode is powered with high sinusoidal voltage generated with a laboratory made free-running oscillator [14]. The glass tube is vertically immersed in the liquid at a depth of 15-20 mm. When plasma gas (argon) flows, at the immersed exit of the glass tube gas bubbles arise with a cadency (0.5 – 10 bubbles/second) which depends on the gas flow rate (0.06 –

0.35 l min^{-1}). During each bubble life a glow discharge is generated between the free end of the electrode and the bubble wall. Fig. 2 shows the most representative video frames from the point of view of the discharge dynamics. A discharge cycle has three stages: (1) pushing the water towards the end of the quartz tube and the gas bubble formation, frames 1-38; (2) the discharge initiation at the powered electrode and its development as streamers with many branches bridging the electrode and the gas-water wall. Simultaneously the gas bubble expands outside the glass tube, frames 43-54; and (c) the extinction of the discharge when the gas bubble detaches from the border of the quartz tube and slides up on its wall, frames 55-57.

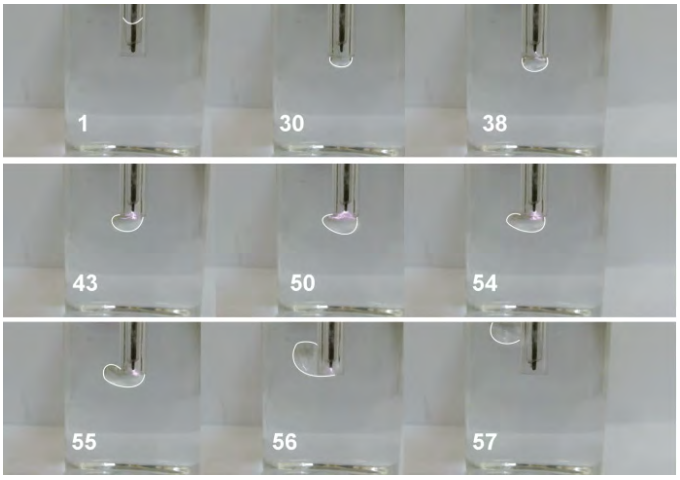

Fig. 2. Time evolution of the plasma generation process during an ignition-extinction cycle. Each imprinted number indicates the number of the frame from a total of a 63 frames/cycle.

The experimental setup to generate plasma on liquid presented in Fig. 3 is very similar to the one presented in Fig. 1, excepting the discharge reactor. It was replaced with two different powered electrodes for generating the plasma on water. The first one is a capillary metallic tube through which helium or argon flows to generate a plasma μ-jet surrounded by the ambient atmosphere. To generate a μ-arc discharge in ambient air a Kanthal wire electrode was used. The second electrode for both discharges is represented by the treated water. The inserts from Fig. 3 show the μ-jet and μ-arc discharges.

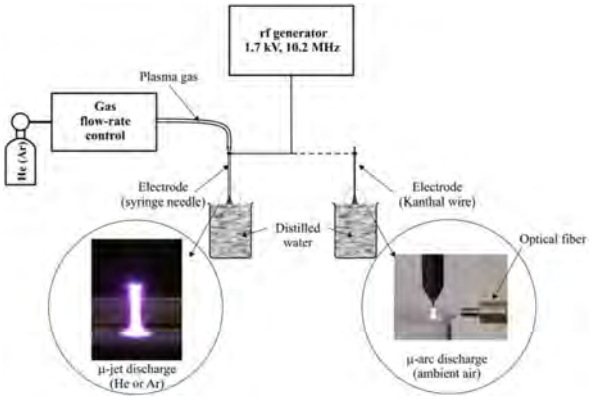

Fig. 3. Experimental set-up to generate plasma on liquid.

3. RESULTS AND DISCUSSION [15 - 20]

3.1 Plasma emission

Fig. 4 shows the emission spectrum of Ar plasma generated in distilled water. With the exception of the argon emission lines, the emission lines of hydrogen (H_α) and oxygen, and the emission bands of $OH^\bullet$ radical as a result of water molecules dissociation are present. Based on the spectrum, plasma parameters were determined: T_{excAr} = 6080 K, T_{rotOH} = 1990 K and n_e = $3.79 \cdot 10^{15}$ cm^{-3}. The high excitation temperature of the electrons in Ar atoms indicates the presence of energetic electrons capable of generating**,** by inelastic collisions, molecular species able to degrade organic dyes, mainly hydroxyl radical $OH^\bullet$ with a high oxidation character.

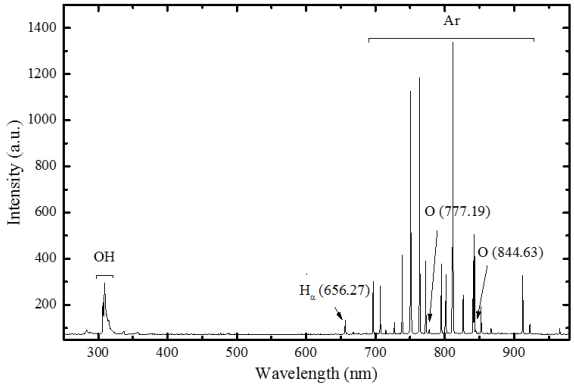

Fig. 4. Emission spectrum of plasma generated in Ar bubbled in water.

3.2 Methylene blue degradation with in-liquid plasma and time evolution of the solution characteristics

Being known that the main degradation mechanisms of MB solutions is the decomposition by energetic electrons and the oxidation under the action of hydroxyl radical and hydrogen peroxide, the influence of the initial dye concentration and the treatment time on the degradation process and on the time evolution of the MB solutions' characteristics after the ending of the exposure to plasma were studied.

The gradual change of the UV-vis spectra and of the visual aspect (see the insertion) for the solution containing 100 mg l^{-1} MB is exemplified in Fig. 5.

The spectra show the characteristic absorption bands of MB in water. The exposure to plasma treatment produces changes in the absorption spectrum. The main absorption band (663 nm) decreases in intensity, a blue shift is observed and after 45 minutes it becomes a flat line suggesting that the methylene blue solution was completely discolored. The blue-shift of the 663 nm band might be correlated to the change of pH which decreases from a value of 5 before treatment, to the value of 2 after the complete degradation. This might be due to the formation of intermediate organic acids during the degradation process of the MB molecules but more importantly due to H^+ produced by means of water dissociation.

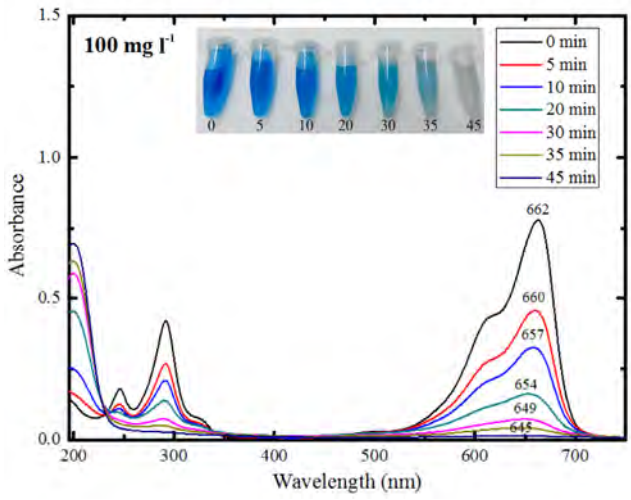

Fig. 5. The absorption spectra evolution for the MB solution with an initial concentration of 100 mg l^{-1} and the image of the samples collected during plasma treatment at different time intervals after the beginning of the treatment.

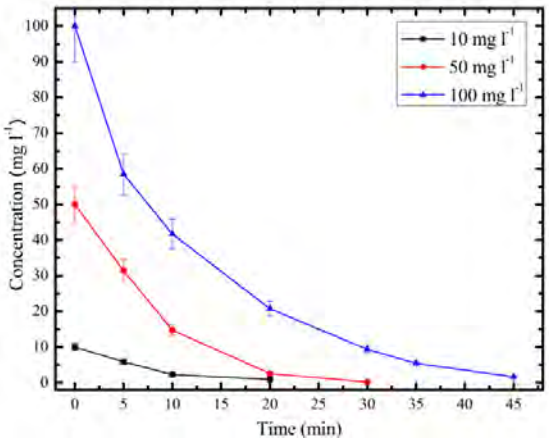

Fig. 6. The dependence of the MB concentration on the treatment time with the initial concentration as parameter.

The changes in MB concentration during the plasma treatment are presented in Fig. 6. The time evolution of the MB concentration shows that the degradation process continues slowly for at least ten minutes even after the plasma treatment was stopped. This fact suggests that the active species generated by the plasma are the ones responsible for the degradation.

During the plasma treatment the electrical conductivity of MB solution increases relatively linear from very low values to higher ones as it can be seen in Table 2. The increase in the electrical conductivity leads to suppose that new ions are generated at the plasma-liquid interface by water molecules dissociation and these ions are H^+. The values of the electrical conductivity and pH after two weeks from the treatment suggest that the processes are irreversible at least for this time period.

Table 2. The time evolution of the electrical conductivity and pH of the treated MB aqueous solution (50 mg l^{-1}, 35 min treatment time)

Electrical conductivity, µs cm^{-1}			pH		
Before treatment	At the end of treatment	Two weeks later	Before treatment	At the end of treatment	Two weeks later
9	595	635	5	4	3

3.4 Carbon structures synthesis with in-liquid plasma

Concurrently with the MB degradation a secondary result of the treatment with plasma which was not mentioned so far in papers, is the progressive generation of very small solid structures. The XPS analysis shows that the plasma breaks the structure and seems to favor the bonding of oxygen in different molecular sites leading to the formation of new bonds of the oxygen with carbon and even nitrogen and sulfur. Thus we could explain the formation of the very small solid particles which are formed preponderantly of carbon and also of contributions coming from oxygen. The TEM image, shown in Fig. 7, reveals the presence of spherical particles having tens of nm in diameter in these solid structures. The insertion from figure 7 shows a great number of solid structures obtained after 45 minutes of treatment of the solution with a concentration of 100 mg l^{-1} MB.

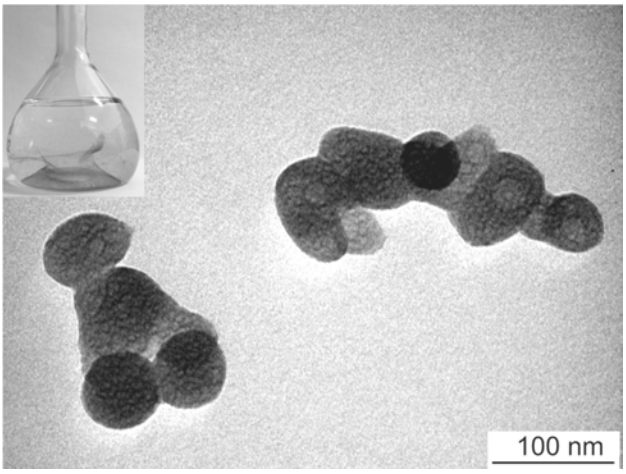

Fig. 7. TEM image of solid structures generated by treatment with bubbled Ar plasma of 100 mg l^{-1} MB solution. The insert presents a photo of the solid particles in solution at the end of the plasma treatment.

A schematic representation of the synthesis procedure is presented in Fig. 8. It suggests that there are three main mechanisms for dye degradation in plasma in liquids: electron bombardment, ion collision and radical induced degradation. It also shows that the nature of plasma gas (Ar or He) influences the dimensions and forms of the synthesised carbon nanostuctures.

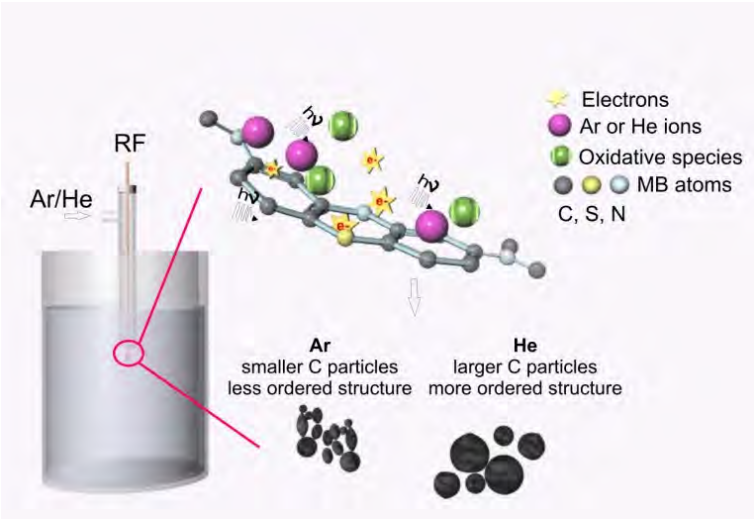

Fig. 8. Schematic representation of the synthesis procedure and mechanism.

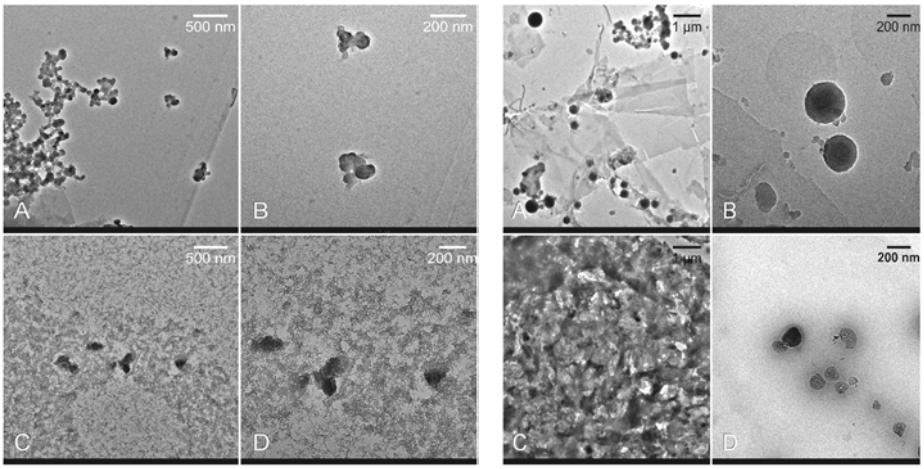

Fig. 9. TEM images of the Ar plasma carbon structures (left) obtained at different time treatments: A,B-20 minutes C,D- 40 minutes and of the He plasma carbon structures (right) obtained at different time treatments: A,B-20 minutes C,D- 60 minutes.

The TEM analysis (Fig. 9) showed that the structures obtained with the He plasma are larger compared to the case of the Ar plasma and revealed that the plasma has a destructive effect on the structures as well.

3.5 Plasma activated water and bacterial inhibition

Under the action of atmospheric pressure plasma, distilled water changes its characteristics, mainly pH and electric conductivity, and acquire an important oxidative potential. The so treated water is named plasma activated water (PAW). Depending on the nature of the discharge gas (Ar, He, O_2, air, or their mixture), reactive oxygen species (ozone O_3, hydrogen peroxide H_2O_2, hydroxyl radical $^{\cdot}OH$) and reactive nitrogen species (peroxynitrite, nitrate, nitrite and the corresponding acids, nitrogen oxides NO_x) are generated in the plasma core or in the plasma-liquid contact zone being then dissolved in the liquid. Fig. 10 shows the dependence of their concentrations on the treatment time. They are responsible for a large variety of applications of plasmas in contact with liquids, mainly in the bio-medicine field and for reduction of environmental pollution. The presence of nitrogen is important for the activation of water-based liquids. Generally, it enters in the discharge from ambient air as a result of diffusion and contributes to the generation in plasma of reactive oxygen and nitrogen species which are then transferred to the liquid phase.

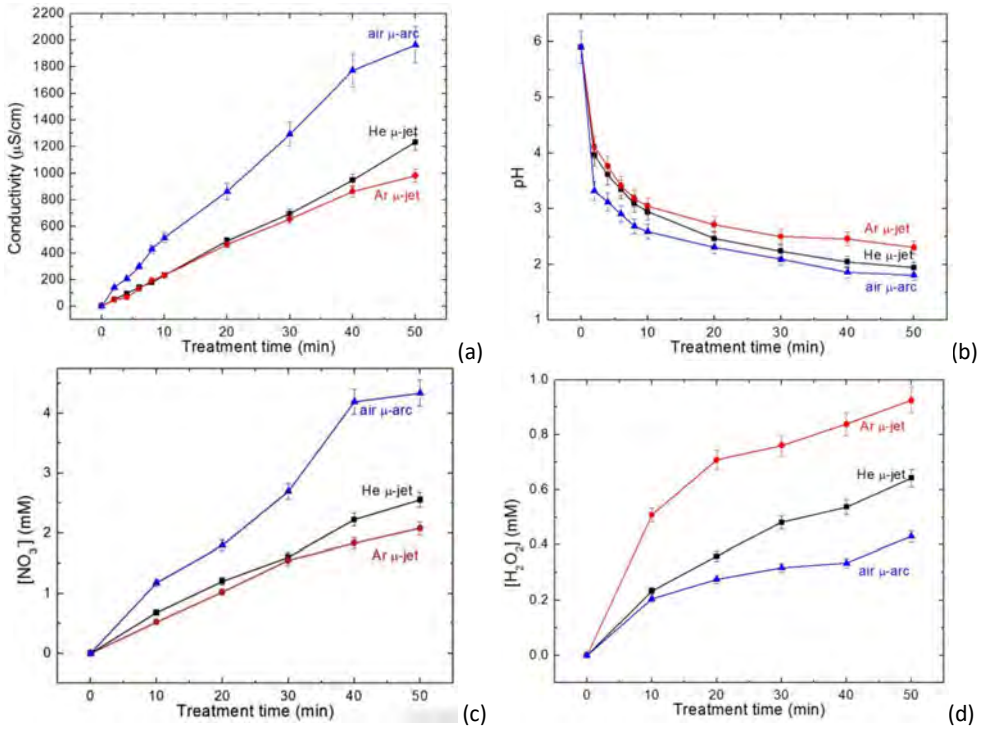

Fig. 10. Electrical conductivity (a), pH (b), nitrate (c) and H_2O_2 (d) concentrations dependences on the treatment time for water samples of 35 ml.

The new attributes (pH value, electrical conductivity, nitrate and hydrogen peroxide concentrations) acquired by the PAW solutions do not change significantly for at least 21 days.

The so obtaned PAW's were used to study the inhibitory effect on *Staphylococcus aureus*. The bacteria was selected because it is one of the most common infectious agents as it causes numerous skin and respiratory infections, food poisoning and it is very dangerous in hospital hygiene. The PAW's were incubated with the microorganisms and their inhibition effect on the bacteria is assessed. The inhibition effect was investigated by determining the optical density of the bacterial suspensions at 620 nm using a Jasco V-530 UV-VIS spectrophotometer. It was estimated as it is shown in [20].

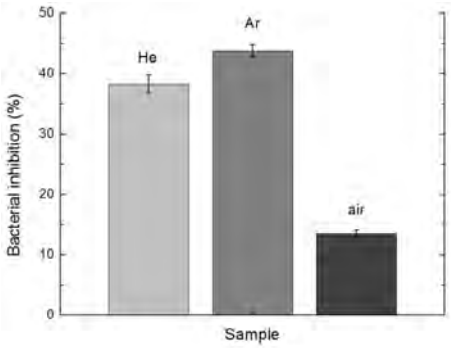

Fig. 11. Bacterial inhibition effect of PAW – discharge type influence.
PAW obtained after exposure to the plasmas for 50 minutes was used.

Fig. 11 shows that the air discharge offers the lowest inhibition rate while the Ar discharge shows the more intense effect. Considering the properties of the PAW ilustrated in Fig.10, it can be observed that the Ar discharge creates the highest concentration of hydrogen peroxide, followed by the helium and air discharges, which is similar to the inhibition effect on the *S.aureus* samples. Furthermore, by increasing the treatment time of the PAW samples, the concentration of hydrogen peroxide is also increased.

CONCLUSIONS

This work has shown the possibility to generate plasma in liquids by using a new device for bubbling the plasma gas and atmospheric pressure plasma on liquids. The plasma emission shows the presence of chemically active species which

are important for methylene blue degradation and for synthesis of carbon based nanoparticles. The activation of distilled water was also studied. Plasma activated water has a long time stability and represents a promising agent for bacterial inhibition.

AKNOWLEDGEMENTS

The author thanks to Dr. Iulia Elena Vlad and Dr. Diana Zaharie-Butucel for successful collaboration over several years.

REFERENCES

1. P. Bruggeman, C. Leys, *J. Phys. D: Appl. Phys*., 42, 053001 (2009).
2. Q. Chen, J. Li, K. Saito, H. Shirai, *J. Phys. D: Appl. Phys.,* 41, 175212 (2008).
3. P. Vanraes, A. Nikiforov, C. Leys, *J. Phys. D: Appl. Phys.*, 45, 245206 (2012).
4. P. Bruggeman, J, Degroote, C. Leys. J. Vierendeels, *J. Phys. D: Appl. Phys*., 41, 194007 (2008).
5. S. Gershman, O. Mozgina, A. Belkind, K. Becker, E. Kunhardt, *Contrib. Plasma Phys.,* 47 19 (2007).
6. K. Sato, K. Yasuoka, S. Ishii, *Electr. Eng. Jpn*., 170, 1 (2010).
7. K. Yasuoka, K. Sato, *Int. J. Plasma Env. Sci. Technol.,* 3, 22 (2009).
8. [19] A. Yamatake, H. Katayama, K. Yasuoka, S. Ishii, *Int. J. Plasma Env. Sci. Technol.,* 1, 91 (2007).
9.T. Miichi, N. Hayashi, S. Ihara, S. Satoh, C. Yababe, *Ozone-Sci. Eng*., 24, 471 (2002).
10. Y. Akishev, M. Grushin, V. Karalnik, N. Trushkin, V. Kholodenko, V. Chugunov, E. Kobzev, N. Zhirkova, I. Irkhina, Kireev G, *Pure Appl. Chem.,* 80, 1953 (2008).
11. D. Mariotti, R. M. Sankaran, *J. Phys. D: Appl. Phys.,* 44, 174023 (2011).
12. P. Jamroz, P. Pohl, W. Zyrnicki, *J. Anal. Atom. Spectrom.,* 27, 1032 (2012).
13. H. Aoki, K. Kitano, S. Hamaguchi, *Plasma Sources Sci. Technol.,* 17, 025006 (2008).
14. S. D. Anghel, *IEEE Trans. Plasma Sci.,* 30, 660 (2002).
15. S. D. Anghel, D. Zaharie-Butucel, I. E. Vlad, *J. Electrostat.*, 75, 63 (2015).
16. D. Zaharie-Butucel and S.D. Anghel, *Roum. Journ. Phys.,* 59, 757 (2014).
17. I. E. Vlad, O. T. Marisca, A. Vulpoi, S. Simon, N. Leopold and S. D. Anghel, *J. Nanopart. Res.,* 16, 2633 (2014).
18. D. Zaharie-Butucel, J. Papp, C. Leordean, S. D. Anghel, *RSC Advances,* 5, 98325 (2015).
19. I. E. Vlad, S. D. Anghel, *J. Electrostat.,* 87, 284 (2017).
20. I. E. Vlad, C. Martin, A.R. Toth, J. Papp, S. D. Anghel*, Rom. Rep. Phys.,* 71, 602 (2019).